MWET

Aircraft Family

AIAA Design competition

LIÈGE université
Aerospace &
Mechanical engineering

AIAA

50

56200 lbs

3206 ft	2000 n mi	3687 ft
Takeoff distance	Range	Landing distance

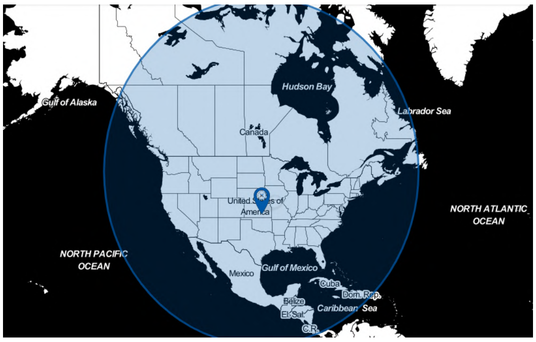

MWET-50

Length: 75.8 ft

Span: 91.9 ft including winglets length: 19.68 ft

Cruise speed: 470 kts

Cruise altitude: 32000 ft

USD 57,000,000

MWET

76

70637 lbs

4165 ft	2000 n mi	4003 ft
Takeoff distance	Range	Landing distance

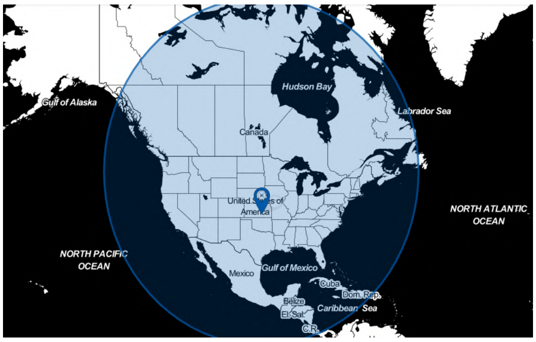

MWET-76

Length: 92.2 ft

Span: 91.9 ft including winglets length: 19.68 ft

Cruise speed: 470 kts

Cruise altitude: 32000 ft

USD 63,000,000

The *MWET* Crew

Name	**AIAA N°**	**Signature**
Thomas BASTIN	1192290	Bastin
Guillaume BEAULIEU	1192623	Beaulieu
Guillaume BRIAN	1192586	
Regnauld COLLARD	1192627	
Martin JOLIS	1192587	Jolis
Tarek ORABI	1192615	
Bastien RANSY	1192584	Ransy.
Samuel WILLEMOT	1192291	Willemot
François WINAND	1192298	
Morgane ZEOLI	1192589	Zeoli

Faculty advisors
Grigorios DIMITRIADIS - AIAA 213432
Ludovic NOELS - AIAA 775328

Project advisors
Adrien CROVATO
Thomas LAMBERT

Contents

Introduction

The aviation industry is of paramount importance in the world as it helps to connect continents, countries and cultures within a few hours. Whether it is for work, cargo transport or leisure, aviation has demonstrated to be the fastest and most efficient way to travel long distances. The industry is constantly growing with the increasing demand. As part of this large and prolific industry, the regional jet market bases its fleet mainly on design from the early 1990s such as the 50-seater Canadian Regional Jet (CRJ) or the Embraer (ERJ) 145. In the next 20 years, it is forecast that about 2000 new regional aircraft could be needed [1], giving the opportunity to design more efficient aircraft in terms of fuel burn, and thus in terms of CO_2 emissions, and economics than existing options.

In this context, the American Institute of Aeronautics and Astronautics (AIAA) posted a request for proposal to design a family of regional aircraft with fuel consumption 20% better than existing alternatives, with a comparable manufacture cost [1]. A 50-seat and 76-seat variant are requested. In this context, the *MWET* (pronounced "mouette"[1] in French) crew developed the conceptual design for *MWET-50* and *MWET-76*: two high-wing regional aircraft that feature **Movable Wingtips and an Electric Taxiing system** (**MWET**). With those innovations, both aircraft successfully fulfill the requirement concerning the fuel reduction, while remaining in the range of the cost of similar regional aircraft.

Target Market

The Covid-19 pandemic has undeniably a big impact on aviation industry and regional jets are no exception. According to a study from the Oliver Wyman firm [2], 2021 will not be any better than 2020. Although a growth is inevitably going to happen, a 10 years period is announced as the time needed to recover from this crisis and reach back the pre-pandemic situation. In this particularly difficult context, airliners might be less inclined to spend money on any aircraft, which is why efficiency is very important.

The markets on which the recovery seems to be the fastest are developing economies of Asia and the Middle East, which were already those with the most potential during the pre-Covid period. This report also forecasts that in the 2030's, they will experience the biggest traffic growth. In China, it is important to point out that domestic travel has already returned to pre-pandemic levels since end of 2020. For this reason, the market that will be targeted by the *MWET* family, planned in the 2030's, will be mainly Asia, although Europe and America can still be interesting potential market later on.

1 Mission Analysis

The *MWET* aircraft family is aimed to enter the aeronautical market as a new regional airliner family composed of a 50-seat configuration and of a stretch derivative which will be able to transport 76 passengers. The entry in service is planned for 2030. The chosen engine will therefore need to be available no later than 2029. The objective of this new generation of airliners is to be at least 20% better than existing 50-seat regional jets in 500 n mi block fuel per seat. Table 1.1 summarizes the main requirements

---

[1] It means "seagull" in French. The bird from which the flapping winglets were inspired. This bird is also very common at the Belgian coast, thus introducing a reference to the country where *MWET* was designed.

that the design will have to meet in order to comply with the Request for proposal (RFP).

	50-seat	76-seat
Passenger capacity	50	76
Design range [n mi]	2000	>1500
Cruise Mach number	0.78 [R]	0.78 [R]
	0.8 [O]	0.8 [O]
Wing span [ft]	ICAO Code B[1]	ICAO Code B
Cruise altitude [ft]	$\geq$ 32000	$\geq$ 32000
Takeoff distance [ft]	<4000	<6000
Landing distance[ft]	<4000	<6000
FAA Certification	FAA 14 CFR Part 25 [3], (§343)	FAA 14 CFR Part 25
Takeoff Requirements	FAA 14 CFR 25.121 [3], (§121)	FAA 14 CFR 25.121

Table 1.1: Summary of performance required and achieved by the MWET family of aircraft. [R] denotes the requirements and [O] the objectives.

Within the scope of reducing the family production costs and fuel consumption, series of design objectives have been defined in order to impose a design guideline. This will allow to make choices for the different components of the airplane. These design objectives, determinant for the choice of the innovations, are:

- minimizing the production costs by maximizing the commonality between both configurations;
- minimizing the operating costs;
- make the aircraft reliability equal to or better than that of comparable configuration.

2 Design Methodology

Figure 2.1 illustrates the general design methodology that guided the *MWET* design. The starting point for the conceptual design is to analyze the mission: based on the kind of aircraft that must be designed and the specific requirements, similar aircraft are studied in order to have a global view of the design. Different configurations have been compared, and choices were made to design an aircraft that best suits the mission. Based on an initial guess for the total weight, an initial sizing of each component is made. The stability is studied. The position of the wing and the tail is adjusted until the aircraft the static margin of the aircraft is in an acceptable range of values. If no configurations allow to have a stable aircraft, the conceptual design is updated. Afterwards, performances are evaluated. This iterative process is repeated until the designed aircraft fulfill all requirements and has optimized performance.

When the conceptual design of the aircraft is over, the preliminary design can begin. It consists in a more accurate evaluation of various parameters like the drag or the aeronautical loads. The design of the internal structure of the aircraft is also investigated.

---

[1] International Civil Aviation Organization (ICAO) has defined a requirement for regional airliner family named *Code B* which imposes the total span of any regional aircraft to be lower than 78.74 ft. in taxiing.

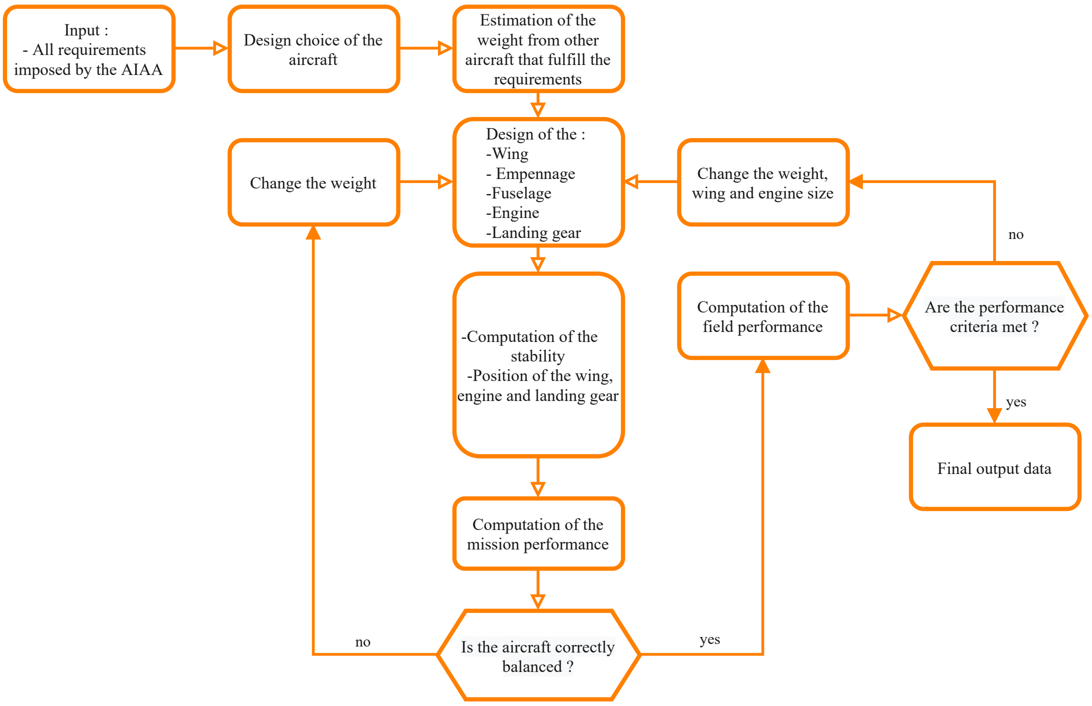

Figure 2.1: Flowchart of the conceptual design methodology (adapted from [4]). Solid arrows denote a choice from the design team while dashed arrows mean a logical follow-up.

3 Configuration

3.1 Existing Configurations

The first step in the design of a new aircraft is to study existing configurations which meet more or less the same requirements and which correspond to the same category of aircraft. It allows to have a global idea of what is done or not in the market and why. It gives also a first approximation of different parameters which are needed at the early stages of a design such as an estimation of the take-off gross weight.

Since the request for proposal imposes a regional aircraft family design which consists in two configurations, one of 50-seat and the other of 76-seat, existing aircraft from several aircraft family are reviewed to determine the *MWET* family general design choices and to begin the design. Some of these configurations are illustrated in Figure 3.1.

Based on these configurations, an optimal trade-off can be found in order to fulfill as much as possible the request for proposal. Throughout the design of the *MWET* family, these different existing configurations were used as benchmarks so that its main parameters could always be compared with theirs.

Figure 3.1: Different aircraft configurations: Mitsubitshi MRJ100 (top left), Embraer E-jet family (top right) and Bombardier CRJ family (bottom). [5–7]

	ERJ145 [8]	**CRJ200** [9]	***MWET-50***
Passengers	50	50	50
MTOW [lb]	48501	53000	56200
Max. payload [lb]	12755	13100	12820
Max. fuel [lb]	11322	14305	12010
Takeoff field length [ft]	7448	6290	3206
Landing field length [ft]	4593	4029	3687
Max. cruise speed [KTAS]	461	464	495
Range [nmi]	1550	1700	2000

Table 3.1: Typical 50-seats regional airliners.

	ERJ170 [8]	**CRJ700** [9]	***MWET-76***
Passengers	72	75	76
MTOW [lb]	82012	84500	70637
Max. payload [lb]	19848	19995	19060
Max. fuel [lb]	20580	19450	14700
Takeoff field length [ft]	5190	6072	4165
Landing field length [ft]	4029	5120	4003
Max. cruise speed [KTAS]	472	472	497
Range [nmi]	2100	2000	2000

Table 3.2: Typical 76-seats regional airliners.

3.2 General Design Choices

3.2.a Wing

High-wing. Three main wing configurations are available: low, mid or high-wing aircraft. The different configurations have their advantages and disadvantages. The choice of a high-wing is the more adapted for several reasons:

- Since *MWET-50* and *-76* are regional aircraft, they will not cross the sea for a long time thus an emergency landing in water can be avoided in case of failure. This usually non-negligible advantage of low-wings is not valid in this case and therefore, the high-wing configuration can be taken into account given that it has many advantages.
- The ground clearance is better. The engines can thus be placed such that interference effects with the wing are small. In addition, flaps can be bigger which is advantageous since the requirements in terms of take-off and landing distances are more restrictive than similar aircraft.
- It keeps the engine away from debris or rocks in case of emergency landing on rough terrain.
- A shorter landing gear is required, thus reducing its weight.
- The landing gear can be placed in the fuselage instead of the wings. Therefore, it reduces the loads applied by the wings on the fuselage.

Flexible Winglets. Many aircraft feature winglets but it exists many variants such as raked wingtips, canted winglets or wingtip fences to name a few. The particularity of the wing of the *MWET* aircraft is that it includes winglets with a semi-aeroelastic hinge, named *flexible winglets*. This innovative technology is based on a process of biomimicry which takes inspiration from albatross flights. Indeed, this type of bird is able to lock or unlock its wingtips as desired according to the flight conditions, which means that if they want to travel long distances without losing too much energy, they lock them. Inversely, if they face wind gusts, they unlock their wingtips to better surf through them. This device has two main functions. The first one is that it enables a span during the flight larger than the one restricted by ICAO Code B, because the winglets are folded up at 90° during taxiing to reduce the span under this restriction. The second one is that it enables a larger aspect ratio than conventional regional aircraft since the static and dynamic loads produced by the increase of span are almost not transferred to the main wing thanks to this innovative hinge, as explained in the *AlbatrossOne* project [10–16].

3.2.b Empennage

Among the multiple empennage configurations available for aircraft, a T-tail is chosen for *MWET-50* and *-76*. This tail configuration is popular among business jets and transport aircraft. The Bombardier CRJ200, Embraer ERJ 145 and the British Aerospace 146 (BAe 146), which are well-known regional aircraft, indeed have a T-tail.

This tail configuration presents many advantages. The vertical tail is located as far as possible from the disturbed airflow coming from the wing and the fuselage, and of the engine exit flow. It improves the performance of the empennage and its control surfaces. The lower influence of the wing on the horizontal tail also results in reduced vibration on the tail and thus less fatigue, increasing the lifetime of the empennage. In addition, the horizontal tail acts as a end-plate for the fin, allowing a reduction of the empennage drag.

However, the T-tail configuration also has drawbacks. A T-tail is heavier than the conventional tail configuration because the fin has to support the horizontal tail. In addition, the particular location of the horizontal tail with respect to the wing influences the stall characteristics. The horizontal tail can be caught in the wing wake at stall or post-stall. This phenomenon is called *deep stall* and can have dramatic consequences when it occurs. The perturbed incident airflow decreases the efficiency of the horizontal tail and of its control surface, reducing the contribution of the horizontal tail to the longitudinal stability. The aircraft must thus be stable enough to recover from stall even if the horizontal tail is blanketed by the wing wake.

3.2.c Engines

In general, high-wing aircraft use either turboprop engines or turbofans. Without considering their efficiency, the former are suitable for short flights from short runway while the latter allow to fly at higher cruise velocities and at a higher ceiling altitude. In order to respect all requirements, the final choice is in favor of the use of turbofans. In general, engines of regional aircraft are either mounted under the wings or aft-mounted. The high-wing configuration lead to the latter choice in order to avoid the distorted airflow endured by aft-mounted engines. Moreover, a promising sustainable aviation fuel is considered. It is indeed identified as one of the key elements to reduce the Greenhouse Gas emissions in the aviation domain.

3.2.d Electric taxing system (ETS)

The environmental impact has to be taken into account when designing a new aircraft. A lot of research are published concerning the use of as many electrical systems as possible in the aircraft. The *MWET* family is designed to be eco-friendly. A lot of fuel is consumed during taxiing. This consumption increases year by year due to the increasing number of passengers and thus the increasing number of aircraft at the airport. Typically, the busier the airport, the more time an aircraft spends on the ground. The duration is assumed to be around 30 minutes per flight. Moreover, the turbofan engine that is used today is optimized for flying and not to power the aircraft during taxiing on the ground and that could lead to more fuel consumption especially for medium-haul aircraft that spend more time in taxiing compared to the actual length of the flight. Consequently, an electrical taxiing system is used for the *MWET* family. It will allow to decrease the fuel consumption on the ground and to reduce carbon emissions (CO_2, NO_x, CO, etc). Another target of the *MWET* family by using the ETS electrical taxiing system is to be completely autonomous and able to taxi in and taxi out without using any ground services and infrastructure. According to interplex [17], this solution would help to reduce the traffic at the airport, improve flight punctuality, save more time during ground taxiing, and finally contribute to maximize the capacity at the airport.

3.3 MWET Aircraft Family CAD

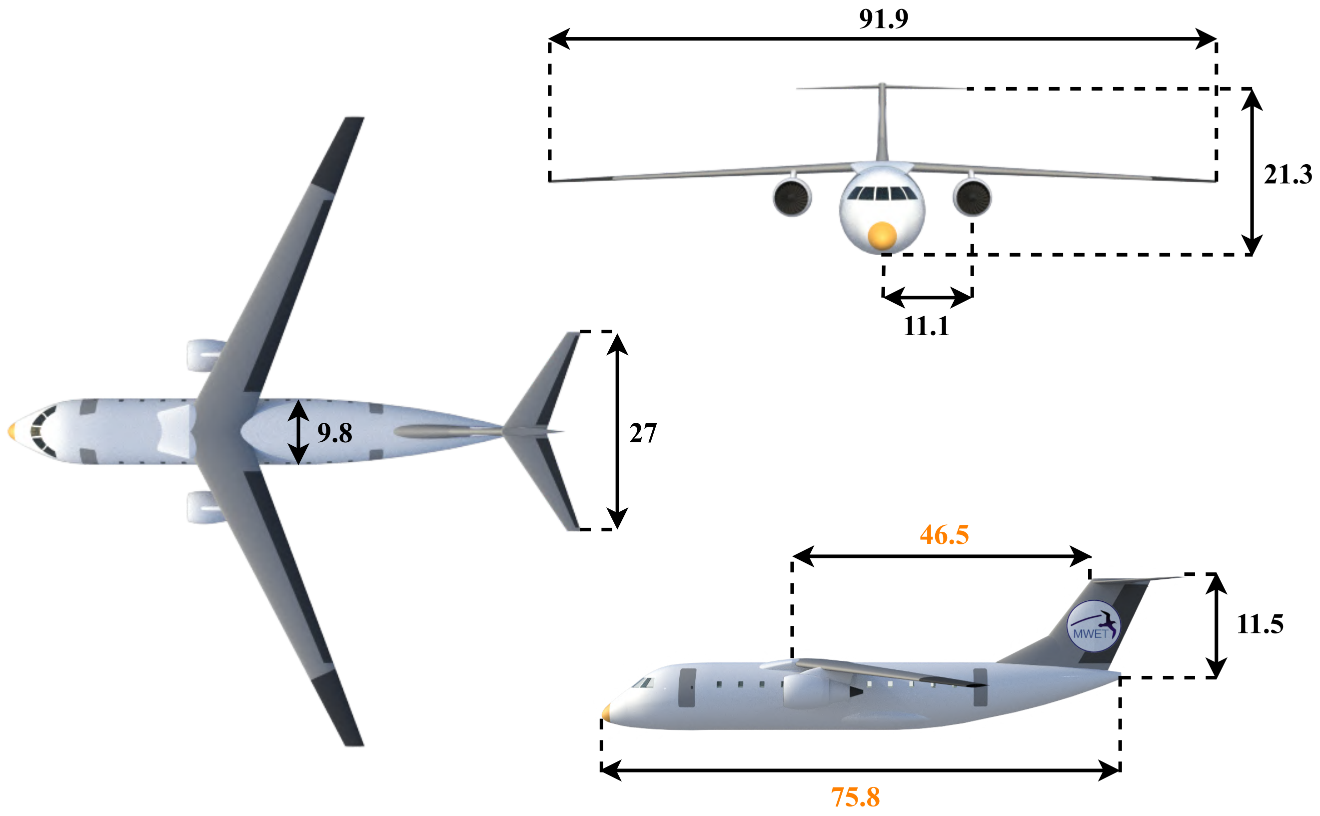

Figure 3.2: Three-views representation of *MWET-50*, dimensions in feet (black = common values for both configurations).

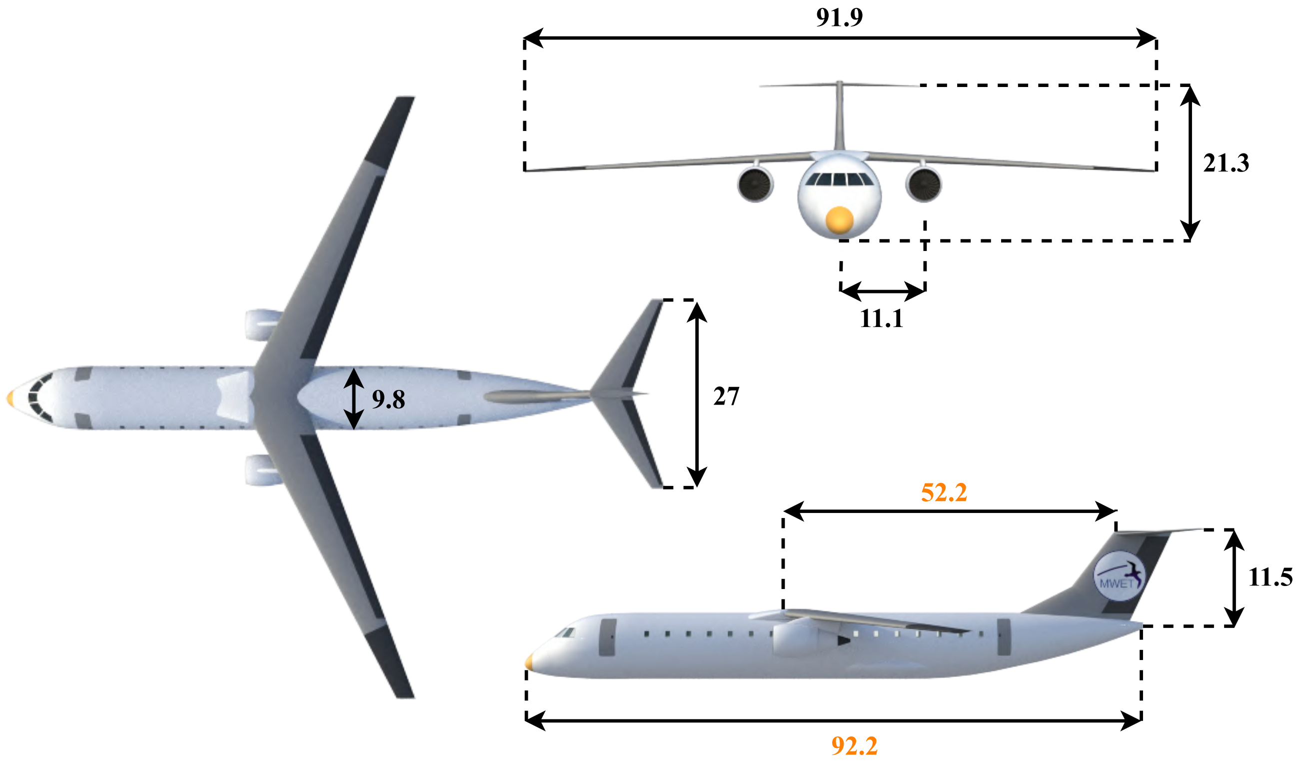

Figure 3.3: Three-views representation of *MWET-76*, dimensions in feet (black = common values for both configurations).

Figure 3.4: CAD of the *MWET-50* in flight and taxiing configuration.

Figure 3.5: CAD of the *MWET-76* in flight and taxiing configuration.

4 Component Design

4.1 Wing

The first step of the wing design is to estimate the lift force that the wing will have to produce based on a first guess of the take-off gross weight. As soon as the objective is determined, the geometric parameters can be evaluated following the needs and the requirements imposed by the *AIAA Design competition* [1]. The methodology which guides the entire wing design is illustrated in Figure 4.1.

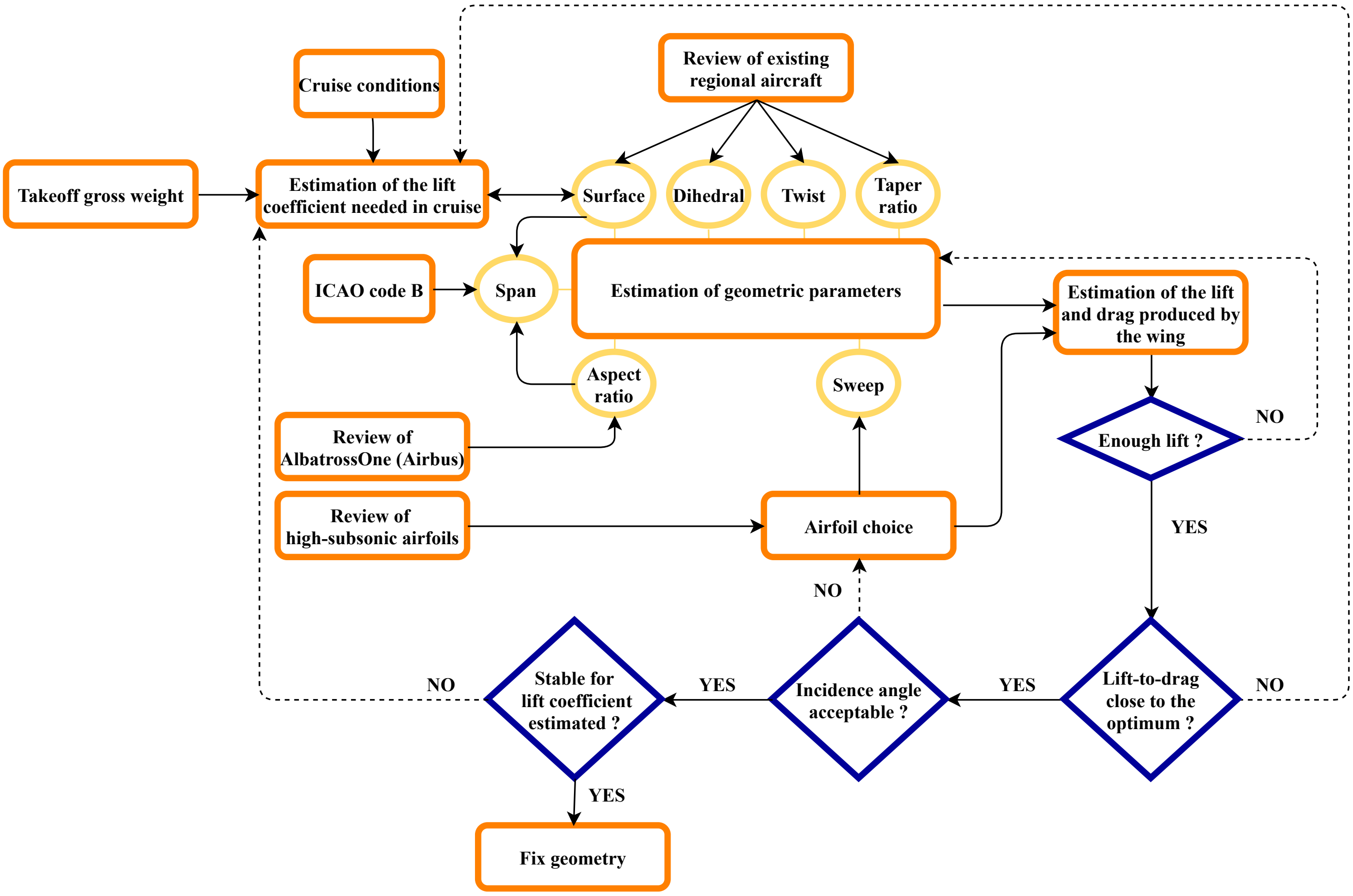

Figure 4.1: Wing design methodology; solid arrow means "determine", a dashed arrow means "change".

4.1.a Wing Planform

In order to design an optimal regional aircraft family with very similar characteristics for both configurations, it is interesting to design a single wing for *MWET-50* and *-76* to drastically reduce the manufacturing cost. Figure 4.2 illustrates a schematic of the entire wing planform. Furthermore, based on the general choices stated in Section 3.2, another main objective is to design a wing whose induced drag is considerably reduced compared to similar existing configurations. The objective is to decrease the *MWET* aircraft's fuel consumption.

Span. Based on existing configurations of regional airliners (Section 3.1) and in order to comply with the ICAO Code B, the wing span of the *MWET* family is set at 68.9 ft when the flexible winglets are folded up at 90°, i.e. during the taxiing phase. The

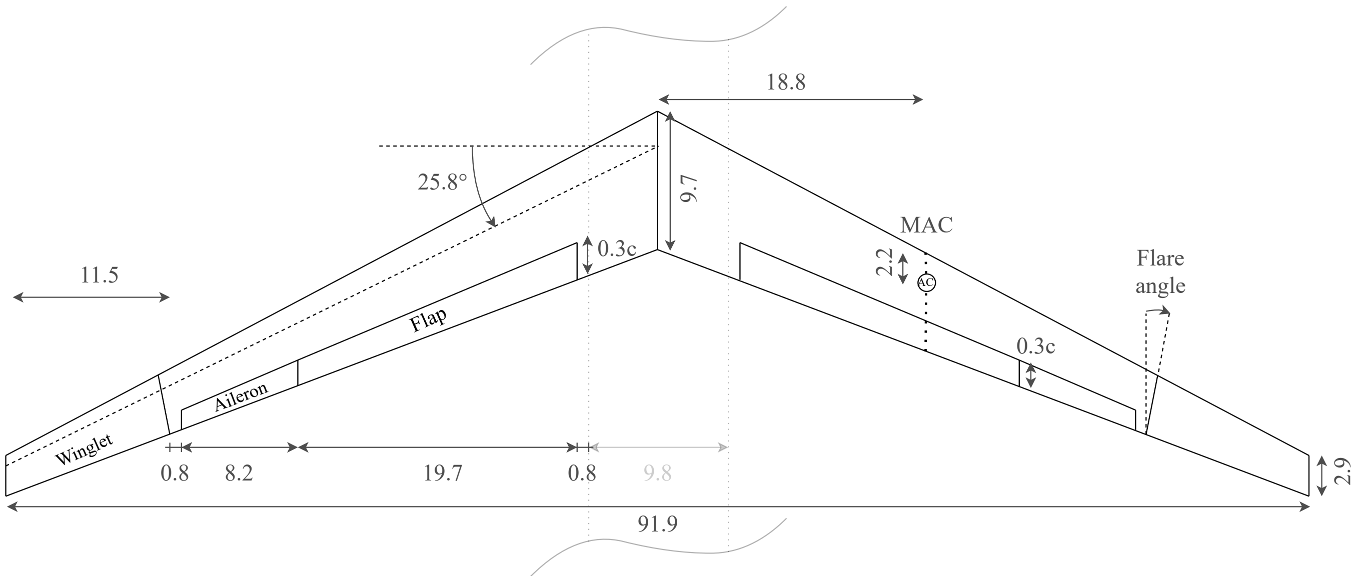

Figure 4.2: *MWET-50* and *-76* wing planform [ft]. MAC is the mean aerodynamic centre and c is the chord.

wing is designed to exceed this requirement in flight, as the winglets unfold. Following Castrichini's research [10], which claims that flexible winglets enable an increase in the wingspan by about 25% at the expense of an increase in the loads carried by the fuselage of only 4%, the wing span when the winglets are unfolded reaches 91.9 ft.

Aspect ratio. As it will be explained in details in Section 4.1.c, the flexible winglets enable to reach a higher aspect ratio than similar aircraft without increasing the loads transferred to the fuselage. That has the direct consequence of considerably reducing the induced drag compared to its competitors. Indeed, according to the design team of Airbus's *AlbatrossOne* [12], flexible winglets allow to double the wing aspect ratio of an Airbus-like aircraft without the usual detrimental impact on loads and handling qualities. Henceforth, the aspect ratio is set at 14.5 since the common aspect ratio for a regional airliner is between 7 and 9 (Section 3.1).

Wing area. The wing area can be deduced from the aspect ratio and the span. This results in a total surface of 581.25 ft^2, which is in the same range as the other regional airliners comprising 50 to 76 seats.

Taper ratio. The choice is based on a very common value among high-subsonic aircraft [18]. A taper ratio $\lambda = 0.3$ enables to approach an elliptical lift distribution, which is the configuration that minimizes the induced drag produced by the wingtip vortices as shown by Prandtl in the lifting line theory [19]. The resulting chord lengths are respectively 12.81 ft at the root and 3.84 ft at the tip of the winglets.

Twist angle. The washout angle prevents the wing tip to stall before the wing root. It is thus necessary to apply one on the *MWET* aircraft family. A common value for the twist angle is -3° for high-subsonic aircraft [18],and provides adequate stall characteristics.

Anhedral angle. The value of the anhedral angle is chosen based on common values that are applied on other high-wing aircrafts [18]. Therefore, the anhedral is equal to 3°.

4.1.b Airfoil Selection

The choice of the airfoil is driven by the velocity at which the aircraft flies during cruise, as it is the longest phase of the flight. A supercritical airfoil is the most consistent choice for a high-subsonic flight because it has the particularity to increase the drag-divergence Mach number, so that an excessive increase in drag is prevented even in the case of a cruise speed very close to the critical Mach number.

Moreover, one important characteristic of airfoil families is that they are designed to fly in the range around their optimal angle of attack in order to stay in their drag bucket. This optimal angle of attack is close to 0°. A particularity of supercritical airfoils is that this additional constraint is all the more true since the drag increases much faster than common airfoils as the angle of attack moves away from the optimum. Indeed, the example of the NASA SC(2)-0714, which is the chosen airfoil as it will be further discussed, can be used to illustrate that when the lift coefficient exceeds the design lift coefficient (i.e. $c_l = 0.7$), the drag coefficient blows up, which has a negative impact on the performance of the aircraft. Therefore, it is preferable to give an incidence angle to the wing as close as possible to 0° so that in cruise, i.e. when the angle of attack of the aircraft is 0°, the drag remains small as can be seen in Figure 4.3.

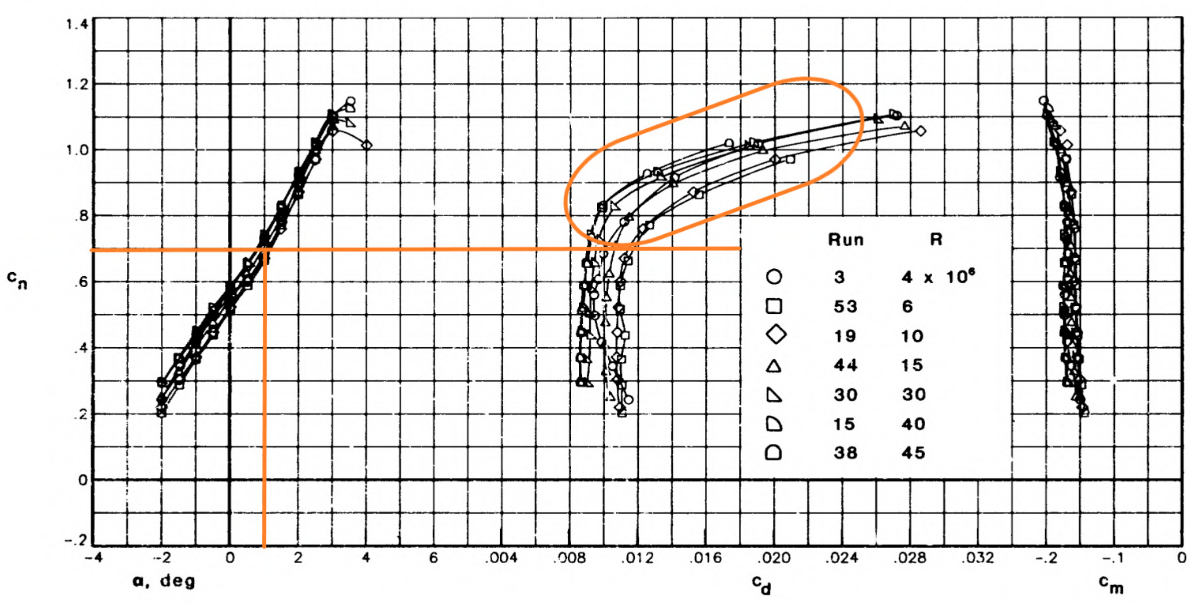

$M = 0.72$.

Figure 4.3: Experimental data for the NASA SC(2)-0714 airfoil presenting the lift, drag and moment coefficients as a function of the angle of attack for various Reynolds number, at $M = 0.72$ [20].

The next step is to find an airfoil that would give to the aircraft the required lift force to ensure equilibrium at mid-cruise and full-payload (i.e. design point) as it is defined in [4] for a small angle of attack. Therefore, the NASA supercritical airfoil family is investigated by comparing the evolution of the lift-to-drag coefficient with respect to the lift coefficient and also the lift coefficient curve with respect to the angle of attack, for *MWET*'s 3D wing with different NASA supercritical airfoils. Among them, the NASA SC(2)-0714 stands out as the wing produces the required lift at very small angles of attack, and its thickness ratio of 14% provides some room for fuel storage as well as some robustness. The curves from Figure 4.4 are built thanks to empirical correlations [4] which enable to take into account all the geometric parameters as well as the airfoil's geometry (i.e. NASA SC(2)-0714) [20]. One main equation can be defined to link the 2D lift coefficient of the airfoil with the 3D one of the entire *MWET* aircraft, recalled below;

$$C_{Lw} = \frac{2\pi}{\beta\left(\frac{2}{\beta AR} + \sqrt{\left(\frac{1}{\frac{\beta c_{l,\alpha}}{2\pi}\cos\Lambda_\beta}\right)^2 + \left(\frac{2}{\beta AR}\right)^2}\right)}\left[\alpha_{\text{root}} - (\alpha_{l_{0_{\text{root}}}} + \alpha_{01}\varepsilon_{a,\text{tip}})\right] \tag{4.1.1}$$

Where β is the compressibility factor, AR is the aspect ratio, $c_{l,\alpha}$ is the 2D lift curve slope, Λ_β is the corrected sweep angle by β, α_{root} is the angle of attack at the wing root, $\alpha_{l_{0_{\text{root}}}}$ is the zero-lift angle of attack of the airfoil, α_{01} is the local aerodynamic twist and $\varepsilon_{a,\text{tip}}$ is the aerodynamic twist which is equal to geometric twist in the *MWET* aircraft.

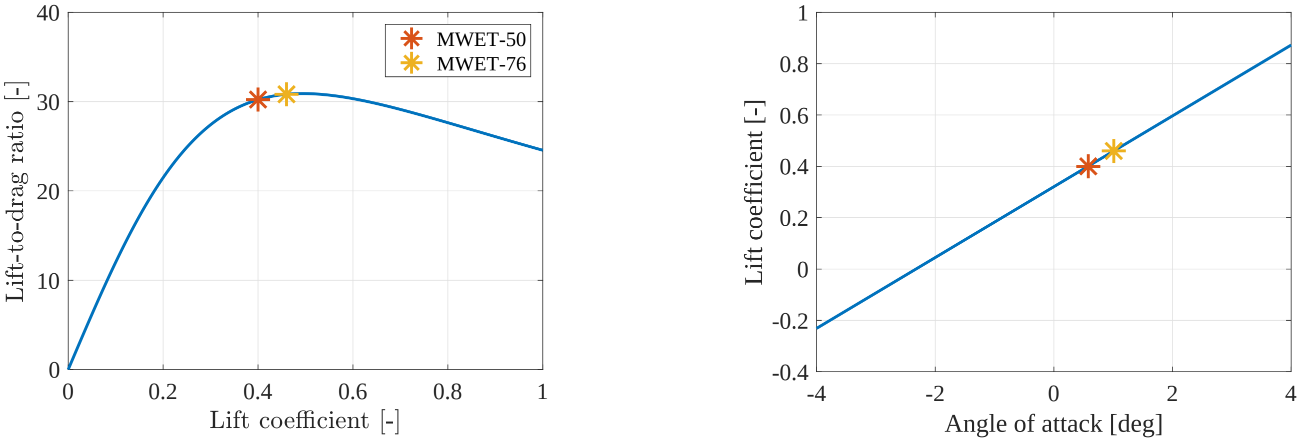

Figure 4.4: Lift-to-drag coefficient with respect to the lift coefficient (left) and lift coefficient with respect to the angle of attack (right) of the 3D wing with the NASA SC(2)-0714 with empirical correlations.

It can be seen that for the lift coefficient at the design point (i.e. required to ensure equilibrium at full-payload and mid-cruise [4]), the lift-to-drag ratio is close to the maximum one that can be provided by the wing. Moreover, the lift curve with respect to the angle of attack (Figure 4.4 (right)) illustrates that the wing can provide the required lift coefficient at an angle of attack almost equal to zero, which is expected. To summarize, the chosen airfoil is the **NASA SC(2)-0714**. Its characteristics are gathered in Table 4.1, where $\left(\frac{t}{c}\right)_{max}$ is the maximum thickness ratio, $\mathbf{c}_{\mathbf{l},\alpha}$ is the 2D lift curve slope, α_{l_0} is the angle of attack for which the airfoil produces no lift, $c_{l,max}$ is the 2D maximum lift coefficient reachable by the airfoil before stall and, finally, c_m is the moment coefficient with respect to the quarter-chord.

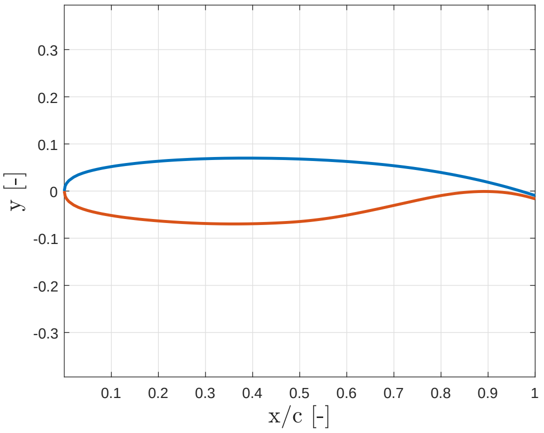

Figure 4.5: Geometry of the wing profile section [20].

	NASA SC(2)-0714
$C_{L,design}$ [-]	0.7
Design Mach [-]	0.72
$\left(\frac{t}{c}\right)_{max}$ [%]	14
$c_{l,\alpha}$ [1/rad]	11.5
α_{l_0} [deg]	-3
$c_{l,max}$ [-]	1.9
c_m [-]	-0.15

Table 4.1: Characteristics of the wing profile section [20].

Sweep angle. The cruise Mach number is chosen with respect to the mission requirements at 0.8. Since the *MWET* family will fly in a transonic regime, it may occur that at some points of the wings, the flow becomes sonic, which would alter the performances of the aircraft if it exceeds its drag-divergent Mach number. That is why on all transonic aircraft, a sweep angle is applied. Indeed, when the wings are effectively swept backward, the velocity actually seen by these stays close to the design Mach of the airfoil, which is the point at which it is the most efficient. Therefore, the sweep angle can be evaluated as:

$$\Lambda_{c/4} = \arccos\left(\frac{M_{DESIGN}}{M_{CRUISE}}\right) \approx 25.8^\circ. \tag{4.1.2}$$

Incidence angle. The angle (i_W) at which the wing is fixed on the fuselage is determined based on design point defined above. It is chosen in order to keep the fuselage parallel to the flow during most of the flight to minimise its drag force. A first approximation has been determined thanks to empirical correlations [4] in order to demonstrate that the wings are in the good range of angles of attack. However, more accurate values of these angles of incidence will be computed in the aerodynamic analysis of the wings (Section 5.2). Table 4.2 summarises those results.

	MWET-50	*MWET-76*
Angle of incidence [deg]	0.58	1
Lift coefficient in cruise [-]	0.4	0.46
3D lift coefficient derivative [rad^{-1}]	7.9	7.9

Table 4.2: First approximation of the angles of incidence and characteristics of the wings of *MWET-50* and *MWET-76* with empirical correlations; the required lift coefficients are determined to ensure equilibrium at mid-payload and mid-cruise.

From these results, it can be deduced that the wings are in the good range of angles of attack given that both angles of attack stay in the drag bucket around 0°.

4.1.c Flexible Winglets

The use of flexible winglets is mainly based on the work of Castrichini and Wilson with their project *AlbatrossOne* at Airbus Company [15]. A major concern of the current aircraft market is to reduce the CO_2 emissions of the future generation of aircraft but also their fuel consumption. A serious obstacle for the fuel consumption reduction of aircraft is induced drag, inversely proportional to the aspect ratio of the wing [19];

$$C_{D,i} = \frac{C_L^2}{\pi \, AR \, e}, \tag{4.1.3}$$

where $C_{D,i}$ is the induced drag coefficient, C_L the lift coefficient, AR the aspect ratio and e the Oswald efficiency factor.

Therefore, a quick way to significantly reduce this drag component is to increase the aspect ratio. However, on common aircraft, the larger the aspect ratio, the larger the loads at the wing-fuselage junction which implies that it has to be drastically reinforced. Consequently, this unavoidable reinforcement has a direct negative impact on the aircraft weight and thus, on its performance.

The biomimicry enabled to develop the idea of a flexible winglet. It has been demonstrated by Castrichini and Wilson that the dynamic loads produced by the increase of the span could be alleviated by the hinge's flexibility of the winglets. Indeed, the static and dynamic loads to which the winglets are subjected are almost not transferred to the main wing as the aircraft "surfs" through wind gusts. Airbus' engineers illustrate in their case study that a 25% increase in span using flexible winglets resulted in almost no increase in loads (about 4%). Obviously, this increase in span would directly increase the aspect ratio for a same surface, thus considerably decreasing the induced drag which is the objective of this innovative technology.

In the case of *MWET*, the flexible winglets and more particularly the hinge stiffness is designed to transfer exactly the necessary lift in cruise such that the winglets are just in continuity of the wing during this phase of flight. It means that in case of gusts or manoeuvres, the pressure differentials on the winglets result in higher or lower loads than the ones for which the rigidity of the hinge has been designed, thus they fold up or down. Another particularity of the flexible winglets it that they can be folded up at 90° in taxiing and at the airport. The different phases of the winglets are illustrated in Figure 4.6.

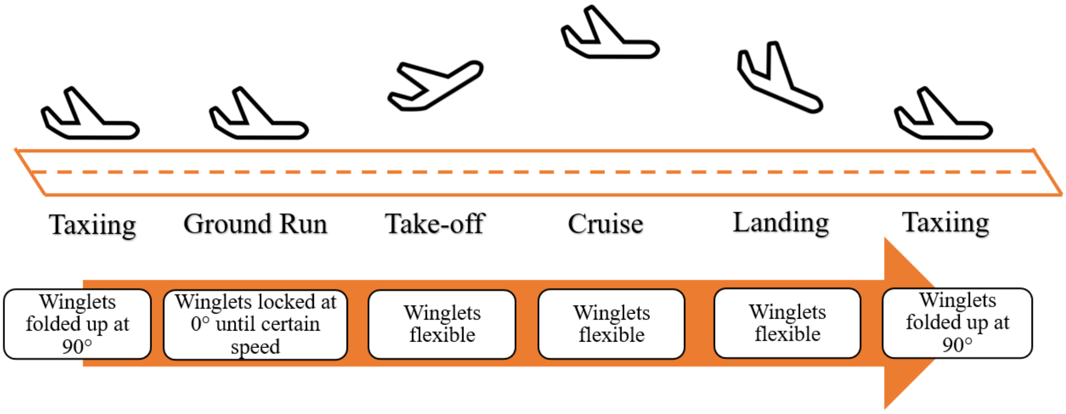

Figure 4.6: Different states of the flexible winglets from gate-to-gate.

Load alleviation, however, is only possible if the hinge line forms an angle with respect to the free stream [10]. An optimal value for this so called flare angle will thus have to be computed in next researches. Because such an angle is introduced, the most efficient position of the winglets in terms of drag is when they remain almost flat, as shows Figure 4.7. The hinge therefore needs to be designed such that this configuration is reached during cruise conditions. The following graph is built using a Steady Vortex Lattice Method code taking into account a compressibility correction. [21, 22].

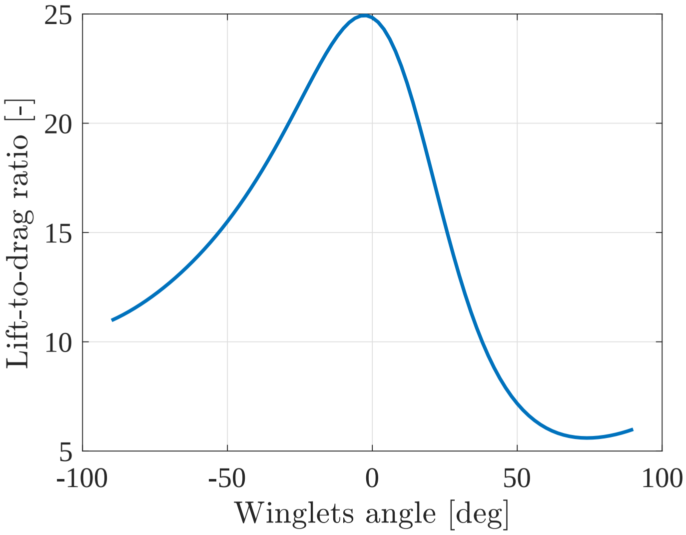

Figure 4.7: Evolution of the lift-to-drag coefficient ratio with respect to the deflection angle of the winglets with a hinge perpendicular to the quarter chord.

4.1.d Hinge Design

The objective of the hinge design is to estimate the torsion stiffness as well as the initial position of the torsion spring that is placed at the hinge. These estimations will enable to determine if the hinge is reasonable and feasible or if it is impossible to design such torsion spring. The flexible winglets and the hinge are represented in Figure 4.8 with all the forces that act on it.

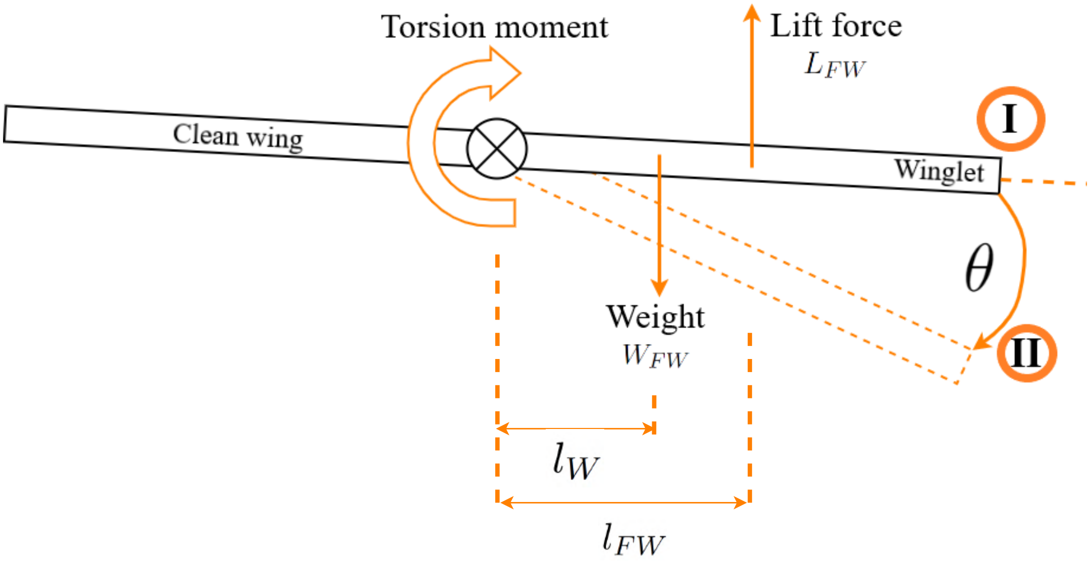

Figure 4.8: Simplified schematic of the winglet with its hinge.

Two situations, denoted by (I) and (II), can be highlighted.

I. The moment equilibrium is reached i.e. when the relation (4.1.4) is verified. In the *MWET* case, the moment equilibrium is wanted when $\theta = 0$.

II. The initial position of the torsion spring i.e. no force acts on the winglet.

Therefore, the moment equilibrium at the hinge can be written as,

$$\kappa(\theta - \theta_0) = L_{FW} \cdot l_{FW} - W_{FW} \cdot l_W\,, \tag{4.1.4}$$

where κ is the torsion stiffness of the spring, θ is the position of the winglet at equilibrium, θ_0 is the initial position of the spring, L_{FW} is the lift force, l_{FW} is the lift lever arm, W_{FW} is the winglet weight and l_W is the weight lever arm.

As stated previously, $\theta = 0$, the equation can be rewritten as follows;

$$-\kappa\theta_0 = L \cdot l_{FW} - W_{FW} \cdot l_W \tag{4.1.5}$$

From then on, the weight of the winglet is estimated to $W_{FW} = 355.7$ lbf based on the Section 4.9 by multiplying the total weight of the semi-wing and the ratio between the winglets surface and the total wing surface. Concerning the lever arm of the weight, the location of the center of gravity of the winglet is needed. However, it is still unknown at the stage of the design so it can be approximated to one third of the winglet length.

The second term that has to be determined is the moment due to the lift force. Since the wing of both *MWET* aircraft are not placed at the same incidence angle on the fuselage, the moment due to the lift generated by one winglet is different for the two aircraft. The software FLOW which is used in Section 5.2 can be used to determine the moment due to lift force.

	Moment due to lift force with respect to the hinge [ft.lbf]
MWET-50	≈ 14851
MWET-76	≈ 19942

Table 4.3: Different values of the moment generated by one winglet at the hinge.

Since all the moments are known, the Eq. 4.1.5 can be simplified for both configurations in,

$$\begin{cases} \kappa\theta_0 = -13490 \text{ ft.lbf}, & \text{for } \textit{MWET-50} \\ \kappa\theta_0 = -18581 \text{ ft.lbf}, & \text{for } \textit{MWET-76} \end{cases} \tag{4.1.6}$$

The torsion stiffness (κ) and the initial position (θ_0) of the spring can be tuned in order to obtain an initial position which tends to 0 while keeping a reasonable rigidity.

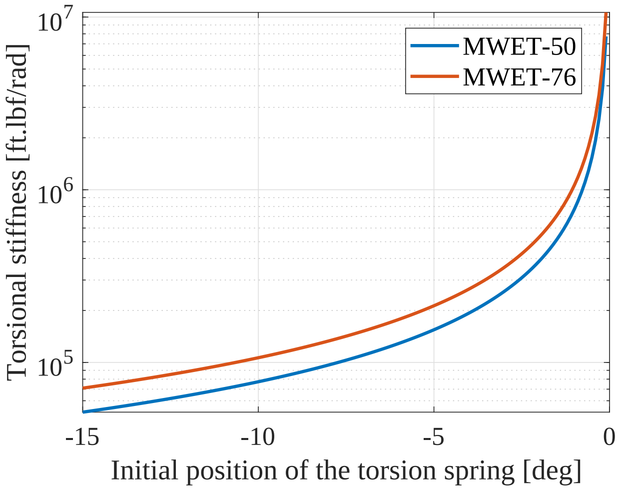

Figure 4.9: Evolution of the torsional stiffness of the hinge with respect to its initial position for *MWET-50* and *MWET-76*.

Based on these results, a comparison can be performed with the range of torsion stiffness proposed by the team working on the *AlbatrossONE*. They test some hinges with torsion stiffness from $7 \cdot 10^4$ to $7 \cdot 10^7$ $\frac{\text{ft.lbf}}{\text{rad}}$ [10]. Henceforth, it can be concluded that the range of stiffness illustrated in Figure 4.9 is quite conclusive and reasonable. The manufacture of such a torsion spring is realistic.

Another parameter that could be interesting to estimate is the mass of the hinge. The aim is to investigate the structural loads that the hinge could generate at the wing root, which could counterbalance a part of the lift during cruise as the engines do. A way to proceed is to review the commercialized torsion springs [23], which is done in Figure 4.10 (left) in order to determine an acceptable value of stiffness by unit of mass. From then on, a graph can be built up to illustrate the evolution of the mass spring with respect to the initial position of the spring. Thanks to the spring market review, it is concluded that a value of approximately 1681 $\frac{ft.lbf}{kg.rad}$ is a potential value that could be reached. It is important to keep in mind that the review of the commercial spring market has been performed thanks to spring catalogs which propose industrial springs made of heavy materials such as steel for example. Therefore, the mass of the hinge system is overestimated since lighter materials can be especially developed for aeronautical applications.

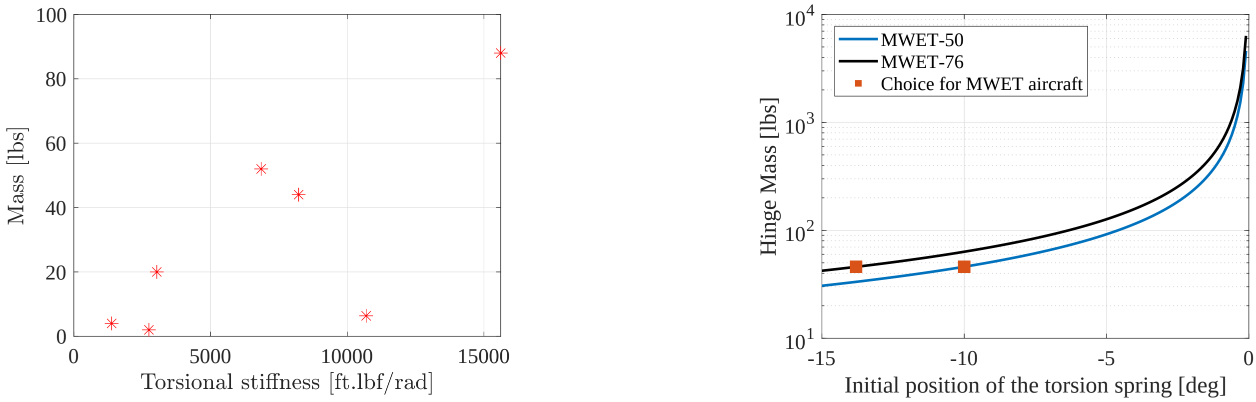

Figure 4.10: Evaluation of the spring mass with respect to its initial position thanks to a market review and definition of the configuration for both *MWET-50* and *MWET*-76.

As a conclusion, the mass of the hinge could be determined thanks to a market review of commercialized torsion springs for 50- and 76-seat configurations. It is chosen that the same torsion spring is used for *MWET-50* and *MWET-76* to continue to minimize the production costs by increasing the commonality between the two aircraft. In order to keep the added mass on the wing as low as possible while keeping the initial position as close as possible from 0°, the mass of the torsion spring is equal to $\approx$ 46 lb as can be seen in Figure 4.10 in the right graph. Consequently, the spring's initial position of the *MWET-50* is -10° and the *MWET-76*'s is -13.8° which stays in the range that has been defined in Figure 4.7. To summarize, the hinge characteristics are recalled in the Table 4.4.

	MWET-50	*MWET-76*
Initial position [°]	-10	-13.8
Torsional stiffness [ft.lbf/rad]	7.7e+04	
Hinge mass [lb]	46	

Table 4.4: Principal characteristics of the hinge mechanism.

However, the configuration I. is determined based on the cruise conditions corresponding to the design point (i.e. at full-payload and mid-fuel) but the equilibrium position varies if the *MWET* aircraft are flying in off-design conditions. Henceforth, the flexible winglets have to fold up or down in order to return in moment equilibrium with respect to the hinge.

For this reason, it is important to check that the equilibrium positions stay around 0° to minimize the increase in drag in off-design conditions with the chosen hinge characteristics as it has been shown in Figure 4.7. Two critical cases are considered to prove that even if the flight conditions is changed, the equilibrium positions are close from 0° and thus, that the drag remains small. The first one is the case of a full-payload and full fuel flight and the second one is the hypothetical case with no fuel and no payload. In order to determine the lift moment produced in those two cases, FLOW is used. The latter is a full potential equation solver which will be described in more details mater. Since the hinge characteristics are known, the Equation (4.1.4) can be reassessed to determine the new equilibrium positions with respect to the one evaluated thanks the design point for both aircraft. The results are illustrated in the Figure 4.11.

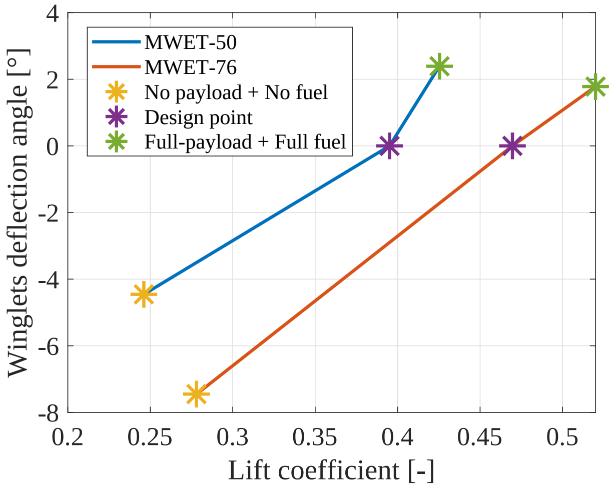

Figure 4.11: Evolution of the winglet deflection angle with respect to the flight conditions for both configuration using FLOW.

It can be concluded that even if the flight is in off-design conditions, the deflection angles with respect to the equilibrium position based on the design conditions stay small such that the drag is not significantly increased. Indeed, from Figure 4.7 and 4.11, it can be computed that the lift-to-drag ratio does not vary more than $\approx 5\%$ with respect to the design point when *MWET-50* and *MWET-76* are flying in off-design conditions. Consequently, it can be deduced from these results that the hinge is well-designed for the *MWET* flight cases.

As a conclusion, the hinge design is approximated as being a torsion spring, thus further investigations will have to be performed in order to determine exactly what it is needed and which type of mechanism will be used. In addition, it is important to proceed to an aeroelastic study of the wing with the flexible winglets to assess the behavior of them in a subsonic flow.

4.2 Empennage

The empennage is composed of two parts: the horizontal tail and the fin. It ensures the trim, stability and control of the aircraft. The horizontal tail provides longitudinal trim by compensating the pitching moments coming from several sources, such as the wing. The fin counteracts yawing moments to ensure lateral stability.

The sizing methodology of the empennage is inspired by [18] and [24]. The empennage is designed with the optimizing tool of EXCEL. The objective is to minimize the drag and the weight of the empennage, while fulfilling the static stability and trim requirements. The limits used for this optimization have been chosen with statistics from similar aircraft and typical ranges of values given in [18] and [24]. It is common for aircraft families to reuse the wing and empennage from an aircraft family to another, as it can be seen, for example, in the Embraer ERJ family.

The horizontal tail design results from an iterative process between the geometrical parameters and the longitudinal equilibrium. The force equilibrium equation and the pitching moment around the center of gravity (CG) equilibrium equation are reminded in Equations (4.2.1) and (4.2.2). x_{CG} is the distance between the nose of the aircraft and the center of gravity of the aircraft, x_{AC_w} the distance between the nose of the aircraft and the aerodynamic center of the wing, $\bar{\bar{c}}$ is the mean aerodynamic chord of the wing and l_T is the distance between the center of gravity and the aerodynamic center of the horizontal tail. The last ratio is also called the *tail volume coefficient*. Given that the horizontal tail has a symmetrical airfoil, its moment coefficient is null ($C_{m_T} = 0$). Both equations are adimensional and the moment are considered positive when the aircraft pitch up.

$$C_{L_w} + C_{L_T} \frac{S_T}{S} - mg = 0 \tag{4.2.1}$$

$$C_{m_0} + C_{L_w} \frac{x_{CG} - x_{AC_w}}{\bar{\bar{c}}} + C_{m_T} - C_{L_T} \frac{S_T l_T}{\bar{\bar{c}} S} = 0 \tag{4.2.2}$$

In the following section, the limits used for the optimization are specified and the final results given are the ones resulting from the iterative process described earlier.

4.2.a Empennage Planform

The geometry of the empennage of *MWET-50* and *-76* is the same. The geometry of the horizontal tail is shown in Figure 4.12. The geometry of the fin is shown in Figure 4.13.

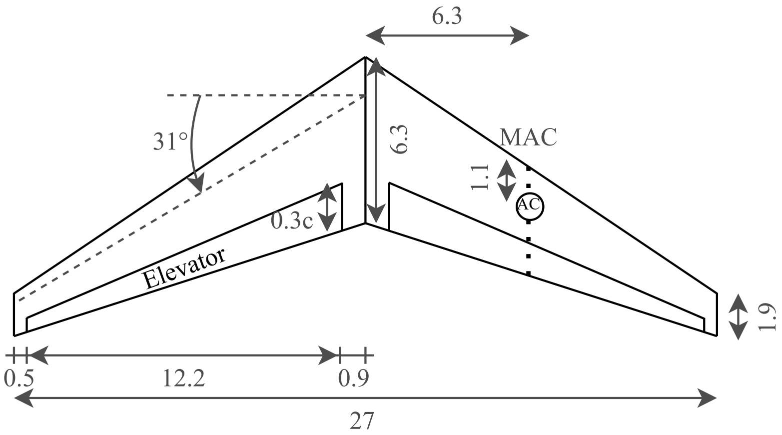

Figure 4.12: *MWET-50* and *-76* horizontal tail planform [ft].

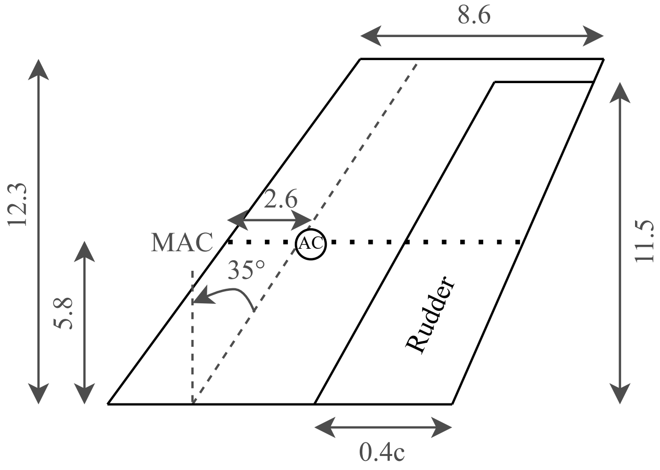

Figure 4.13: *MWET-50* and *-76* fin planform [ft].

Span. According to statistics gathered on similar aircraft (EMB 145, CRJ 200, etc), it appears that the horizontal tail span is usually about a third of the wing span while the fin span is about a sixth of the wing span. A 20% margin is used to derive the limits used for the horizontal tail and the fin design. The span of the horizontal tail (b_T) is of 27 ft and the span of the fin (b_F) is 11.5 ft.

Aspect ratio. The aspect ratio of the horizontal tail is often included in [3;6] [4], and for the fin of a T-tail it is included in [0.7;1.2] [18]. The aspect ratio is $AR_T = 6$ [-] for the horizontal tail and $AR_F = 1.16$ [-] for the fin.

Tail area. The ratio of the horizontal tail surface and the wing surface is often included in [0.2;0.4] [4]. In addition to this limit, the horizontal tail surface has to be consistent with the chosen aspect ratio. This latter condition is also valid for the fin surface. The surface of the horizontal tail is $S_T = 122.10$ ft^2 ($S_T/S = 0.21$) and the surface of the fin is $S_F = 130.64$ ft^2.

Taper ratio. The horizontal tail taper ratio is often similar or lower than the wing taper ratio and is usually included in [0.3;0.6] [24]. Given those two conditions, the only value possible for the taper of the horizontal tail is $\lambda_T = 0.3$ [-]. The taper of T-tail fin is included in [0.6;1] [18]. $\lambda_F = 0.7$ [-] finally came out of the iteartive process.

Sweep angle. The sweep angle at quarter chord of the horizontal tail has to be at least 5° higher than the one of the wing to avoid shock waves, and, for transport jets, it never exceed 40° [18]. The quarter chord sweep angle of the fin is often of about 30° to 40° [4]. The quarter chord sweep angle of the horizontal tail is $\Lambda_{1/4,T} = 31^\circ$ and the one of the fin is $\Lambda_{1/4,T} = 35^\circ$.

Twist angle and dihedral angle. The horizontal tail hardly ever features a twist angle and a dihedral angle. For the sake of symmetry, the fin is never twisted and never has a dihedral angle. They are thus set to 0° for both the horizontal tail and the fin for both *MWET-50* and *-76*.

Tail volume coefficient. A last criterion that is often used in empennage design is the tail volume coefficient. This coefficient is a non-dimensional measure of the aerodynamic effectiveness of the tail. Some methodology for empennage design [25] are entirely based on this coefficient. For the *MWET* family of aircraft, the tail volume coefficient was used as the last limit in the optimization process to verify that the horizontal tail and the fin are well-designed.

$$\overline{V}_T = \frac{S_T\, l_T}{S\, c_{\mathrm{MAC}}} \qquad \text{and} \qquad \overline{V}_F = \frac{S_F\, l_F}{S\, b} \tag{4.2.3}$$

The tail volume coefficient is defined for the horizontal tail and the fin in Equation (4.2.3), where $l_{T,F}$ is the lever arm of the horizontal tail/fin with respect to the center of gravity, $S_{T,F}$ is the tailplane surface, S is the wing surface, c_{MAC} is the wing aerodynamic chord and b is the wing span. In the final configuration of the empennage, the coefficients are given in Table 4.5. According to Raymer [18], for a T-tail, the typical tail volume coefficient can be reduced by 5% for the horizontal and vertical tail due to the end-plate effect and the improved flow. This criterion is met for *MWET-50*. The tail volume coefficient is larger for *MWET-76* given the larger lever arms, but is close to the typical range of values. This ratio takes its importance in the equilibrium equations. The fact that the ratio is slightly out of the range for $MWET - 76$ is not an issue as long as the equilibrium criterion is fulfilled.

Tail volume coefficient	*MWET-50*	*MWET-76*	Typical values [18] [24]
$\overline{\mathbf{V}}_{\mathbf{T}}$ [-]	1.18	1.38	[0.95; 1.2]
$\overline{\mathbf{V}}_{\mathbf{F}}$ [-]	0.08	0.09	[0.07; 0.09]

Table 4.5: Horizontal and vertical tail volume coefficients for *MWET-50* and *MWET-76*.

4.2.b Airfoil Selection

The geometry of the empennage is far less complex than the one of the wing, because less critical. While the wing produces almost all the lift needed to allow the aircraft to fly, the horizontal tail produces just the required amount of lift needed to keep the aircraft in a trimmed configuration. The lift coefficient of the horizontal tail is most of the time close to zero during cruise. To decrease the manufacturing cost, symmetrical airfoil of the NACA four-digit family are commonly used for the horizontal tail. The thickness of the airfoil is taken the lowest possible for three main reasons. First, a thinner airfoil lowers the weight of the horizontal tail, which is important so that the fin can support it. Then, flight condition in cruise are close to the transonic regime, which means that shocks can occur. A thin, swept wing (or horizontal tail in this case) is less likely to generate shocks. Finally, the thinner the airfoil, the lower the drag. The optimizing process depicted earlier leads to the choice of a **NACA-0008** airfoil.

To preserve the symmetry of the aircraft, symmetrical airfoils of the NACA four-digits family are used for the fin. The airfoil of the fin has to be thicker than the one of the horizontal tail to provide enough mechanical strength to support the horizontal tail, while remaining thin enough to avoid increasing dramatically the drag and the weight of the aircraft. A **NACA-0012** is finally selected. The characteristics of the airfoils of the horizontal tail and the fin are summarized in Table 4.6.

	Horizontal tail airfoil	**Fin airfoil**
Maximum thickness ratio, $\left(\frac{t}{c}\right)_{\max_{T,F}}$ [%]	8	12
2D lift curve slope, $c_{l,\alpha_{T,F}}$ [rad^{-1}]	6.02	6.11
Zero-lift angle of attack, $\alpha_{l_{0,T,F}}$ [deg]	0	0
Maximum 2D maximum lift coefficient, $c_{l,\max_{T,F}}$ [-]	1.2	1.55
Moment coefficient (w.r.t quarter-chord, $c_{m_{T,F}}$ [-]	0	0

Table 4.6: Characteristics of the horizontal and vertical tail profile sections [26]

4.3 Control Surfaces

The control surfaces are essential for the control of the aircraft. The lift can be adapted to the needs of the aircraft to remain in equilibrium or perform a manoeuvre by deflecting the control surfaces. Their design is mainly based on statistics but also on the requirements concerning the take-off and landing distances. The validity of the design can be verified for a critical case of flight.

4.3.a High-Lift Devices

Several flaps configurations can be used. Ranking them by increasing aerodynamic efficiency but also increasing mechanical complexity, it exists split, plain, single-slotted, double-slotted or Krueger flaps, to name a few. At first, the maximum lift coefficient of the wing must be determined, in order to quantify by how much the flaps must increase the lift. To do so, a correlation from [4] is used:

$$C_{L,max} = \cos\Lambda_{1/4}\, 0.95\, \frac{(c_{l\,\max})_{\text{root}} + (c_{l\,\max})_{\text{tip}}}{2} = 1.6245 \text{ [-]}, \tag{4.3.1}$$

where $(c_{l\,\max})_{\text{root}} = (c_{l\,\max})_{\text{tip}}$ because the airfoil remains the same along the span. Then, based on the methodology described in an open educational resource for Hamburg Open Online University (HOOU) [27] and assuming that the kinematics of the flaps does not influence much their performance, one can obtain a value of the increase of the maximum lift coefficient provided by the flaps $\Delta C_{l,max,f}$ using the formula

$$\Delta c_{l,max,f} = k_1\, k_2\, \left(\Delta c_{l,max}\right)_{base} \text{ [-]}, \tag{4.3.2}$$

where $\left(\Delta c_{l,max}\right)_{base}$ is the maximum increase in the lift coefficient for a flap with a 25% flap chord at a reference flap angle, k_1 is a correction factor which takes into account a relative flap chord that has a value other than 25%, and k_2 takes into account a flap deflection that differs from the reference value.

Still based on the methodology of [27], the increase in 3D lift coefficient can then be expressed in terms of the 2D lift increase, accounting for the sweep angle and the surface of the flaps:

$$\Delta C_{L,max,f} = \Delta c_{l,max,f}\,\frac{S_{W,f}}{S_W}\,K_\Lambda, \tag{4.3.3}$$

where $\Delta c_{l,max,f}$ is obtained from Eq. (4.3.2), K_Λ is an empirical correlation factor for taking into account wing sweep, and $\frac{S_{W,f}}{S_W}$ is the area ratio for the flaps ($S_{W,f}$ considers the area of the flaps as if they covered the entire chord).

It is decided that the use of **doubled-slotted** flaps without any leading-edge device is the best configuration. They provide sufficient lift coefficients to take-off and land safely within the requirements, contrarily to single-slotted flaps which make it impossible to respect approach speed category C (< 141 kts). Furthermore, the addition of slats was assessed following the methodology described in [27]. Even though the combination of single-slotted flaps and slats increases the performance in terms of take-off and landing with respect to double-slotted flaps, the mechanical complexity and cost of such leading edge devices make this increase not worth it. Finally, the use of double-slotted flaps is in line with what is done in the industry [28].

The length of the flaps is set to 19.7 ft so that they cover the maximum span available, considering that some space must be left for the ailerons and high-lift or control devices cannot be mounted on the flexible winglets. Moreover, a small security margin of 0.8 ft is left between the flaps and the fuselage. The flap-chord ratio is 30%, while the deflection angles are set to respectively 20° and 50° in takeoff and approach. Those values are in line with the optimal ones for double-slotted flaps, as stated in [27]. The resulting increase in maximum lift coefficient is thus maximized for a given area ratio and sweep angle. This lift coefficient increment leads to the values of $C_{L,\text{max}}$ which are summarized in Table 4.7.

	MWET-50/76
Maximum lift coefficient in cruise $(\mathbf{C_{L,max}})_{\mathbf{clean}}$ [-]	1.62
Maximum lift coefficient at take-off $(\mathbf{C_{L,max}})_{\mathbf{to}}$ [-]	2.17
Maximum lift coefficient in approach $(\mathbf{C_{L,max}})_{\mathbf{app}}$ [-]	2.43

Table 4.7: Maximum lift coefficients of the wing with 19 ft long and 30% chord double-slotted flaps, deflected by 20° at take-off and 50° in approach.

4.3.b Ailerons Design

In the design of the ailerons, four main geometric parameters have to be determined: the aileron planform area (S_a), the aileron chord over span ratio ($\frac{c_a}{b_a}$), the maximum up and down aileron deflection ($\pm\delta_{A,\text{max}}$) and the location of the inner edge of the aileron along the wing span (b_{ai}). Figure 4.14 illustrates geometrically the link of these different parameters on a standard wing. However, as it can be observed in Figure 4.2, the *MWET* wings are composed of two parts: the first one is the clean wing and the second one is the winglets. Therefore, for the sake of roll controllability, the ailerons should be placed before the hinge with

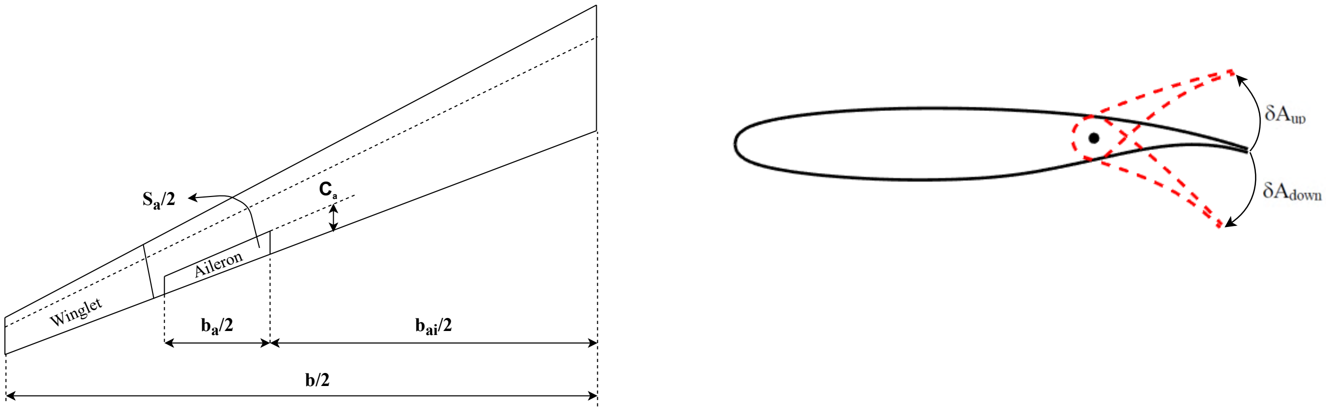

Figure 4.14: Geometry of the ailerons on the *MWET* semi-wing.

respect to the wing root.

Some statistical data have been collected on a series of airliners concerning the geometric parameters of an aileron [24]. Therefore, some guidelines about the aileron design can be deduced and are summarized in Table 4.8.

As illustrated in Figure 4.2, it is assumed that the flaps and the ailerons can be placed side by side based on the assumption that the mechanisms do not need space in between.

From this point, the length of the ailerons (b_a) can be arbitrarily set from the end of the flaps to 0.8 ft before the hinge to keep room for the hinge of the winglets and then, $b_a = 16.4$ ft. Moreover, the location of the inner edge of the aileron (b_{ai}) is also known from the assumption that has just been made which is equal to 50.8 ft. To finish, the aileron-to-wing-chord ratio is set at 30% to keep the ailerons in alignment with the flaps, which also have a ratio of 30%. Although this value is higher than statistical data computed thanks to a large range of airliners, it stays close from the general guidance (cfr. Table 4.8). With all these parameters, the ailerons surface can be computed thanks to following equation;

$$S_a = 2 \times \frac{(c_{\text{inner}} + c_{\text{outer}}) \times \frac{b_a}{2}}{2} \approx 88 \text{ ft}^2, \tag{4.3.4}$$

with c_{inner} and c_{outer} respectively the chord at the inner and outer edge of the aileron. The statistical range of the geometrical parameters [24] can be compared with those which are estimated.

	Statistical range	*MWET* ailerons
Aileron-to-wing-area ratio $\frac{S_a}{S}$ [-]	5-10%	15%
Aileron-to-wing-chord ratio $\frac{c_a}{c}$ [-]	15-25%	30%
Aileron-to-wing-span ratio $\frac{b_a}{b}$ [-]	20-30%	18%
Inboard aileron-to-wing-span ratio $\frac{b_{ai}}{b}$ [-]	60-80%	55%
Maximum deflection angle $\pm\delta_{A,max}$	±30°	±30°

Table 4.8: Comparison of the aileron's geometric parameters with statistical values determined on existing airliners.

From Table 4.8, it can be deduced that thanks to the choices that are made on the ailerons' geometry, the *MWET* ailerons are almost in the same range as its competitors. Indeed, the aileron-to-wing-area ratio and the aileron-to-wing-chord ratio are a little bit higher than the common range but they are compensated by a lower aileron-to-wing-span ratio and also a lower inboard aileron-to-wing-span ratio. However, it is not a problem because engineers from *Airbus* who are working on flexible winglets claimed that this innovative technology enabled a better roll control which would help the ailerons for the turns [16].

4.3.c Elevators

Elevators ensure longitudinal control. They are fully described by four main geometric parameters: the elevator planform area (S_E), the elevator chord (c_E), the elevator span (b_E) and the maximum up and down elevator deflection ($\pm\delta_{E,max}$).

For the sake of simplicity, the geometrical parameters of the elevator are normalized with the geometrical parameters of the horizontal tail. The design of the elevator of the *MWET* family of aircraft is based on statistics coming from general cases and similar aircraft. The arbitrarily chosen ratios are summarised in Table 4.9 and the actual dimension of the elevators are shown in Figure 4.12.

	Statistical range	***MWET* elevators**
Elevator-to-tail-area ratio $\mathbf{\frac{S_E}{S_T}}$ **[-]**	15-40%	27%
Elevator-to-tail-chord ratio $\mathbf{\frac{c_E}{c_T}}$ **[-]**	20-40%	30%
Elevator-to-tail-span ratio $\mathbf{\frac{b_E}{b_T}}$ **[-]**	80-100%	90%
Maximum deflection angle $\delta_{\mathrm{max},E}$	$\pm20°$-$\pm25°$	$\pm25°$

Table 4.9: Comparison of the elevator's geometric parameters with statistical values determined on existing airliners [18] [24].

4.3.d Rudder

The rudder is the control surface located on the fin. It is responsible for the aircraft lateral control. Its geometry is fully described by four main geometric parameters: the rudder planform area (S_R), the rudder chord (c_R), the rudder span (b_R) and the maximum up and down rudder deflection ($\pm\delta_{R,max}$).

Once again, those values are expressed as ratios with respect to the fin parameters for the sake of simplicity. *MWET-50* and *-76* use a swept rudder, which is the same for both configurations. The rudder is designed following the methodology described in section 12.6 of [24]. This methodology leads to the rudder geometry described in Table 4.10. Those ratios are compared to usual values. The actual quantities of the rudder are shown in Figure 4.13.

The design of the rudder is validated by considering a critical case of flight. The most critical case for the rudder of a twin-engine engine aircraft is the case of an asymmetric thrust, so the case of a take-off with one engine inoperative. The rudder deflection needed to counteract the moment coming from the remaining engine is estimated with Equation (4.3.5). T_L is the thrust of the remaining engine, y_T is the distance between the remaining engine and the fuselage centerline and V is the lift-off velocity. $C_{\mathrm{n}_{\delta R}}$ is the aircraft yawing moment coefficient due to rudder deflection derivative. It depends strongly on the fin size and the fin moment arm. The angle of deflection of the rudder needed for the case of a take-off with one engine inoperative is lower that the maximum angle allowed for both *MWET-50* and *-76*.

$$\delta_{\mathrm{R}} = \frac{T_{\mathrm{L}} y_{\mathrm{T}}}{-\frac{1}{2}\rho V^2 S b C_{\mathrm{n}_{\delta R}}} \tag{4.3.5}$$

	Statistical range	*MWET* elevators
Rudder-to-fin-area ratio $\frac{S_R}{S_F}$ [-]	15-35%	37.2%
Rudder-to-fin-chord ratio $\frac{c_R}{c_F}$ [-]	15-40%	40%
Rudder-to-fin-span ratio $\frac{b_R}{b_F}$ [-]	70-100%	93%
Maximum deflection angle $\delta_{\max,R}$	±30°-±40°	±40°

Table 4.10: Comparison of the rudder's geometric parameters with statistical values determined on existing airliners [24].

4.4 Engines

The propulsion system is an important part of the design. On the one hand, the provided thrust has to power the aircraft during all phases of the flight with a special focus on the critical phases such as takeoff with one failing engine. On the other hand, the weights of the engines, the fuel and the nacelles directly affect many other components including the stability.

4.4.a Reduction of greenhouse gas emissions

Firstly, a discussion about the sources of energy to power an aircraft is performed. New technologies are coming up to reduce the greenhouse gas emissions (GHG) of the aeronautical world.

Sources of energy. Carbon-based fuels such as kerosene or gasoline have been used for decades in aviation thanks to their high energy density. However, they are a major contributor to GHG emissions. The *MWET* family of aircraft has been developed such that they are more efficient and they reduce GHG emissions. The latter goal could potentially be achieved using different sources of energy such as hydrogen, sustainable aviation fuel, solar energy transformed in electricity stored in batteries.

In the near future, most of these technologies would have been hardly implemented in regional aircraft. The available quantity of information, studies and data have not allowed to consider them to power an aircraft of this size, except for sustainable aviation fuel (SAF) which is frequently used blended with kerosene fuel since 2008 [29]. The final decision has been to use an existing turbofan with this mixing fuel powering the engines. It allows to decrease the impact of the aircraft on the environment. Following the International Air Transport Association (IATA), SAF have been identified as one of the key elements in helping achieve emissions reduction goals in the aviation sector [30]. Considering the availability of sustainable aviation fuel, some airports have already made the first move to offer the possibility to airlines to use SAF during their flights such as Oslo airport [31].

Certifications. For now, the SAF is a drop-in replacement to conventional jet fuel. These fuels are defined such that they are entirely fungible with conventional kerosene requiring no adaptation of engines or associated delivery infrastructure. This is verified by the American Society for Testing and Materials (ASTM) certifications such as D1655/7566 respectively for aviation turbine fuels [32] and for aviation turbine fuels containing synthesized hydrocarbons [33]. They also make sure that any fuels used by the industry are, in fact, sustainable from feedstock to function. At the same time, prescreening tools[2] and procedures are now developed to minimize cost, fuel volume, program risk, and time requirements [35].

Performance. In a recent lifecycle analysis of greenhouse gas from renewable jet fuel production, De Jong *et al.* [36] have reported that it is possible to achieve significant emissions reductions with new sustainable aviation fuels conversion pathways compared to the actual certified production processes. Thanks to more freedom in the production processes, fuel's composition can be adapted in order to reduce GHG emissions or to improve performances. For example, by obtaining higher specific energy and energy density. Indeed, Kosir *et al.* [37] have studied a subset of sustainable aviation fuel, high-performance jet fuel, that improves the value and performance of the fuel while reducing greenhouse gas emissions and remaining within drop-in operability, safety limits and ASTM constraints. At the same time, Feldhausen *et al.* [38] have shown that there could even be general performance benefits from addition of biofuel with improved GHG emissions while minimizing the cost that is still higher than actual Jet A fuel for now.

Cost. In order to reduce the high cost that mainly comes from the production technologies, the development of technologies that maximize carbon conversion efficiencies for a reduced cost is essential. Tanzil *et al.* [39] have conducted detailed techno-economic analyses of six SAF production technologies in. At the end, they have proposed a new scheme for SAF production that could result in yields close to those needed to achieve cost targets.

In conclusion, this drop-in technology is promising to reduce significantly greenhouse gas emissions for a cost that is expected to decrease during the next years. At the same time, performances could even be improved compared to actual kerosene fuel. For all these reasons, it can reasonably be assumed that sustainable aviation fuel will be available worldwide for future clients.

4.4.b Engine Selection

First, a quick market analysis is performed. A good indicator for engine selection is the choices that have already been made for similar aircraft. Given all certifications considering the sustainable aviation fuel and the drop-in technology, the engine can be selected from similar existing aircraft. A few of them are presented in Table 4.11. The maximum thrust values are taken from the manufacturers datasheet and expressed in terms of uninstalled thrust. In this work, the installed thrust has been computed using the assumptions from [4] and [18] which provide, in the worst case, a loss of thrust of around 8% compared to the uninstalled value at static sea level.

The weight, as well as the fuel consumption, are critical parameters for the engine selection. As a matter of fact, the engines are designed specifically for the cruise and, consequently, they consume the least amount of energy during this segment. However, regional missions have a short haul, and thus a short cruise. For example, the increase of weight, and thus of the total fuel needed, coming from an heavier but less consumptive engine, could not be compensated during cruise. A compromise between the weight and the specific fuel consumption has to be made.

Another useful parameter is to ensure that the provided thrust allows the aircraft to fly at all the phases of the flight. As a matter of

---

[2] Prescreening novel SAF candidates refers to testing or predicting key fuel properties and performance metrics before entering the formal ASTM D4054 Standard Practice for Evaluation of New Aviation Turbine Fuels and Fuel Additives [34].

	Static SL thrust [lbf]	T/W [-]	TSFC [lb/h lbf]	BPR [-]	Overall length [in]	Diameter [in]	Dry mass [lbs]	Aircraft
GE CF34-3	9220	5.52	0.69	6.2	103	49	1670	Bombardier CRJ200
R-R AE3007A1	9500	5.6	0.69	5	115	55.7	1665	ERJ135/140/145
GE CF34-8	13790-14500	5.7-6.1	0.67-0.68	5	128	52	2450	Bombardier CRJ700/900/1000, ERJ170/190
P&W PW800 series	**12000-15000**	**3.86-4.83**	**0.55**	**5.5**	**130**	**50**	**3105**	**Gulfstream G500/600, Dassault Falcon 6X**
P&W PW1700G	14000-17000	3.95	0.54	9	113.5	62	3800	E-Jet E2 175
R-R Pearl 15	15125	3.77	0.57	4.8	189	48.5	4032	Bombardier Global 5500/6500

Table 4.11: Engines for similar aircraft.

fact, the total available takeoff field length and the cruise velocity requirements represent critical design points as the engine must provide enough thrust to reach these requirements. The takeoff field limit is the most critical case in term of available thrust, as the *MWET* family aircraft must perform this phase of flight taking into account an event of one engine failure. The latter requirement leads to a lower bound of static takeoff thrust around 21,400 lbf and 22,400 lbf using balanced field length of 4000 ft and 6000 ft for the *MWET-50* and *-76* respectively with an obstacle clearance height of 50 ft. Regarding the amount of thrust needed to perform the cruise segment at Mach 0.8 and at a cruise altitude of at least 32,000 ft, the 50- and 76-seats configuration must provide at least 3591 lbf and 4032 lbf in order to perfectly compensate the drag force acting on the aircraft.

After a comparative analysis between the different possibilities of engines for the *MWET* aircraft family, two existing configurations of the PurePower PW800 from the new family of Pratt & Whitney are finally chosen. These engines are the **PW812D** and **PW814** respectively for the *MWET-50* and *-76*. The trade-off analysis is available in Table 4.12. As it can be seen in the Table 4.12 that the CF34-3 and AE3007A1 do not respect the maximum required takeoff field length in the event of one engine failure above the decision speed (OEI section 5.4.a).

4.4.c Engine Characteristics

According to MTU Aero Engines [40], the PW800 series comes with numerous improvements. A double digit improvement (-10%) is expected for the fuel consumption, the environmental emission (NOX, etc), the engine noise and, finally, the operating cost with respect to similar thrust-class engines available on the market. It also has the significant advantage of providing 40% less scheduled maintenance and demanding 20% fewer inspection. The PW800 is designed for long range business jets, regional

Engines	T-O field length / OEI [ft]	Land. field length [ft]	$W_{f,cruise}$ [lbs]	$W_{f,total}$ [lbs]	W_0 [lbs]
PW812D	3206 / 3868	3687	7625	12,010	56,200
CF34-3	+15.5% / +29%	-15.8%	+17.7%	+14.4%	-3.1%
AE3007A1	+12.6% /+23.3%	-14.6%	+16.1%	+ 13.3%	-3.3%
PW814	4165 / 5003	4003	9400	14,700	70,637
CF34-8	-1.6% / -2.5%	+2.8%	+21.2%	+16.2%	-1.3%
PW1700G	-1.5% / -7.1%	+7%	+3%	+2.3%	+3.1%
Pearl 15	+0.5% / -0.4%	+5%	+4.4%	+3.7%	+4.4%

Table 4.12: Comparison between selected engines for *MWET-50* (upper part) and *-76* (lower part) with respect to similar regional used turbofan engines. The red values represent requirements that are not respected.

airline like *MWET* and single aisle aircraft. The engine is composed of 24 blisked fan blades. The gear-less PW800 shares a common core with the larger geared PW1000G which leads to a significant reduction of the dry mass.

The announced specific fuel consumption of the listed engines in the table 4.11 are evaluated, by manufacturers, at Mach 0.8 for an altitude of cruise around 35,000 ft. As the mission cruise altitude for the *MWET* aircraft family is around 32,000 ft, a correction must be applied on the specific fuel consumption in order to be closer to the reality. This TSFC can be computed as a function of the Mach number as developed in [41],

$$\mathrm{TSFC} = \mathrm{TSFC}_0 \sqrt{\theta}(1+M)^n \tag{4.4.1}$$

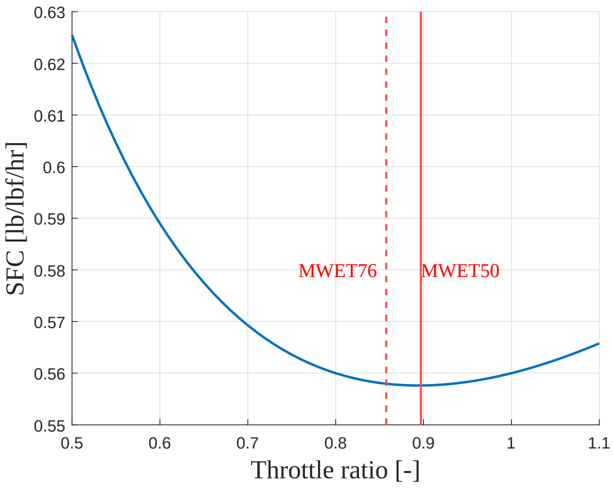

Figure 4.15: Specific fuel consumption in function of the throttle ratio at 32,000 ft and Mach 0.8.

where TSFC_0 is the static sea level ISA installed thrust SFC, the exponent n is equal to 0.8 in order to fit with experimental results obtained for high by-pass ratio turbofans (BPR > 5) and θ is the temperature ratio. TSFC_0 is around 0.4 lb/lbf/hr for current turbofan engines. Actual engines are developed to consume the least amount of fuel in cruise condition. However, resulting from this design point, the consumption at sea level is far from the optimum. The specific fuel consumption for the *MWET* aircraft family is rounded to 0.56 lb/lbf/hr in the *MWET* aircraft family cruise altitude. The specific fuel consumption depends on the altitude, the velocity reached and on the throttle ratio. The effect of the latter on the fuel consumption is represented in the Figure 4.15 for a steady cruise flight. It can be seen that the optimal point takes place around 90%, where the SFC is minimal. The red lines on the figure 4.15 characterized the needed throttle ratio to perfectly compensate the drag acting of the aircraft during the cruise for the 50- and 76-seats configuration. It can be seen that the applied thrust in cruise condition will be close to the optimal point for both aircraft of the *MWET* family meaning that the fuel consumption is minimal.

In this preliminary design study, the variation of the maximum available thrust in function of the altitude and the Mach number represents an unknown. However, using the thrust model of modern two-shaft turbofan engines developed by [42], an approximation of the available thrust for all the different flight segments can be found. These values are shown in the Figure 4.16 for each *MWET* seats configuration. For the sake of readability, only four Mach number are represented: the static case (Mach 0), the cruise one (Mach 0.8) and a range in which the takeoff will take place (between Mach 0.1 and 0.2). Using this method and as it can be seen in the Figure 4.16, the available thrust in cruise condition for the PW812D takes place around 2150 lbf per engine while the PW814 is equal to 2510 lbf. Regarding the thrust produced by the engines at takeoff, the PW812D will deliver a mean value, evaluated at 70% of the liftoff velocity [43], of 9740 lbf per engine. Similarly, the PW814 delivers in average 11,125 lbf. These values allow the *MWET* aircraft family to respect the requirements and the expected performance as shown in the Table 4.12.

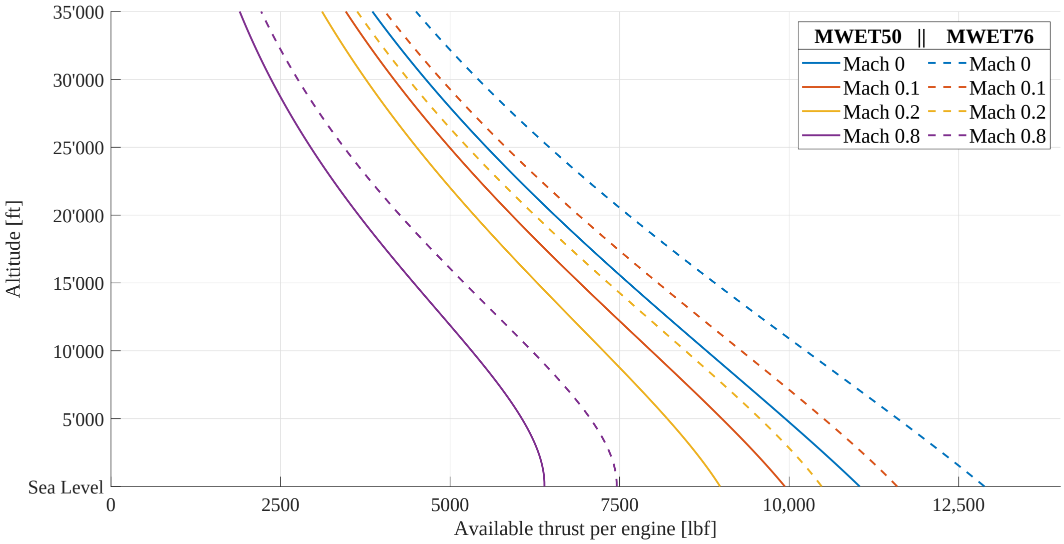

Figure 4.16: Available thrust per engine in function of the flight altitude and velocity.

The results shown in Figure 4.16 will be used to determine (in addition to the takeoff field length at sea level and the performance during cruise flight) the needed takeoff field length at 5000 ft above the sea level, the climb and turn performance as well as the performance for the alternate mission.

4.5 Fuselage

In this section, the different parts of the fuselage are presented in detail. More than containing the passengers, it contains the crew, the pilot, the on-board computer and the cargo compartment for the luggage. The landing gear are also in the cargo compartment during the flight. The first three sections presented here are the different portions of the fuselage.

4.5.a Cabin

The cabin is divided into four different parts in order to be properly studied.

Seat part. To define a correct length for the seat, Gudmundson's book [25] is used. The seats are modeled in order to be comfortable for a 6.2 ft person and to validate the AIAA requirement [1]. The latter gives a length for the seat of 30 in. The seat width is set to 20 in and the height is set to 55 in. All the seats are arranged in a two by two disposition. This disposition is chosen for its optimization of space. The aisle, of 20 in, is placed in the middle and thus there is no need for high ceiling on the side. For the *MWET-50* there are 13 rows (with the last one with only 2 seats) and for the *MWET-76* there are 19 rows of seats.

The diameter of the fuselage is determined by the size of the seats. In order to get a headroom of 6.6 ft and to be able to put 4 seats and the aisle, the interior diameter has been fixed to 114 in. The exterior diameter has been defined by taking the addition of the interior diameter and 4% of the interior diameter. It finally gives an exterior diameter of 118.6 in. This result is visualized in Figure 4.17.

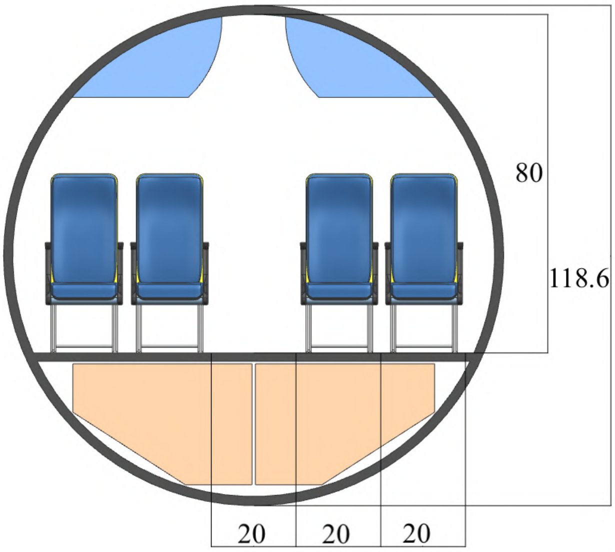

Figure 4.17: Schematic of the cabin [in].

Door part. The first door is the entrance door and is put just after the cockpit part. It is 60 in long to be able to put exit door of type A. This space is also used by the crew during the flight. The second door is of type I and is placed in the tail.

Bathroom part. Two lavatory are needed, following the regulation given by CFR [3], when there is more than 50 passengers. Both lavatory box are placed in a face to face position just after the seat part. They will be 2 seats wide and 38 in long. They can be visualized in Figure 4.18.

Crew part. This part takes into account the seats of the crew as well as the crew material (meal, drink, ...). It is 60 in long but does not take part in the cabin length. This part is put into the tail to reduce the length of the plane. Two exit doors of type *I* are put there too. In this way, the number of exit doors corresponds to the regulation given by CFR [3].

4.5.b Cockpit

The cockpit has a length of 16.4 ft to be 1.5 longer than the exterior diameter of the fuselage [4]. This is a condition in order to have a correct pressurization. The design of the cockpit is inspired from the Mitsubishi Spacejet [44] as it is the most advanced streamlined design present on the market, but is not as long. The window size and disposition has been defined to get a field of view for the pilot of: 12° down in the flight direction; 40° up in the flight direction; 130° on the side.

4.5.c Tail

The tail has a length of 19.7 ft to be 2 times longer [4] than the exterior fuselage. It has a conical shape, and its end has the shape of peak. The up-sweep angle is 13.4°[3]. The closure angle is 24°.

4.5.d Total Dimension

The final length of the fuselage are respectively 75.8 ft and 92.2 ft for *MWET-50* and *MWET-76*.

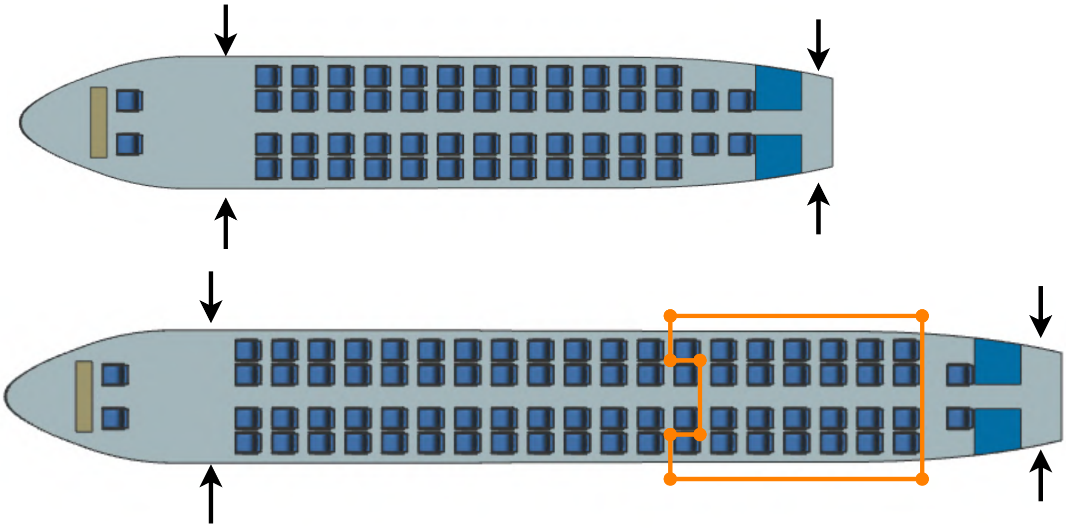

Figure 4.18: Fuselage of *MWET-76* with arrows to show where the door are positioned .

The configuration is presented in Figure 4.18. The hold volume is sufficient for the luggage of each passenger and landing gear. It is estimated at 459 ft^3 (681.5 ft^3 for *MWET-76*) by taking the section area of the cargo-hold and multiply it by the cabin length. 266 ft^3 are allocated for the luggage for the *MWET-50* and 396 ft^3 for the *MWET-76*, 87 ft^3 for the landing gear and the remained volume is used to stock the fuel.

4.6 Avionics

The avionics includes all electronics, such as the antenna and radar, the communication system, the navigation system, and all the instrument needed to control the aircraft.

In the cockpit, the avionics are related to the navigation and communication. For the communication, the pilot need a set of headset and an audio controller is also placed in the cockpit to manage the communication. The rest of the communication especially the antenna can be placed in the tail. The other instruments placed in the cockpit are related to the navigation. The on-board computer, the navigation system, some gyroscope or movement sensor are also present. All these instruments are displayed on screen on the dashboard. An head-up display can be used with Enhanced Vision System. The data recorder, also

---

[3] defined in more details in the landing gear part

known as the black box, can also be placed in the cockpit part. This one will record all the data of the flight and the audio. It is used in case of a problem during the flight to know what happened. Both seats inside the cockpit have a control system in order to fly the aircraft.

On the outside of the plane some systems included in the avionics are used. First of all, the light are an important part. Due to the CFR reglementation [3] lights are needed (anti-collision lights) on the wing to be visible at night or inside clouds and also for the landing. The other system that is needed on the wing but also on the rest of the plane is an anti-ice system. This one can be an electro-thermal system [45]. It is composed of a system of wires that will heat the surface of the plane and deice it. It can be placed on all parts of the aircraft, including the engine and its blades. All these avionics can be provided by only one society like Thales-Aeropsace [46] that has already provided family aircraft like CRJ or Boieng.

Sensors and system are required for the aircraft to be capable of VFR and IFR flight with an autopilot. VFR stand for Visual Flight Rules and IFR stands for Instrument Flight Rules. In VFR fly, the the visual meteorological conditions [3] (VMC) need to be maintained. The instrument need for this are an airspeed indicating system, an altimeter, a compass, an accurate watch (need to contain hours, minutes and second) a turn and slip indicator and finally an outside air temperature indicator. With the IFR, the flight can take place in zero visibility conditions from take-off to landing but need a flight plan. The waypoints and the airways have to be established. A minimum radar vectoring altitude and a well-known air traffic is also needed.

4.7 Landing Gear

The landing gear helps support the aircraft on the ground and allows it to taxi, take off and land. In this section, the design and positioning of the landing gear are discussed. In addition, the number and the size of the tires and the shock absorption mechanisms are presented.

4.7.a Configuration Selection

A fuselage-mounted tricycle landing gear has been chosen for the *MWET* family of aircraft. This configuration has several advantages. For example, it gives stability on the ground and improves forward visibility on the ground. However, the high wing regional aircraft has a fairing to retract the landing gear. Then, an oblique retractable landing system is used to have a small fairing that could decrease the drag force during a cruise.

4.7.b Landing Gear Location

The landing gear's length must be sufficient to avoid hitting the tail during take-off. The angle theta θ is the angle off the vertical from the main wheel position to the aft center of gravity. According to Raymer [18] to prevent the tail from hitting the ground in tricycle configuration, it must be always greater or equal than tip back angle α_{tb} and it should fall between 16-25 degrees. However, if the center of gravity is too far forward then the aircraft tends to nose over while if it is too far back the aircraft will ground loop. A typical value of takeoff angle of attack α_{to} is ranged between 10-15° and the formula can be written

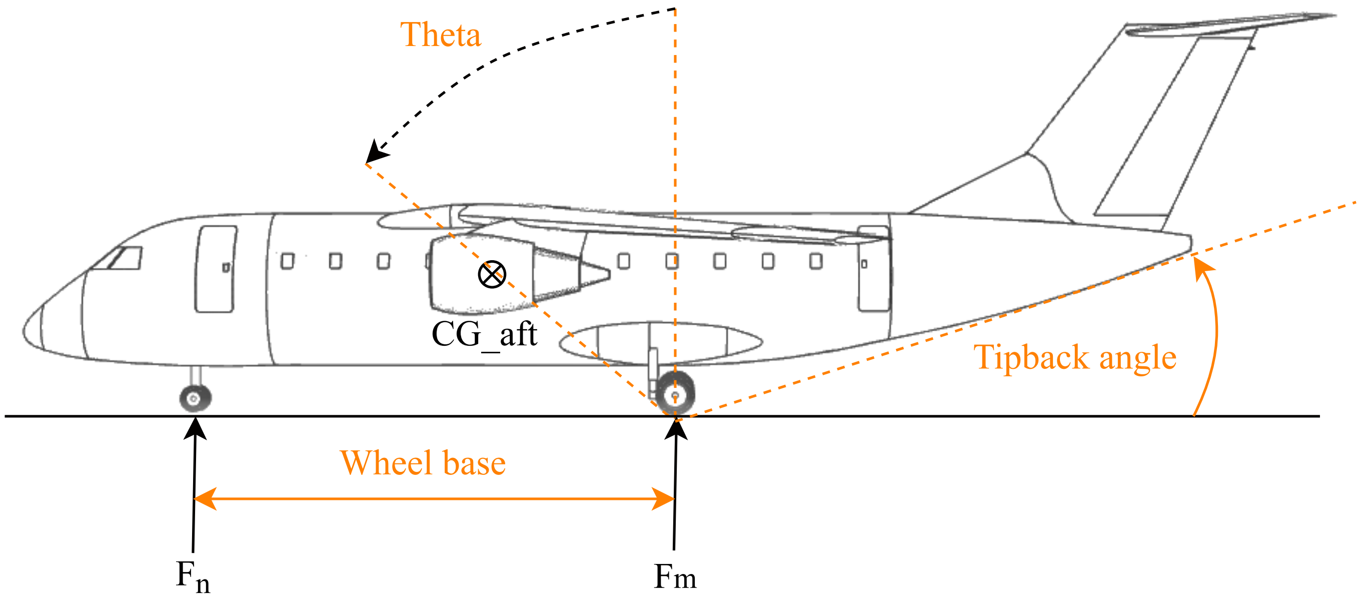

Figure 4.19: Landing gear configuration

as:

$$\alpha_{\text{to}} = \frac{1}{C_{\text{Lo}}} \left[(C_{l,\text{max}})_{\text{cruise}} - C_{l,\text{cruise}} - p(C_{l,\text{max}})_{\text{take-off}} \right] \tag{4.7.1}$$

where p is a margin approximated 0.15. The distance between the main gear and nose gear, which is called the wheelbase, B, has a major influence on ground controllability and ground stability of aircraft. Due to ground mobility, for example, steering during taxiing, the total weight W carried by the nose gear is between 8 to 15% while for the main gear it ranges between 85 to 92%. According to Curry [47], to have the first estimation of wheelbase B it was assumed that the static force at nose gear F_n = 10% of the gross weight and the static force at main gear F_m = 90% of the gross weight. The formulas can be written as:

$$F_m = \frac{B_m}{B} W \qquad \text{and} \qquad F_n = \frac{B_n}{B} W. \tag{4.7.2}$$

The wheel track (T) is the distance between the right main gear and left main gear and it has been arranged in a way that the aircraft can not roll over during ground turn or due to a sudden wind. The overturn angle Θ often ranges between $25^\circ \leq \Theta \leq 63^\circ$ [24]. A 60° has been chosen to compute the wheel track for both aircraft.

$$\alpha_{\text{track}} = \tanh \frac{0.5 \cdot T}{B} \quad \text{and} \quad \tan(\Theta) = \frac{H_{cg}}{L_n \cdot \sin \alpha_{\text{track}}} \tag{4.7.3}$$

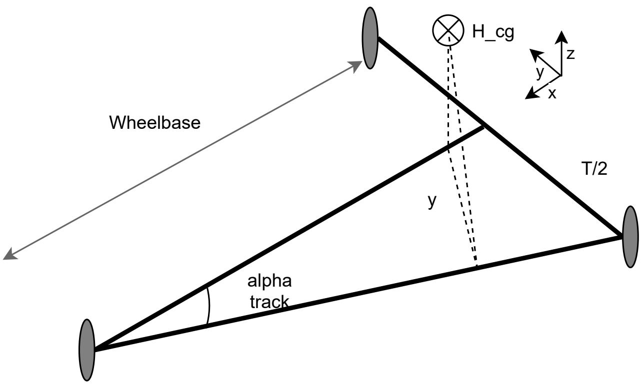

Figure 4.20: Front view of the undercarriage.

The wheel track geometrical relation can be seen in Figure 4.20.

The turning radius (Equation 4.7.4) are defined as the distance between the center of rotation and the various part of aircraft and it is as a function of gear steering angle β which is assumed to be 60°.

$$r = T\tan(90^\circ - \beta) + \frac{b}{2} \tag{4.7.4}$$

	MWET-50	*MWET-76*
Height of landing gear [ft]	3	3.6
Max angle at take off [deg]	12.32	10.7
Angle θ [deg]	20	25
Distance from sweep back to the main gear AB [ft]	15	19
Lm [ft]	3.8	3.96
Wheelbase [ft]	29.5	39.7
Overturn angle Θ [deg]	60	60
WheelTrack [ft]	10.6	11
Turning radius [ft]	21	26

Table 4.13: Geometrical parameters of tricycle landing gear.

4.7.c Tire Selection

The main gear has to support 90% of aircraft's gross weight and the nose gear has to support the remaining 10% [18]. In order to design the tires, the maximum static load on the gears is divided by the number of tires and a 25% growth factor is added to avoid costly redesign and to increase the safety in case of critical situation. The selected dimensions of tires from Michelin [48] can be seen in Table 4.14.

	MWET-50		*MWET-76*	
	Main gear	**Nose gear**	**Main gear**	**Nose gear**
Max static load [lb]	15350	3668.1	22500	5000
Tire diameter [in]	29	17.9	36	17.9
Tire width [in]	9.50	4.45	12	5.75

Table 4.14: Wheel geometry of the landing gear.

4.7.d Shock Absorber

By reviewing Raymer's book [18], the oleo-pneumatic shock strut is selected because it has the highest efficiency of all shock absorber types and also has the best energy dissipation. However, to design the shock absorber, some parameters have to be assumed. The vertical velocity (or "sink velocity"), V_{vertical}, at touchdown is assumed 6.7 mph for most aircraft, the efficiency of the fixed orifice ζ is ranged between 0.65-0.8, the efficiency of tire ζ_t is taken at 0.47 and the gear load factor for the commercial aircraft is $N = 2.7$ and S_t is the stroke of tire. The stroke is computed as:

$$S = \frac{V_{\text{vertical}}^2}{2g\zeta N} - \frac{\zeta_t}{\zeta} S_t \tag{4.7.5}$$

Note that this equation is independent of the weight of the aircraft and it should be increased by 1 in for safety margin then, $S =$ 0.08 [ft]. Typically, the total length of Oleo is selected 250% of S [18] .

4.7.e Landing Gear Material Selection

The material selection of the landing gear is critical since it is subjected to a large load during landing and it has to handle the entire weight of the aircraft on the ground. Therefore, The factors that were taken into consideration to select the material for landing gear are listed below:

- High strength density ratio
- Good corrosion resistance
- High fracture toughness
- High fatigue resistance

Composite materials are started to be used in some components of aircraft since it has high strength density ratio. Therefore, a new type of landing gear is demanded to avoid the constraints mentioned above. The most potential candidate that is selected is **Titanium Metal Matrix Composite** since it has high corrosion resistance and lightning strike resistance. According to RW [49], the results show that one could reduce the weight of landing gear by 32% but the cost increases two times production cost compared to the steel metal but the production cost will also be reduced in the near future. Some properties can be seen in Table 4.15.

Properties	Titanium Matrix Composite
Fibre	**Silicon Carbide**
Fibre strength [ksi]	478.4
Fibre stiffness [ksi]	47862.5
Price [$/lb]	200

Table 4.15: Properties of titanium matrix composite.

4.8 Electric Taxiing System (ETS)

The electric taxing system is aimed to reduce fuel consumption of aircraft during taxiing on the ground. Although, a lot of weight will be added to the total weight of the aircraft. First, it is good to highlight that total fuel that can be saved by **ETS system** depends on many factors, such as the type of aircraft, the total timing of taxiing, and the flight distance. Starting with the system arrangement, a direct drive motor is used to save a lot of mass that comes from the gearbox. On the other hand, the positioning of the motor was chosen to be on the main wheel, since this latter has a high vertical load, which gives good traction. Moreover, the main wheel has a robust structure that can accommodate the system more easily. A Permanent Magnet Synchronous Motor was selected for our system since this motor is known to have higher efficiency, higher torque density, higher power density compared to other types of motors, and also easy to construct and maintenance. Starting to compute the power needed to drive the aircraft at ground Newton's Law is used. The total force subjected to aircraft is:

$$F_{\text{total}} = F_{\text{inertia}} + F_{\text{roll}} + F_{\text{aerodynamic}} + F_{\text{slope}} \tag{4.8.1}$$

Where $F_{\text{aerodynamic}}$ is the drag force and is assumed to be zero since it is very small, F_{roll} = 1348.85 lbs is the friction, F_{slope} = 899.24 lbs is the force due to slope of the runway which is assumed 1.5 %. Moreover, the average velocity at the ground and the distance needed to cover was set as a constrain where v_{ground} has been assumed 18 mph (approximately 16 knots) and the distance to cover taxi in and taxi out is estimated 754 ft. According to Safran [50], the total time of taxi in and taxi out has been taken as an average of 30 minutes, it could be more in busier airport. Then, the power needed for **MWET-50** is 180 hp while for **MWET-76** is 200 hp and it is computed as:

$$P = V \cdot F_{\text{total}} \tag{4.8.2}$$

To power the electric taxiing system, a trade-off has been made between the **Lithium-ion battery** and **APU**. Table 4.16 is shown the total weight of the system in case of using the APU of aircraft and Lithium battery. The system arrangement can be seen in the Figure 4.21.

	MWET-50		*MWET-76*	
Components	*APU*	*Batteries*	*APU*	*Batteries*
Weight of two motors and cabling [lb]	641	641	641	641
Weight of two power converters [lb]	158	180	158	180
Additional weight of APU [lb]	125	/	167	/
Additional weight of battery [lb]	/	943	/	1178
Approximated total weight of ETS [lb]	924	1764	966	2000

Table 4.16: Estimated weight of the ETS system powered by APU and Lithium-ion battery.

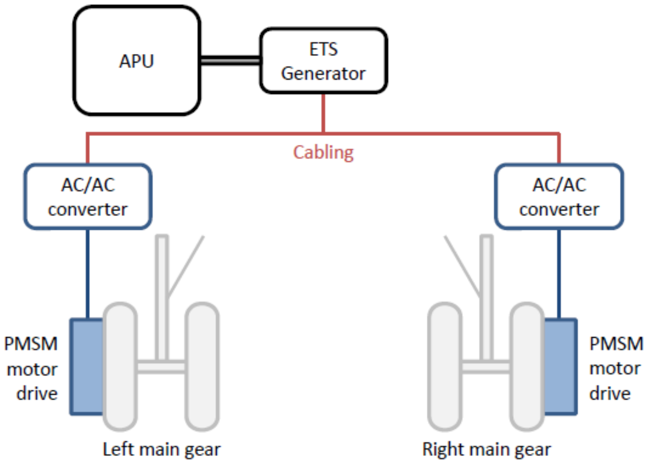

Figure 4.21: Illustration model of the ETS system.

PMSM Motor	Parameters
Torque density [in-lbs/lb]	307.577
Rated torque [in-lbs]	73012.5
Mechanical power [hp]	100.5

Table 4.17: PMSM motor properties

4.8.a Results

Adding about 1000 lbs weight to power the aircraft in case of using **APU** and 2000 lbs in case of using **Lithium-ion battery** would lead to a large increase in the amount of fuel consumed during the flight as in a short haul mission the total weight of fuel is really dependent of the takeoff weight. However, this system is used and developed to reduce fuel consumption when the aircraft is on the ground. The Table 4.18 shows the comparison between the *MWET-50/-76* using an ETS system, powered by the APU or by batteries, and the same aircraft without this device.

First, the fuel consumed by the aircraft during taxiing is computed. At this moment, the SFC is assumed equal to $1.5 \cdot \mathrm{SFC}_{\mathrm{dry}}$ ([18]) as the engines are in ground idle configuration, approximately 5% of the static takeoff thrust at sea level [51], and far away from their optimal operation point. For both cases, the total time spent on ground is assumed equal to 20 minutes (14 for taxi-out and 6 for taxi-in), which is not the worst announced case by Safran [50]. For the case where the ETS is used, the engines start-up is set around 3 minutes before the takeoff phase meaning that the ETS performs alone the motion of the aircraft during the previous minutes. Similarly, regarding the taxi-in, 3 minutes are needed to cool-down the engines just after landing before to shut-down the engines and use the ETS. The consumption for a typical APU is around 300 lbs/hr.

The total fuel consumed during taxi-in and taxi-out can be estimated knowing an approximation of the specific fuel consumption at ground idle thrust.

	MWET-50	*MWET-50 ETS (APU)*	*MWET-50 ETS (batteries)*	*MWET-76*	*MWET-76 ETS (APU)*	*MWET-76 ETS (batteries)*
Start & Taxi-out [lb]	495	157	118	575	174	135
Taxi-in [lb]	221	118	103	256	135	120
Cruise fuel [lb]	7426	7625	7613	9263	9400	9534
Total fuel per flight [lb]	12400	12010	12046	15180	14700	14826

Table 4.18: Comparison between *MWET-50/-76* aircraft without and with an ETS system.

Based on the Table 4.18 APU has been selected to power the ETS system where the total fuel that could be saved represents 3.2% of the total amount of fuel consumed which describes a money save of 310 and 381 dollars per flight respectively for the *MWET-50* and *-76* (price of fuel given in the section *Cost analysis*). This could save several hundreds of thousands of dollars per aircraft per year. However, this value can be increased in busier airport where the aircraft can take much more time during taxiing. On the other hand, there are other advantages of using this system. For example, the traffic flow on apron and at gates could be improved. Moreover, by using **ETS system** the towing tractors could be removed and this would save a lot of space in the airport.

4.9 Final Weight Estimations

The weight estimation of an aircraft is one of the most important steps of the conceptual design. The aircraft must be designed so that it can perform its intended mission carrying its intended payload. The weight estimation of each component relies on three different methods: empirical correlations [18], analytical solutions, and results from the CAD model. The takeoff gross weight W_0 can be decomposed on the one hand in a useful load part which includes occupants, fuel, freight, and on the other hand in an empty weight part, including the structure, the engines, the landing gear, the fixed equipment and the avionics. Considering the payload requirement of the AIAA synthetized in Table 4.19, the desired payload can be established as expressed in Table 4.20 including two pilots and their baggage supported by two flight attendants for the 50- and the 76-passengers configurations.

	Weight [lbs]
On board passenger	200
Pilot & cabin crew	190
Payload per passenger	40
Payload per pilot	30

Table 4.19: AIAA payload requirements.

	MWET-50	*MWET-76*
Passengers	50	76
Pilots	2	2
Cabin crew	2	2
Total payload [lbs]	12820	19060

Table 4.20: *MWET* payload.

Regarding the empty weight, it accounts for 55% and for 52% of the maximum takeoff weight of the *MWET-50* and *-76* respectively. For the sake of comparison, these weight fractions are in accordance with similar regional jet/midsized aircraft with 2 turbofan engines as expressed in [52].

Component weight

The weight of each component of the design can be computed using statistical equations based on regression analysis [18]. Components weights are depicted in the Table 4.21. The wing weight takes into account the estimated weight of the winglets as well as the guessed mass of the springs system used to fix the stiffness of the winglets in cruise and taxiing conditions

Component	*MWET-50*	*MWET-76*
Wing [lb]	4772	4772
Empennage [lb]	923	923
Fuselage [lb]	5986	7823
Landing gear [lb]	2227	3087
Propulsion system [lb]	7672	7672
Flight control system [lb]	999	1110
Auxiliary power unit [lb]	1153	1239
Instrument system [lb]	248	262
Hydraulic system [lb]	677	833
Electrical system [lb]	1646	1912
Avionics system [lb]	1235	1810
Fuel & oil system	417	524
Furnishings [lb]	2525	3700
AC & deicing [lb]	891	1210
Empty weight [lb]	31370	36877
Zero-fuel weight [lb]	44190	55937
Fuel weight [lb]	12010	14700
Takeoff gross weight [lb]	56200	70637

Table 4.21: Weight description of each component of the fixed design for the *MWET-50/-76* using the empirical correlations developed in [18].

(section 4.1.d). The propulsion system characterizes the installed configuration of the engines on the aircraft. This takes into account the weight of each engine, the nacelles and the starter. The fuel system represents the fuel tanks. In the same way, the auxiliary power unit, in this study, incorporates the APU for normal use of a regional aircraft and the required additional weight in order to integrate a electric taxiing system inside the aircraft. This additional weight was already mentioned in section 4.8 for both 50- and 76-seats configuration.

Center of Gravity and Inertia

The components of the aircraft and their respective weight have just been computed. Different flight configurations have to be taken into account by varying the payload and the fuel quantity. In fact, the fuel quantity decreases during the flight and the payload can vary from a flight to an other. The variation of the center of gravity is important to determine if the plane follows the stability requirements during the flight. The positioning of the components of the plane should aim to reduce as much as possible the variation of the center of gravity of the plane. Then by putting the reference frame to the nose of the aircraft, the center of gravity of these ones are gathered in the Table 4.22 and represented in Figures 5.1 and 5.2. The different configurations are defined as: at maximum take-off weight (MTOW), at mid-payload and mid quantity of fuel (mid-cruise), at the end of the cruise on the fuel reserve and mid-payload (end-cruise) and totally empty (empty).

	MWET-50	*MWET-76*
$\mathbf{x_{CG_{MTOW}}}$ [ft]	39.3	48.5
$\mathbf{x_{CG_{mid-cruise}}}$ [ft]	39.5	48.8
$\mathbf{x_{CG_{end-cruise}}}$ [ft]	39.6	48.9
$\mathbf{x_{CG_{empty}}}$ [ft]	39.7	49.3

Table 4.22: Position of the center of gravity for the different flight configurations.

The moments and products of inertia for the *MWET* family are assessed in the aircraft frame of reference with the CAD model. The longitudinal axis is the x-axis, the transversal axis is the y-axis and the vertical axis is the z-axis. The system is placed such that the x axis is located on the fuselage centerline. The values for the mid-cruise and mid-payload configuration are summarized is Table 4.24. Those values will be used in the equations of motion of the aircraft to asses its dynamic stability.

	$\mathbf{I_{xx}}$	$\mathbf{I_{yy}}$	$\mathbf{I_{zz}}$	$\mathbf{I_{xy}}$	$\mathbf{I_{xz}}$	$\mathbf{I_{yz}}$
MWET-50	129,890	377,282	476,104	10.3	- 26,877	-5
MWET-76	133,800	713,460	811,140	- 37.5	- 42,755	4

Table 4.24: Moments and products of inertia of *MWET-50* and *-76* at mid-cruise and mid-payload [$\mathrm{lb \cdot ft^2}$].

5 Aircraft Analysis

5.1 Stability

The stability of an aircraft is defined as the ability to remain or return in its equilibrium position after a perturbation. Of course, its flight dynamics must be such that unexpected phenomena do not lead to violent perturbations of the flight. On the other hand,

◕ Center of mass of the aircraft	2. ● Engines	5. ● Landing gear	8. ● Fin
● Neutral point	3. ● Seats + passengers	6. ● Wings	9. ● APU
1. ● Instruments	4. ● Fuselage	7. ● Fuel + luggage	10. ● Horizontal stabilizer

Table 4.23: Legend of Figures 4.22 and 4.23.

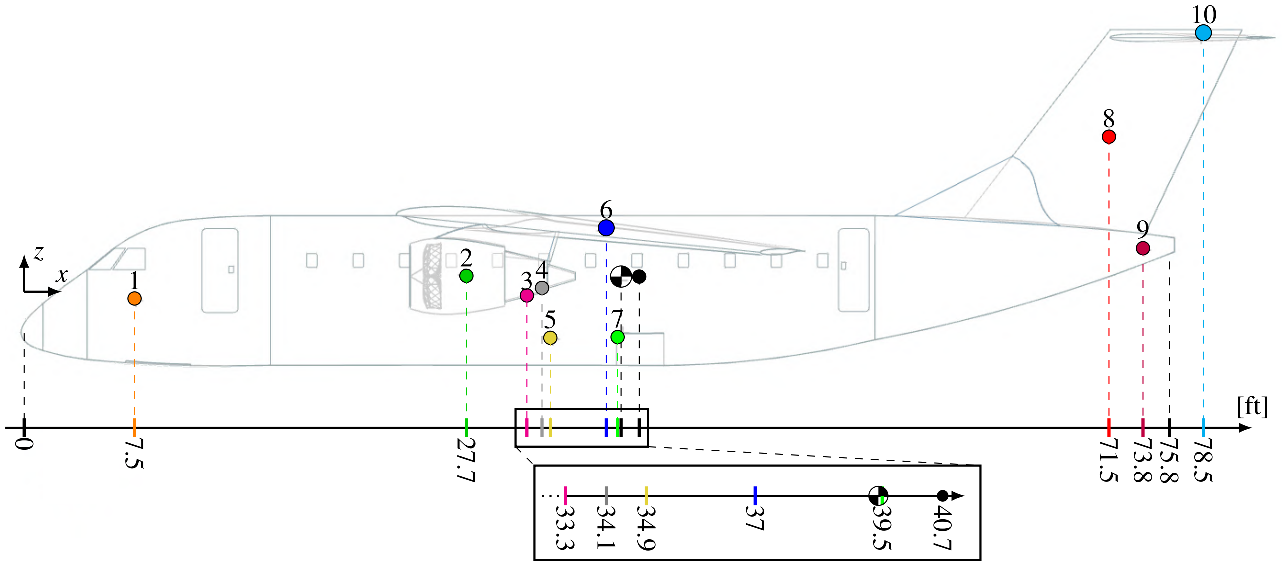

Figure 4.22: Center of gravity, neutral point and static margin variation for the *MWET-50*

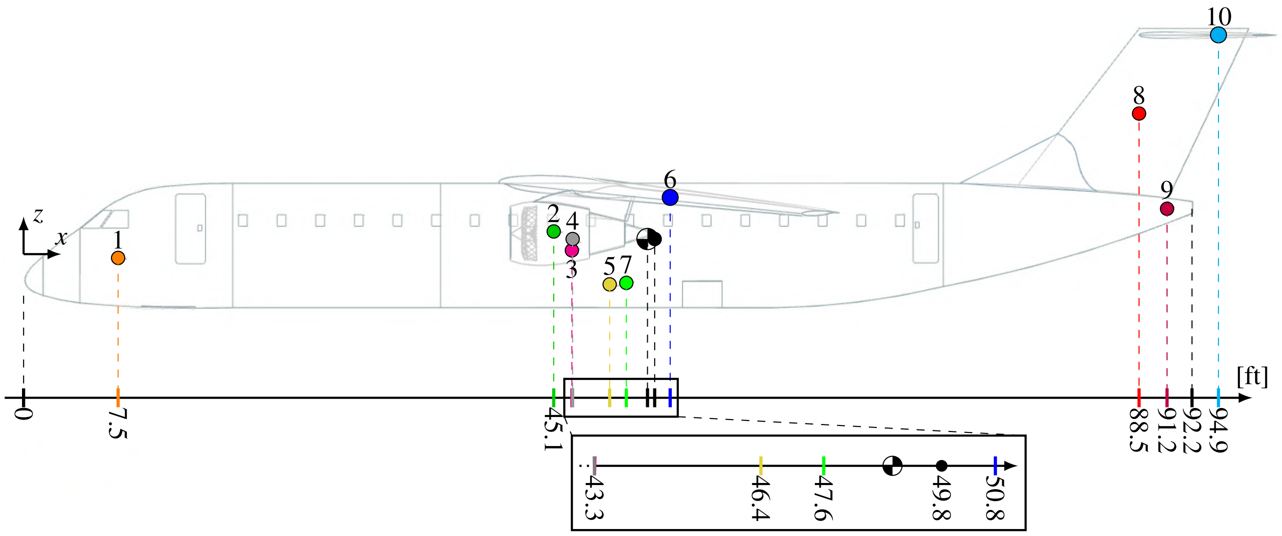

Figure 4.23: Center of gravity, neutral point and static margin variation for the *MWET-76*

the aircraft should not be too stable to remain maneuverable. Therefore, the stability is a compromise between the safety and maneuverability.

5.1.a Static Stability

Longitudinal Stability

The static stability is computed using the wind axis system following Kroo's methodology [53]. The longitudinal stability is characterized by the *static margin*, K_n, defined as the distance between the neutral point and the center of gravity normalized by the mean aerodynamic chord. It means that

$$K_n = h_n - h = -\frac{\partial C_m}{\partial C_{L_w}} \,. \tag{5.1.1}$$

The center of gravity of the aircraft can be found in the section 4.9. The neutral point is defined as the position of the center of mass where the aircraft would be neutrally stable (where $K_n = 0\%$). It is computed by considering the contribution of the wing, the tail and the fuselage.

The neutral point of the *MWET-50* and of the *MWET-76* are represented in Figures 5.1 and 5.2 respectively and are shown in the table 5.1.

	MWET-50	*MWET-76*
$\mathbf{x_n}$ [ft]	40.7	49.8

Table 5.1: Position of the neutral point from the nose of the aircraft.

According to the Federal Aviation Administration (FAA) [4] requirements for a T-tail, the aircraft are designed to obtain results in the range $K_n \in [5-20]\%$ to ensure enough maneuverability and stability at each moment of the flight.

Only the critical values of the center of gravity are kept to compute the static margin. They correspond to the MTOW and empty cases (defined in section 4.9. The static margin are gathered in the Table 5.2 and are represented in Figures 5.1 and 5.2.

	MWET-50	*MWET-76*
$\mathbf{K_{n_{MTOW}}}$ [%]	20.0	19.2
$\mathbf{K_{n_{empty}}}$ [%]	14.8	7.4

Table 5.2: Static margin for different flight and loading configurations.

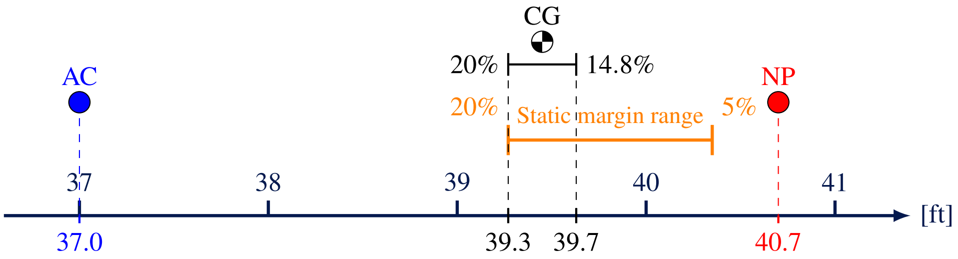

Figure 5.1: Static margin and center of gravity variation of the *MWET-50* along the longitudinal direction.

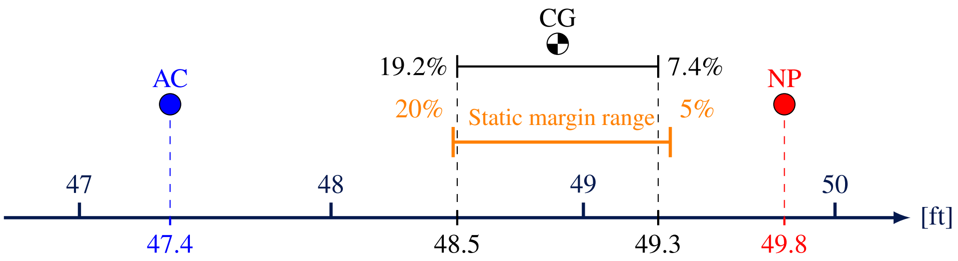

Figure 5.2: Static margin and center of gravity variation of the *MWET-76* along the longitudinal direction.

Directional Stability

The directional stability is the tendency of the aircraft to return to its original direction in with respect to to the freestream. In other words, it describes the stability in yaw. Mathematically, the requirements can be expressed as

$$C_{n_\beta} = \frac{\partial C_n}{\partial \beta} > 0, \tag{5.1.2}$$

and $C_n = 0$ if $\beta = 0$. C_{n_β} is the yawing moment derivative with respect to the sideslip angle β. Similarly to the longitudinal stability, a compromise has to be made to be stable and maneuverable enough. The values for the total directional stability must stand in the range of [0.04 0.4] rad^{-1} [24].

In order to obtain the total yaw moment derivative of the plane, the contribution of the wings, the fuselage and the fin have to be summed such as:

$$C_{n_\beta} = C_{n_{\beta,w}} + C_{n_{\beta,fus}} + C_{n_{\beta,fin}} \tag{5.1.3}$$

By following again Kroo's methodology [53], these contributions can be computed. As the aircraft have high-mounted wings, the wing contribution is set to $C_{n_{\beta,w}} = -0.017$. The fuselage effect causes a destabilizing yawing moment of $C_{n_{\beta,fus}} = -0.165$ and $C_{n_{\beta,fus}} = -0.220$ for the *MWET-50* and *MWET-76* respectively. Finally, the fin is designed to ensure a sufficient stabilizing contribution in order to fit in the range [0.04 0.4] rad^{-1} [24]. The contribution of the fin is equal to $C_{n_{\beta,fin}} = 0.499$ and $C_{n_{\beta,fin}} = 0.560$ for the 50 and 76 passengers aircraft respectively. It gives the total directional stability of the aircraft and they are gathered in Table 5.3.

	MWET-50	*MWET-76*
$\mathbf{C_{n_\beta}}$ [rad^{-1}]	0.317	0.323

Table 5.3: Total directional stability.

5.1.b Dynamic Stability

The dynamic stability is defined as the time history of an aircraft response after it has been disturbed [52]. The linearized equations of motion of a rigid spacecraft can be written with a state-space formulation as:

$$\dot{\mathbf{x}} = \mathbf{A}\mathbf{x} + \mathbf{B}\mathbf{u}, \tag{5.1.4}$$

where $\mathbf{x} = [u\ v\ w\ p\ q\ r\ \phi\ \theta\ \psi]^{\mathrm{T}}$ is the system states vector. The system states are the velocities and the angular velocities of the aircraft, relatively to the aircraft's center of gravity in its geometrical axes. $\mathbf{u}$ contains the system inputs, so the primary aerodynamic control surfaces deflection with respect to the trim condition. Therefore, the input vector is finally defined as $\mathbf{u} = [\xi\ \ \eta\ \ \zeta]^{\mathrm{T}}$, where the inputs are respectively the ailerons, elevators and rudder deflections. **A** is a matrix that contains the stability derivatives of the aircraft and its moment of inertia, which were reminded in Table 4.24. **B** contains the control derivatives. The aerodynamic and control derivatives are computed following the USAF DATCOM methodology [54], which is based on empirical correlations derived from experiments lead over a panel of various aircraft configuration by the US Air Force (USAF).

It is common to assume that the pitch stability is decoupled from the roll and yaw stability. This way, the dynamic stability is divided into two parts, each having its own set of equations: the longitudinal stability and the lateral stability. Once the stability derivatives are assessed, the eigenvalues of **A** are computed for both longitudinal and lateral stability the the two aircraft configurations for the configuration mid-payload at mid-cruise. They are summarized in Table 5.4 and Table 5.5. Both *MWET-50* and *-76* are dynamically stable; the real part of each eigenvalue is negative. The null eigenvalue present among the lateral eigenvalues for both aircraft depicts the fact that the aircraft have almost no restoring force in the roll direction.

The natural modes of the *MWET* family of aircraft can be analyzed through the eigenvalues of **A**.

Longitudinal	Lateral
-1.021 + 2.167i	0.000 + 0.000i
-1.021 - 2.167i	-3.829 + 0.000i
-0.001 + 0.053i	-0.025 + 0.000i
-0.001 - 0.053i	-0.304 + 1.322i
	-0.304 - 1.322i

Table 5.4: Eigenvalues of **A** of *MWET-50*.

Longitudinal	Lateral
-0.735 + 1.283i	0.000 + 0.000i
-0.735 - 1.283i	-3.719 + 0.000i
-0.002 + 0.051i	-0.112 + 0.000i
-0.002 - 0.051i	-0.236 + 0.585i
	-0.236 - 0.585i

Table 5.5: Eigenvalues of **A** of *MWET-76*.

Longitudinal Modes

An aircraft undergoes two longitudinal modes: the *short-period oscillation* mode and the *phugoid* mode. They are both oscillatory modes and are fully described by a natural frequency (ω [rad/s]) and a damping ratio (ζ [-]). Table 5.6 summarizes those two quantities for *MWET-50* and *-76*. The response of *MWET-50* and *-76* can be compared to requirements for handling qualities from MIL-F-8785C. Those requirements were first destined to US military aircraft, but they can be used for the sake of comparison to civil aircraft [24]. The frequency of the short-period mode is slightly smaller than the MIL-F-8785C, especially for *MWET-76*. That is not an issue given that *MWET* is not designed to specifically satisfy those requirements. The order of magnitude remains acceptable for civil aircraft.

	Short-Period		Phugoid	
	ω_s	ζ_s	ω_p	ζ_p
MWET-50	2.401	1.42	0.058	0.054
MWET-76	1.482	1.066	0.058	0.049
Flying qualities [24]	[2.5; 3.8]	[0.3; 2]	/	≥ 0.04

Table 5.6: Natural frequencies (rad/s) and damping ratio (-) of the longitudinal modes of *MWET-50* and *-76*.

Lateral Modes

From the eigenvalues of the matrix **A**, it can be seen that there is three lateral modes. The *roll subsidence* mode and the *spiral mode* are non oscillatory modes. They are characterised by a time constant:

$$\tau = \frac{1}{|\lambda|}, \tag{5.1.5}$$

which units are in seconds. The third lateral mode is the *Dutch roll*. It is an oscillatory mode is thus defined by a natural frequency (ω_d [rad/s]). The characteristics linked to the lateral mode for *MWET-50* and *-76* are shown in Figure 5.7 and compared to requirements [24]. The flying qualities are respected for all lateral modes.

	Roll Subsidence	Spiral	Dutch Roll
	τ_r	τ_s	ω_d
MWET-50	0.261	40.15	1.35
MWET-76	0.268	8.88	0.631
Flying qualities [24]	<1.4	/	>0.4

Table 5.7: Time constant (s) and natural frequencies (rad/S) of the lateral modes of *MWET-50* and *-76*.

5.2 Aerodynamics

The aerodynamics of the *MWET* family of aircraft were first evaluated based on an analytical approach with empirical correlations during the conceptual design stage. A numerical study is performed in this section in order to validate or update the results which have been determined with the analytical approach, but also perform a deeper analysis. The aerodynamic analysis is carried out using the software FLOW, developed by A.Crovato [55]. FLOW is a finite element solver of the full potential equation for compressible flows. Its accuracy when control surfaces are modeled has never been assessed, so this study is restricted mainly to cruise conditions. In the scope of this analysis, 4 models are built: the isolated wing, the isolated horizontal tail and the combination of the wing and the horizontal tail for *MWET-50* and *MWET-76*.

The first one enables to verify that the wing behaves as expected, in terms of lift generation and lift-to-drag ratio. The second one, together with the wing-horizontal tail models, allows to quantify the downwash effect of the wing on the tail, and to check the incidence angles as well as the overall aerodynamic performances of the aircraft. It is important to note that the lift coefficients of the wing and the tail in cruise have been determined by solving the equilibrium equations of the entire aircraft for the mid-cruise full-payload case, as further detailed in Section 4.1.

Furthermore, a detailed drag study is conducted based on the component build-up method with the equations described by Raymer [18] and Torenbeek [43]. This analysis aims to evaluate the participation of all the drag sources and illustrate this detailed drag evaluation to better understand which sources of drag are the most significant compared to others.

5.2.a Lift Analysis

Wing. The aerodynamics of the wing must be thoroughly verified because it is the largest lifting surface of the aircraft, thus the largest source of induced drag. Therefore, the optimization of the wing lift-to-drag ratio is a key parameter in its design. Figure 5.3 (left) shows the lift coefficient curve in function of the angle of attack in cruise conditions, using empirical correlations and FLOW. It enables to reassess the slope of the 3D lift coefficient as well as the incidence angle of the wing. Moreover, the lift-to-drag resulting from the simulations using FLOW is also compared with the analytical one in Figure 5.3 (right). The value of the profile drag used to plot it is a result from the analytical drag study, which is detailed in the next subsection. Those results are displayed in Table 5.8.

The results are quite close to each other, which suggests that the wing is designed based on accurate estimations. Indeed, it can be observed that both lift coefficient slopes from the analytical and numerical results are close which confirms the validity of *MWET* wing design. Moreover, it confirms that the lift is accurately computed in FLOW. Since it models the physics of the problem better than empirical correlations by solving the full potential equation, and considering that the lift is not much affected by the inviscid nature of FLOW, the numerical solutions can be trusted in terms of lift. Although the lift-to-drag ratio is smaller than expected, due to an underestimation of the induced drag with the empirical correlations, it remains close to the optimum. The design point is thus well defined. Henceforth, it can be concluded that the results obtained with FLOW confirm the relevancy of the conceptual design but also all the choices that have been made in previous sections concerning the wing.

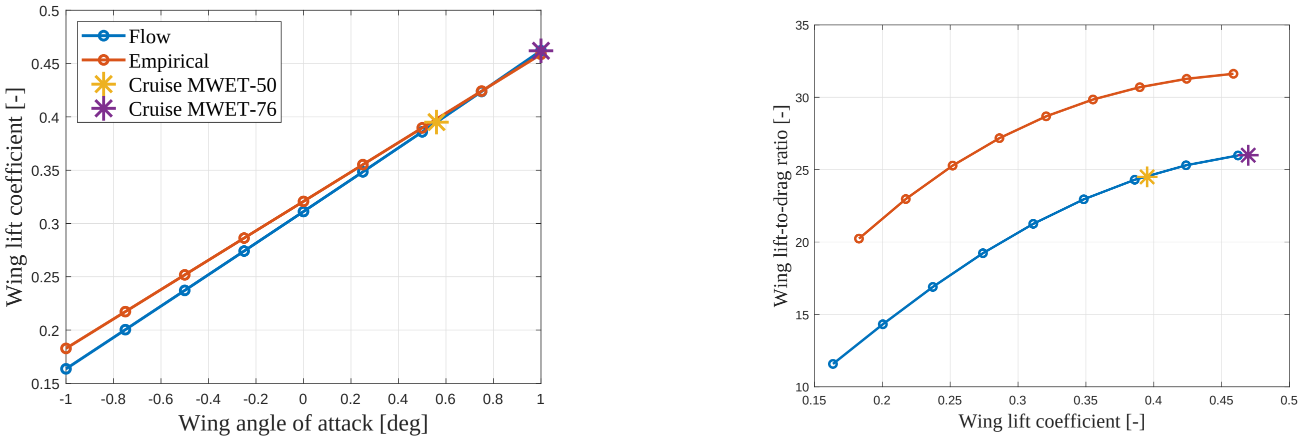

Figure 5.3: Lift coefficient with respect to the angle of attack (left) and lift-to-drag coefficient with respect to the lift coefficient (right) of the wing with both empirical correlations and FLOW.

	MWET-50		*MWET-76*	
	Empirical	**FLOW**	**Empirical**	**FLOW**
Angle of incidence [deg]	0.6	**0.6**	1	**1**
Lift coefficient slope [rad^{-1}]	7.9	**8.6**	7.9	**8.6**
Lift-to-drag ratio [-]	30	**24.5**	30.5	**26**

Table 5.8: Angles of incidence and characteristics of the wings of *MWET-50* and *MWET-76* with empirical correlations and FLOW. The values highlighted in blue are the final ones.

Another parameter that can be verified is the moment coefficient of the wing, as well as the location of the aerodynamic center. To do so, the evolution of the moment coefficient with respect to the angle of attack at the assumed aerodynamic center is reviewed. As can be seen in Figure 5.4, the slope is small so the aerodynamic center computed during the conceptual design phase is a good approximation. Moreover, the moment coefficient remains close to the predicted value from experimental data [20] and thus does not need to be re-evaluated. The values are reminded in Table 5.9.

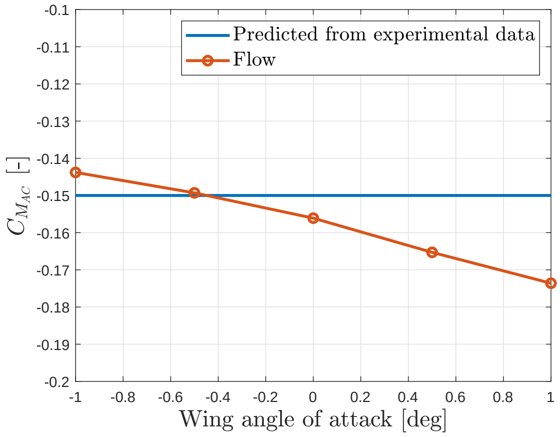

Figure 5.4: Moment coefficient at the aerodynamic centre with respect to the angle of attack based on experimental data and FLOW.

	MWET-50 & -76
$\mathbf{C_{M_{AC}}}$ [-]	-0.15
$\mathbf{y_{AC}}$ [ft]	18.8
$\mathbf{x_{AC}}$ [ft]	2.2
MAC [ft]	6.9

Table 5.9: Characteristics of the wing, as shown in Figure 4.2.

Finally, the spanwise lift distributions of the wing in cruise conditions for both aircraft can be compared with the elliptical one, in order to verify how far or close the lift distribution is from the optimal one. The graphs in Figure 5.5 show that, close to the root, the curves are close to each other, despite a smaller lift at the junction between the wing and the fuselage. Then, due to the linear taper, the distribution diverges from the elliptical one and the lift force finally tends to zero towards the tip, matching with the ideal lift distribution once again.

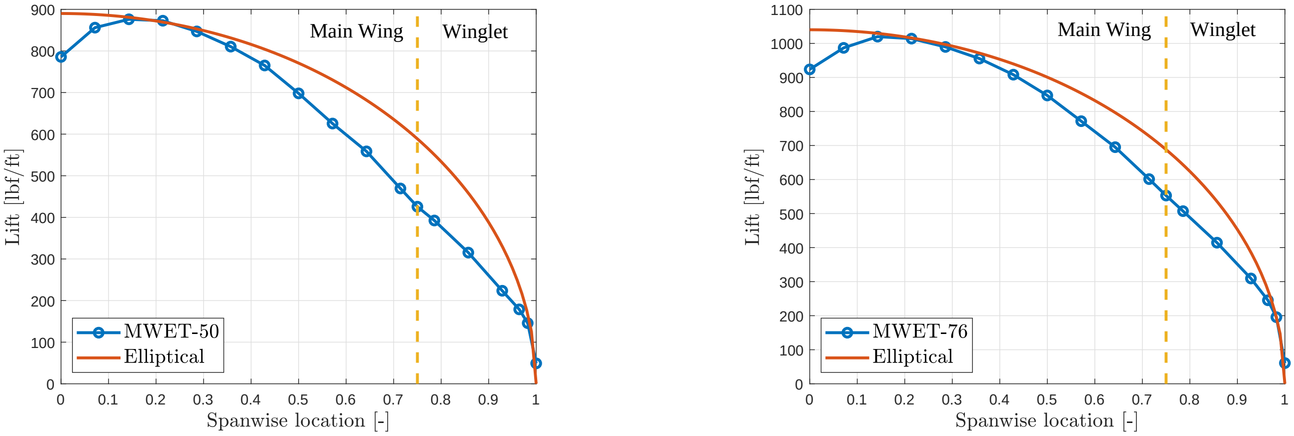

Figure 5.5: Lift distribution along the span of the wing in cruise conditions for *MWET-50* (left) and *MWET-76* (right).

Tail. The wing performs as expected, thus its influence on the horizontal tail and the overall aerodynamic characteristics of the aircraft can be studied. First, the downwash effect is assessed using FLOW, as well as the incidence angle of the horizontal tail so that it generates the lift ensuring longitudinal equilibrium taking into account this downwash. To evaluate this downwash gradient, the lift slope of the tail in the wing-tail model, which corresponds to $C_{L,\alpha_T}\left(1-\frac{d\varepsilon}{d\alpha}\right)$, is simply compared with the slope C_{L,α_T} obtained using the isolated tail model. The downwash angle is evaluated with FLOW by fixing a lift coefficient for the tail, and comparing the corresponding angles of attack in the disturbed flow case (wing-tail model) and the undisturbed flow case (isolated tail model). Since the downwash is caused by the lift, FLOW is trusted for the reasons previously mentioned. Table 5.10 summarizes the results.

	MWET-50		*MWET-76*	
	Analytical	**FLOW**	**Analytical**	**FLOW**
Lift coefficient slope $[rad^{-1}]$	3.38	**4.98**	3.38	**4.98**
Angle of incidence $[deg]$	-1.26	**-0.8**	0.62	**0.2**
Downwash angle ε $[deg]$	1.04	**0.8**	1.17	**0.77**
Downwash gradient $\frac{d\varepsilon}{d\alpha}$ [-]	0.368	**0.16**	0.353	**0.133**

Table 5.10: Angles of incidence and characteristics of the tail of *MWET-50* and *MWET-76* with empirical correlations and FLOW. The values highlighted in blue are the final ones.

The downwash effect over the tail was slightly overestimated with the correlations, such that the incidence angle of the tail in both configurations must be adapted. Based on these results, it can be deduced that the T-tail's geometry is well-designed. Indeed, the choice to use a T-tail to reduce as much as possible the influence of the wing on the flow effectively seen by the tail proves conclusive as the downwash effect remains quite small compared to other types of tail which are placed closer to the wakes of the wing.

Aircraft. The overall lift coefficient is provided by the wing and the tail, and Figure 5.6 shows the contribution of each in cruise conditions with respect to the angle of attack of the aircraft, for both configurations.

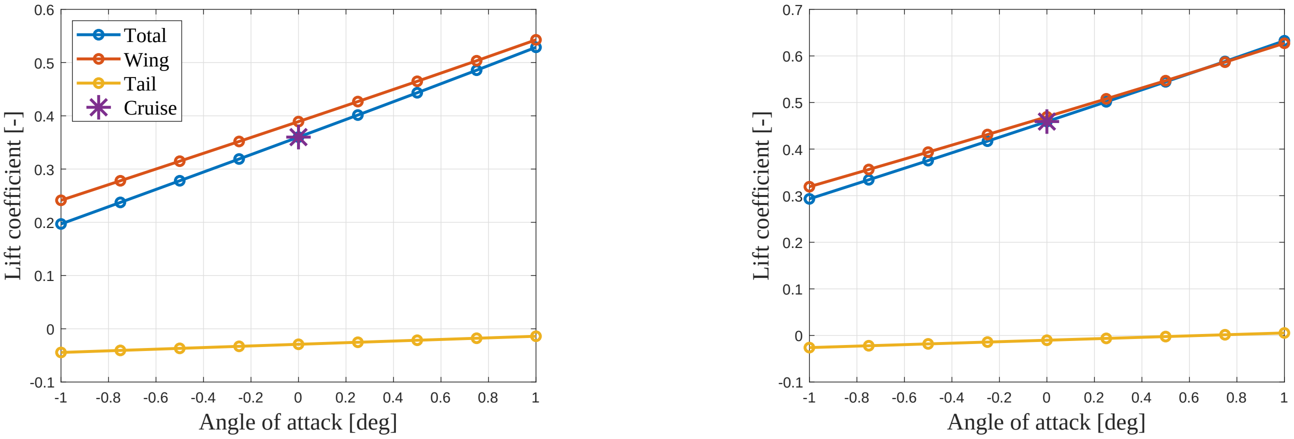

Figure 5.6: Lift coefficient contributions of *MWET-50* (left) and *MWET-76* (right) with respect to the angle of attack with FLOW.

The tail of the aircraft clearly produces negative lift to ensure equilibrium of the aircraft, so that it reduces the total lift coefficient with respect to the one provided by the wing when the fuselage is parallel to the flow. However, it does not account for much of the lift, because the tail's purpose is mainly to stabilize and control the aircraft.

5.2.b Drag Analysis

Analytical

The drag is computed using the component drag build-up method. This method consists first in computing the skin friction coefficient, C_f, of each element. It includes the wing, the fuselage, the two parts of the tail and the engines. These C_f are multiplied by a form factor and an interference factor before being added together to get the zero-lift drag coefficient C_{D_0}. To this, a miscellaneous drag coefficient is added to get the minimum drag coefficient. To obtain the final drag coefficient, the induced drag is added to the sum.

Skin friction coefficient.

The skin friction coefficient is computed by assuming that we have a flow containing part of laminar flow and part of turbulent flow. The equation to compute the skin friction coefficient in these two different parts are presented by Equation (5.2.1).

$$C_{f_{\text{lam}}} = \frac{1.328}{\sqrt{R_e}} \qquad \text{and} \qquad C_{f_{\text{turb}}} = \frac{0.455}{(\log_{10}(R_e))^{2.58}\,(1+0.144M^2)^{0.65}} \tag{5.2.1}$$

In our case all the streamlined body like wing and tail were considered with 10% of laminar flow and the fuselage and engine with 5% [18].

Form factor and interference factor.

These two factors will be different for each component and differ also depending on the book used. The correlations from two different books are used and and compared. The first book used is Torenbeek's book [43] and the second one is Raymer's book [18]. The equations are different but the final result of the drag coefficient will be similar. The result obtained are presented

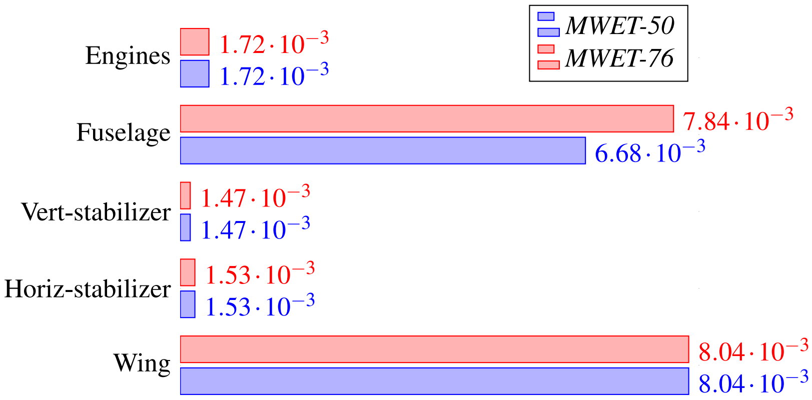

Figure 5.7: Contributions of each component in the zero-lift Drag coefficient [18]

in Table 5.11.

	$FF_{\text{Torenbeek}}$	FF_{Raymer}	$IF_{\text{Torenbeek}}$	IF_{Raymer}
Wing	1.42	1.59	1	1
Horiz. tail	1.19	1.45	2	1.04
Fin	1.21	1.48	2	1.04
Fuselage	1.18	1.15	1	1
Engine	1.25	1.14	1	1.3

Table 5.11: Form and interference factors for the *MWET-50*.

Zero-lift drag coefficient.

The zero-lift drag coefficient is obtained thanks to the Equation (5.2.2) :

$$C_{D_0} = \frac{\Sigma\left(C_f \times FF \times IF \times S_{\text{wet}}\right)}{S_{\text{ref}}} \tag{5.2.2}$$

Each component of the plane will contribute to the C_{D_0} and their contribution is shown in Figure 5.7.

The result obtained for the *MWET-76* do not change except for the fuselage drag but this change is negligible.

Miscellaneous drag.

The miscellaneous drag contains all the drag that is not taken into account by the component drag build-up method. It contains the drag that could come from antenna, pitot tube, sharp corner, inlet or outlet, etc. There is two additional drag to take into account. Firstly, the landing gear does not enter completely inside the fuselage, a fairing is needed. This one will add a drag coefficient equal to 0.00045. Secondly, the case where the landing gear are out of the fuselage also need to be taken into account for the landing and take-off. The values are present in the following Tables 5.14 and 5.15 corresponding to these cases. The leakage drag also needs to be investigated. It is due to the inlet and outlet of the engine. This one is estimated to account for 2% of the parasite drag.

Induced drag coefficient.

The induced drag is the drag generated by the lift created by the wing and tail. It can be computed for different cases. The lift coefficient change depending on whether the design is done full/mid-payload or full/mid-fuel. Different configurations are possible and are presented in Table 5.12.

	MWET-50	*MWET-76*
Mid-payload, mid-fuel	0.0036	0.0050
Full-payload, full fuel	0.0057	0.0085
Full-payload, mid-fuel	0.0051	0.0069
Empty, reserve-fuel	0.0029	0.0040

Table 5.12: Induced drag.

Final drag coefficient.

The total drag coefficient is the sum of all the different components explained earlier and the wave drag. The result for the two reference books and the two aircraft are presented in Table 5.13.

	MWET-50		*MWET-76*	
	Torenbeek	Raymer	Torenbeek	Raymer
C_{D_0}	0.02051	0.019651	0.022061	0.02081
$C_{D_{\text{misc}}}$	0.0009	0.0008	0.0009	0.0009
$C_{D_{\text{wave}}}$	0.0008	0.0008	0.0010	0.0010
C_{D_i}	0.0051	0.0051	0.0069	0.0069
C_D	0.0273	0.0264	0.0309	0.0296

Table 5.13: Final drag coefficient in cruise configuration with full payload and mid-fuel.

It can be observed that there is a difference in the results obtained with the equation coming from the Raymer's book [18] or the Torenbeek's book [43]. This difference can be easily explained by the fact that these two sources do not make the same hypothesis. It has been shown by the polytechnic institute of Virginia [56] that equations coming from the Torenbeek overestimate the drag coefficient, while the equation coming from the Raymer underestimate it compared to results obtained during wind tunnel test. A better approximation could be an average of the two values. Knowing this, the value for the drag coefficient are $C_{D_{MWET\text{-}50}} = 0.0269$ and $C_{D_{MWET\text{-}76}} = 0.0303$.

The total drag coefficient can also be computed for the take-off and landing configurations, where the flaps deflection create an addition to the zero-lift drag such as the landing gear. The induced drag will also change because the lift is higher thanks to flap but also due to the ground effect. Tables 5.14 and 5.15 below show the results.

	MWET-50		*MWET-76*	
	Torenbeek	Raymer	Torenbeek	Raymer
C_{D_0}	0.02051	0.019651	0.022061	0.02081
$C_{D_{\mathrm{LG}}}$	0.0029	0.0029	0.0034	0.0034
$C_{D_{\mathrm{flap}}}$	0.0156	0.0112	0.0112	0.0156
$C_{D_{\mathrm{misc}}}$	0.0008	0.0007	0.0008	0.0007
C_{D_i}	0.1537	0.1560	0.1537	0.1560
C_D	0.1935	0.1904	0.1956	0.1921

Table 5.14: Drag coefficient in Take-off condition.

	MWET-50		*MWET-76*	
	Torenbeek	Raymer	Torenbeek	Raymer
C_{D_0}	0.02051	0.019651	0.022061	0.02081
$C_{D_{\mathrm{LG}}}$	0.0029	0.0029	0.0034	0.0034
$C_{D_{\mathrm{flap}}}$	0.0312	0.0446	0.0312	0.0446
$C_{D_{\mathrm{misc}}}$	0.0011	0.0013	0.0011	0.0014
C_{D_i}	0.1837	0.1968	0.1837	0.1968
C_D	0.2394	0.2653	0.2415	0.2670

Table 5.15: Drag coefficient in Landing condition.

Drag coefficient with one engine out.

When one engine has a failure, an additional drag can be observed. This one is due to the engine-off and from the rudder that is deflected. When one engine fails, the thrust is no longer symmetric, this is why the rudder is deflected to compensate this asymmetry. Moreover, as the engine is off,we can take as a first approximation that there is no more inlet from it and it is seen as a vertical plate. In reality, the engine still have inlet but no more compression. The additional drag coefficient caused by this engine failure is of 0.0375 for the *MWET-50* and 0.0233 for the *MWET-76*.

Comparison with FLOW

In FLOW, only the pressure drag (composed of the induced and the wave drags) is calculated since it solves inviscid flows. The wing produces the majority of this pressure drag, as it is shown in Figure 5.8. This is particularly true for *MWET-76*, since the tail is placed such that it produces less negative lift than for *MWET-50*.

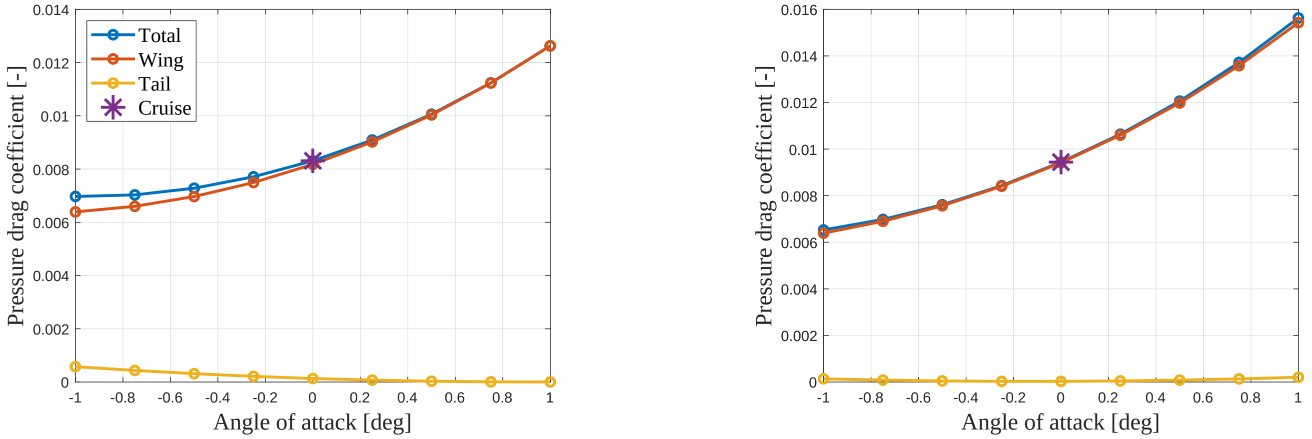

Figure 5.8: Pressure drag coefficient contributions of *MWET-50* (left) and *MWET-76* (right) with respect to the angle of attack with FLOW.

As a result, it is convenient to compare the pressure drag of the wing with the one calculated analytically. Figure 5.9 shows that there is a significant difference between the numerical and the analytical analysis: the pressure drag calculated with FLOW is bigger, resulting in a larger drag of the aircraft. This difference is quantified in Table 5.16, in which the values of the total drag coefficient presented with the subscript FLOW are the sum of the analytical viscous drag and the pressure drag from the simulations.

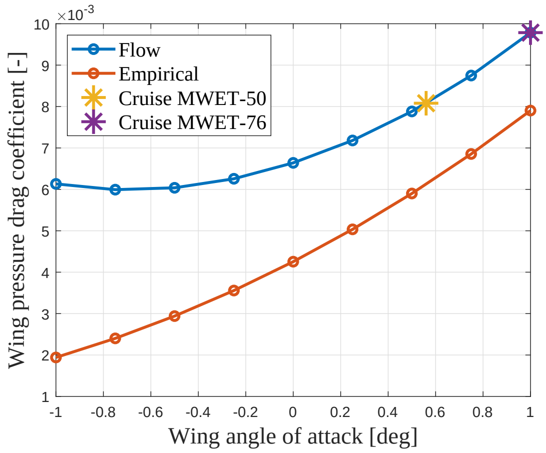

Figure 5.9: Pressure drag coefficient with respect to the angle of attack of the wing with empirical correlations and FLOW.

	MWET-50	*MWET-76*
$C_{D,p,analy.}$ [-]	0.0059	0.0079
$C_{D,p,flow}$ [-]	0.00831	0.00944
Relative error	+41%	+19%
$C_{D,analy.}$ [-]	0.0270	0.0305
$C_{D,flow}$ [-]	0.029415	0.03209
Relative error	+9%	+5%

Table 5.16: Comparison of the pressure drag and total drag coefficients of *MWET-50* and *MWET-76* using empirical correlations and FLOW in cruise conditions.

This difference in pressure drag probably comes from an overestimation of the wave drag in FLOW. Indeed, it does not consider boundary layer calculations, thus the strength of the shock wave on the wing is bigger than in the case of viscous calculations, resulting in a larger wave drag. Given the magnitude of the errors, it is thus safer to trust empirical correlations for the drag, such that the total drag is calculated using the C_{D_0} and $C_{D_{\text{misc}}}$ from Table 5.13 (averaged between the books). The $C_{D_{\text{wave}}}$ as well as the C_{D_i} are also calculated using the empirical correlations from the book, in which the C_L comes from FLOW. The final values of the total drag for both aircraft in cruise conditions:

$$C_{D_{MWET\text{-}50}} = 0.0265 \quad \& \quad C_{D_{MWET\text{-}76}} = 0.0302$$

5.2.c Drag Polar and Lift-to-Drag Ratio

Finally, using the total drag of the aircraft and the lift presented before, the drag polars and the lift-to-drag ratios of *MWET-50* and *MWET-76* can be obtained.

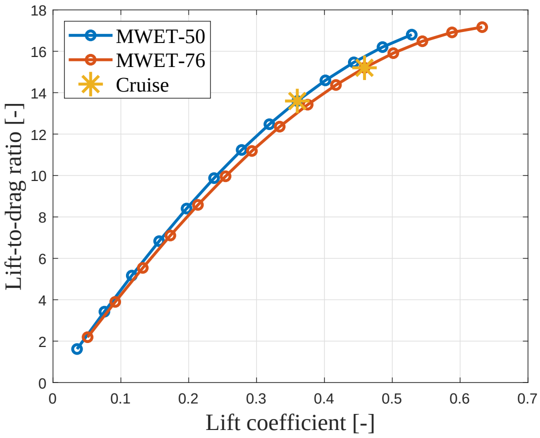

Figure 5.10: Lift-to-drag ratio of both *MWET-50* and *MWET-76* with respect to the lift coefficient.

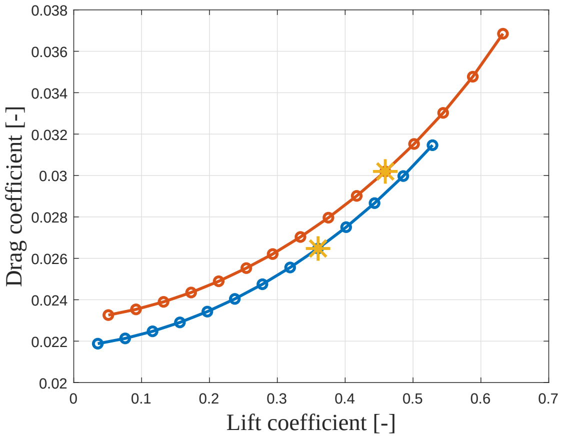

Figure 5.11: Drag polar of both *MWET-50* and *MWET-76* with respect to the lift coefficient.

As expected, the lift-to-drag ratios of both *MWET* aircraft are further from the optimal point than those for the wings (shown in Figure 5.3. Indeed, since the lift is mainly generated by the wing, when considering the whole aircraft the drag increases due to the large amount of drag brought mainly by the fuselage and the engines, while the lift remains nearly the same. Therefore, the lift-to-drag ratio is considerably reduced. However, these types of ratio are quite good if they are compared to those of similar aircraft, and they are quite close from the optimum. In addition, the drags of the *MWET* aircraft family remain in the drag bucket and thus close to the maximal lift-to-drag ratio for a given lift coefficient.

5.3 Structure

One of the main purpose of the aircraft's structure is to withstand the applied loads. These loads come from the weight, thrust, inertial loading and aerodynamic loading, but also from various other sources, such as shocks at landing. In order to characterize the acceptable flight conditions avoiding any harm to the structure and allowing to keep control of the aircraft, two diagrams are presented in this section for each aircraft: the Placard diagram and the flight envelope. Considering the most critical point of the flight envelope, the fuselage loading is then studied to determine the number of stringers and the thickness of the skin for both fuselage and wing. Moreover, the material selection is performed. An analytical analysis and a Finite Element Method analysis are then performed and compared in order verify that the chosen configuration sustains the applied loads.

5.3.a Placard Diagram

This diagram determines the speed at which the airplane should fly depending on the altitude. The Placard diagrams of *MWET-50* and *MWET-76* are represented respectively in Figure 5.12 and 5.13.

The design cruising altitude is located under the stratospheric limit and above the turbulence zone. In this case, it is set to 32,000 ft. The design cruise speed V_C is the speed that the airplane would reach if the engines were operating at 100% of their power. This is not the case in practice, as such a percentage is generally only used for takeoff. This design cruise speed is thus determined based on the maximum thrust of the engines and on the drag. The maximum installed thrust of both engines of *MWET-50* at cruise altitude is 4297 lbf. That of *MWET-76* is 5013 lbf. The drag coefficient is computed as explained in Section 5.2.b, taking into account the fact that the wave drag varies with altitude. Using the expression of the divergence-drag Mach number from [51]:

$$M_{dd} = \frac{\kappa_A}{\cos\,\Lambda_{c/4}} - \frac{1}{\cos^2\,\Lambda_{c/4}}\left(\frac{t}{c}\right) - \frac{C_L}{10\cos^3\,\Lambda_{c/4}} \tag{5.3.1}$$

where $n = 2.5$, $\kappa_A = 0.95$ is the airfoil technology factor, $\left(\frac{t}{c}\right) = 0.14$ the thickness-to-chord ratio, and $\Lambda_{c/4} = 25.84$ the sweep angle at quarter-chord.

- If $M_{\text{cruise}} \leq M_{dd}$:

$$\Delta C_{D,w} = 0.002\left(1 + n\,\frac{M_{dd} - M}{\Delta M}\right)^{-1} \tag{5.3.2}$$

- If $M_{\text{cruise}} > M_{dd}$:

$$\Delta C_{D,w} = 0.002\left(1 + \frac{M - M_{dd}}{\Delta M}\right)^{2.5} \tag{5.3.3}$$

with $\Delta M = 0.05$. The total drag coefficient is then obtained as follows:

$$C_D = C_{D0} + \frac{C_L^2}{e\,\pi\,AR} + \Delta C_{DW} \tag{5.3.4}$$

where AR is the aspect ratio and e the Oswald factor. With $\rho_\infty = 0.027$ lb/ft^3 and $S_{wings} = 581.25$ ft^2, one finds:

$$V_C = \sqrt{\frac{T_{\max}}{\frac{1}{2}\,\rho_\infty\,S_{\text{wings}}\,C_D}} \qquad \text{(true airspeed)} \tag{5.3.5}$$

$$\Rightarrow \qquad V_{C,MWET\text{-}50} = 495 \text{ knots} \qquad \text{and} \qquad V_{C,MWET\text{-}76} = 497 \text{ knots}$$

Above the design altitude, the Mach number has to be kept constant in order to avoid getting close to the sonic condition, which could create shocks due to compressibility effects. Below the design altitude, one wants to keep the drag constant, such that the equivalent velocity is constant, i.e. the true airspeed decreases with decreasing altitude. The equivalent velocity at sea level is equal to:

$$V_{\text{e, sea level}} = \sqrt{\frac{\rho_{\text{cruise}}}{\rho_0}}\,V_C \tag{5.3.6}$$

which is equal to 292 knots for *MWET-50* and to 293 knots for *MWET-76*. The maximum velocity can also be represented in the

Placard diagram. Indeed, the airplane can reach a velocity higher than the design cruise speed during a dive. This corresponds to the design dive speed V_D which is approximated by $1.25 \times V_C$, as suggested by the Federal Aviation Regulation (FAR) [57]. The ceiling is at 47,300 ft for *MWET-50* and 39,500 ft for *MWET-76*, as computed in Section 5.4.

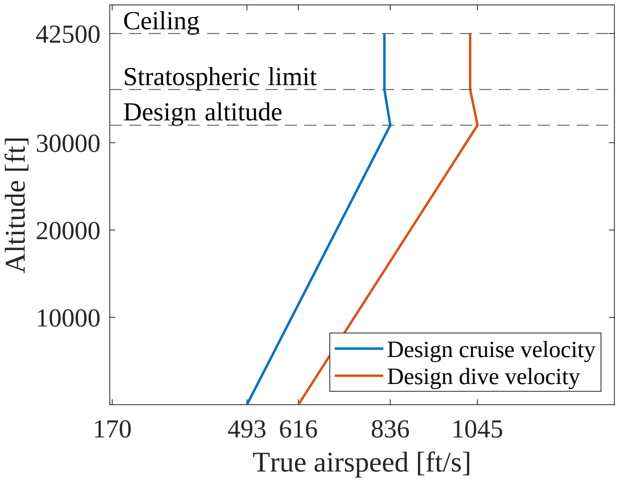

Figure 5.12: Placard diagram for *MWET-50*.

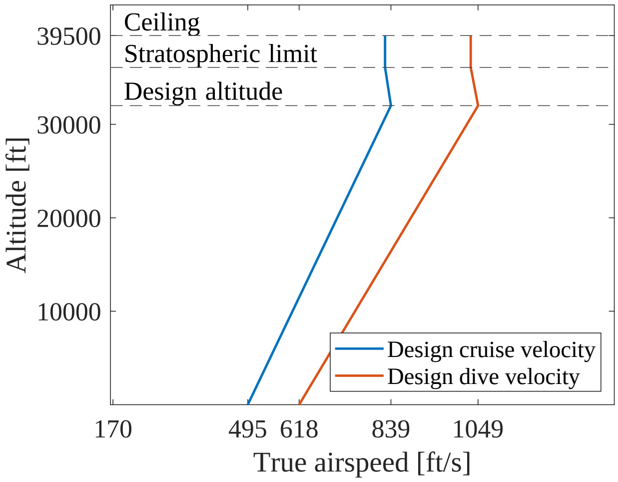

Figure 5.13: Placard diagram for *MWET-76*.

5.3.b Maneuver and Gust Envelopes

The maneuver envelope shows the evolution of the load factor as a function of the airspeed. In particular, it is the equivalent airspeed that is used here, in order to get rid of the dependency on the altitude. These envelopes are represented in Figures 5.14 and 5.15. The corresponding design airspeeds and load factors verify the conditions from paragraphs 25.333 to 25.341 of the Federal Aviation Regulation (FAR) [57].

The maximum and minimum load factors are determined from the FAR. The latter leads to $n_{\max} = 2.5$ and $n_{\min} = -1$. At speeds lower than V_C, the airplane can stall at a load factor smaller than $n_{\max}$. The relation between the load factor and the stall speed depends on the maximum lift configuration $C_{L,\max}$:

$$n = \frac{L}{W} = \frac{\rho_0 V_e^2 S C_{L\max}}{2W} \tag{5.3.7}$$

The stall speed V_{s1} is the speed below which the plane cannot sustain cruise in steady level flight. Idem for V_{s0} except that it corresponds to the case where flaps are down, thus allowing a lower stall speed. The design maneuvering speed V_A is the maximum velocity at which maximum deflection of control surfaces is authorized. Indeed, if it was done at a velocity higher than V_A, the load factor could become higher than the maximum load factor $n_{\max}$, which could damage the airplane.

The gust effect quantifies the increase in load factor due to a sudden vertical gust. The equivalent gust velocity U_e at cruise altitude is ±44 ft/s at an equivalent velocity of the airplane equal to V_B or V_C, and ±22 ft/s at V_D. The gust load factor is expressed as:

$$n_g = 1 + \Delta n \approx 1 + \frac{\rho_0 V_e S F C_{L,\alpha\,\text{plane}} U_e}{2W} \tag{5.3.8}$$

with

$$F = \frac{0.88\mu}{5.3+\mu} \qquad \text{and} \qquad \mu = \frac{2W}{\rho\, C_{L,\alpha\ \text{plane}}\ c\, S} \tag{5.3.9}$$

The gust entering velocity V_B is the minimum speed that the aircraft should have if gust is expected to happen. Indeed, below this velocity, a gust could bring the aircraft much higher than the stall line, and the pilot could lose control of it. V_C has to be high enough compared to V_B in order to have a sufficiently large zone where the aircraft can be flown safely. This is expressed by the following condition: $V_C > V_B + 1.32\,U_e$

The limit load factor is the maximum expected load factor that the aircraft could experience. It is equal to 2.93 for *MWET-50* and 2.56 for *MWET-76*. Although, the aircraft has to be able to withstand an ultimate load factor $n_{\text{ultimate}} = 1.5 \times n_{\text{limit}}$ for three seconds and to be operated until landing.

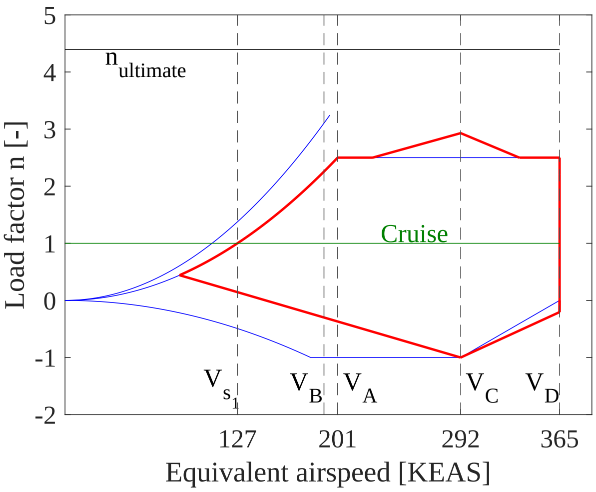

Figure 5.14: Maneuver (blue) and gust (red) envelopes for *MWET-50*.

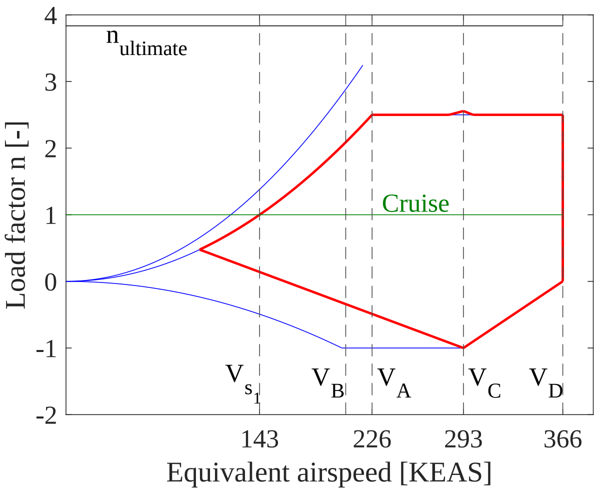

Figure 5.15: Maneuver (blue) and gust (red) envelopes for *MWET-76*.

5.3.c Aerodynamic Loads

For each of the relevant critical points, the aerodynamic loads are computed. These critical points are A($V_{\text{eq}} = V_A$, $n = 2.5$), C(V_C, 2.93), D1(V_D, 2.5) and D2(V_D, -0.20) for *MWET-50*, and A(V_A, 2.5), C(V_C, 2.56), D1(V_D, 2.5) and D2(V_D, -0.20) for *MWET-76*. The computation of the aerodynamic loads is based on an iterative process involving a vertical equilibrium and an equilibrium of moments around the center of mass:

$$I_\theta\, \ddot{\theta} = d_L\, L + d_{\text{th}}\, T + d_{\text{BD}}\, D_B + d_{\text{WD}}\, D_W - d_T\, P + M \tag{5.3.10}$$

$$L = n\, W - T\, \sin(\alpha - \beta) - P\,, \tag{5.3.11}$$

where d_L is the horizontal distance between the aerodynamic center of the wing and the center of mass of the aircraft; d_{WD} is the vertical distance between the two latter points; d_{th} is the distance between the axis of the engines and the axis of the fuselage; d_{BD} is the vertical distance between the center of mass and the body drag center; d_T is the horizontal distance between the center of mass and the aerodynamic center of the horizontal tail.

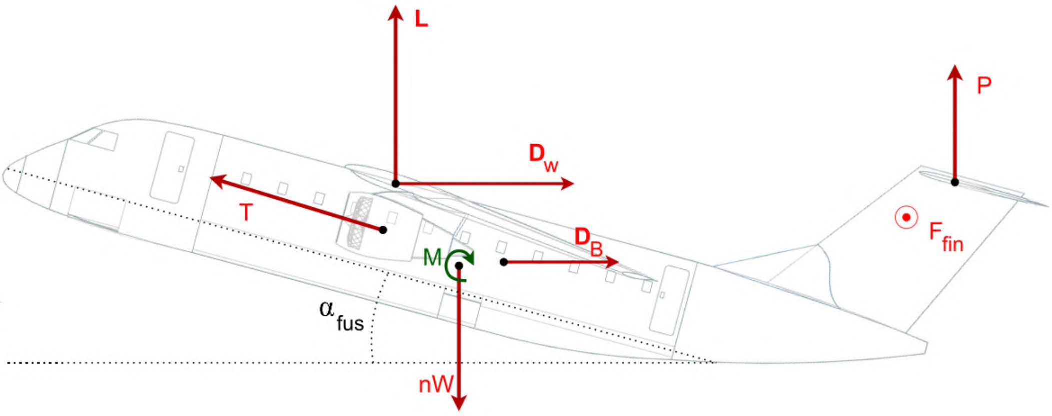

Figure 5.16: Aerodynamic loads.

The expression of the maximum pitch acceleration $\ddot{\theta}$ is given in paragraph 25.331 of the Federal Aviation Regulation [57]:

$$\ddot{\theta} = \frac{39n}{V_{\text{eq}}}(n-1.5) \tag{5.3.12}$$

T is the maximum thrust of the engines, D_B the drag on the fuselage, D_W the drag on the wing and M the pitching moment of the aircraft. The three latter quantities depend on the angle of attack. So at each iteration on α, the only unknowns are L and P, respectively the lift of the wing and the lift of the tail. The lift coefficient can be computed from the lift. From the C_L-α curve, the angle of attack of the next iteration can then be deduced. M_{fus} is the total moment coefficient on the rear fuselage around the longitudinal axis. The latter results only from the fin load, as the tailplane torque due to asymmetric slipstream is ignored. This leads to the results gathered in Table 5.17 and 5.18, where the most critical case is highlighted in blue.

	n	**V_{eq} [KEAS]**	**α [°]**	**P [Lbf]**	**F_{fin} [Lbf]**	**M_{fus} [Lbf ft]**	**L [Lbf]**	**M [Lbf ft]**
A	2.5	201	1.5	-2.4e+04	1.8e+05	5.8e+05	6e+05	-6e+05
C	2.93	292	-0.5	-5.5e+04	3.7e+05	1.2e+06	8e+05	-1e+06
D1	**2.5**	**365**	**-1.5**	**-8.6e+04**	**5.8e+05**	**1.9e+06**	**7e+05**	**-1e+06**
D2	-0.21	365	-2.5	-8.5e+04	5.8e+05	1.9e+06	4e+04	-1e+06

Table 5.17: Aerodynamic loads for the 50-seats configuration.

	n	**V_{eq} [KEAS]**	**α [°]**	**P [Lbf]**	**F_{fin} [Lbf]**	**M_{fus} [Lbf ft]**	**L [Lbf]**	**M [Lbf ft]**
A	2.5	226	0.6	2.3e+03	2.2e+05	7.3e+05	8e+05	-8e+05
C	2.56	293	-0.9	-1.7e+04	3.8e+05	1.2e+06	8e+05	-1e+06
D1	**2.5**	**366**	**-1.9**	**-4.3e+04**	**5.9e+05**	**1.9e+06**	**8e+05**	**-1e+06**
D2	0.027	366	-3.4	-6.9e+04	5.9e+05	1.9e+06	8e+04	-1e+06

Table 5.18: Aerodynamic loads for the 76-seats configuration.

5.3.d Fuselage Section

In this section, the structural loads are first computed. Then a material selection with primarily design are presented. Finally, a numerical analysis is performed to compare it to the analytical results.

First, the shear distribution and the moments that are differentiated from the loads subjected to the fuselage are presented. The computation is presented by assuming that the stringers are only subjected to bending stresses while the skin is subjected to a shear flow that is caused by shear forces and torsion. Starting by a section of interest from the fuselage, the weight distributed and the cross section area are illustrated in Figures 5.17, 5.18 and 5.19.

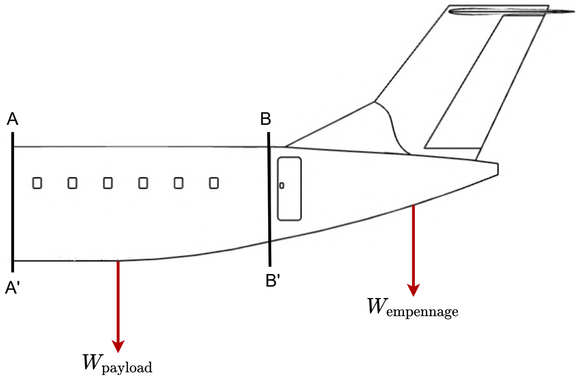

Figure 5.17: Representation of the rear fuselage including the two studied section AA' and BB' and the weights.

W_{payload} is a distributed load including the weight of luggage and $W_{\text{empennage}}$ is a concentrated load. Q_1 and Q_2 are the resultant of load distributions. The fuselage loads are studied at section AA', so just after the position of the wing and at section BB', located just before the empennage as it is illustrated in Figure 5.17. Both sections are assumed to have the same circular dimensions.

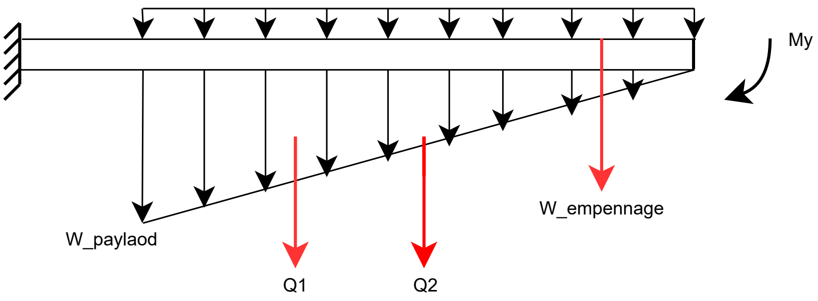

Figure 5.18: Idealization of the rear fuselage with the weights distribution.

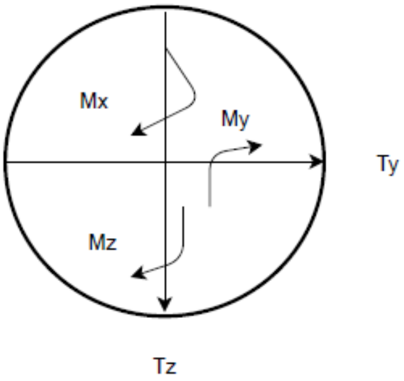

Figure 5.19: Representation of cross-section axis.

Then, the shear forces and the bending moments on the cross-section AA' and BB' can be computed using Equation 5.3.13:

$$\begin{cases} T_y = -F_{\text{fin}} \\ T_z = (SF_{AA'} - P)\cos\left(\alpha_i - i_{\text{wing}}\right) \\ M_x = -M_{\text{fuselage}} \\ M_y = BM_{AA'} - P\ d\ \cos\left(\alpha_i - i_{\text{wing}}\right) \\ M_z = F_{\text{fin}}\ d \end{cases} \tag{5.3.13}$$

where P is the lift force of tail, i_{wing} is the orient angle of the wing, F_{fin} is the fin load, $SF_{AA'}$ is the shear force along z-axis due to the weight distribution, $BM_{AA'}$ bending moment coming from the weight distribution along cross-section, α is the incident angle of attack which depends on the envelope choice, and d the distance between the aerodynamic center of the tail and the cross-section. The effect of the various loads for both types of aircraft are presented in Table 5.19 and 5.20.

MWET-76	**n**	**T_y [lbf]**	**T_z [lbf]**	**M_x [lbf.ft]**	**M_y [lbf.ft]**	**M_z [lbf.ft]**
A	2.5	-5.0e+04	5.9e+04	6.5e+06	2.4e+06	2e+07
C	2.56	-8.5e+04	6.5e+04	1.7e+07	4.3e+06	4e+07
D1	**2.5**	**-1.3e+05**	**6.9e+04**	**1.7e+07**	**6.8e+06**	**6e+07**
D2	0.027	-1.3e+05	1.6e+04	1.7e+07	6.7e+06	6e+07

Table 5.19: Structural loads for different points of flight envelope at section AA'.

MWET-76	**n**	**T_y [lbf]**	**T_z [lbf]**	**M_x [lbf.ft]**	**M_y [lbf.ft]**	**M_z [lbf.ft]**
A	2.5	-5.0e+04	5.6e+04	6.5e+06	1.6e+06	2e+07
C	2.56	-8.5e+04	6.2e+04	1.1e+07	3.5e+06	4e+07
D1	**2.5**	**6.6e+04**	**6.6e+04**	**1.7e+07**	**6.0e+06**	**6e+07**
D2	0.027	-1.3e+05	1.6e+04	1.7e+07	6.7e+06	6e+07

Table 5.20: Structural loads for different points of flight envelope at section BB'.

The most critical loads are observed for *MWET-76* and at section AA'. For this reason, the structural design is developed considering this section.

Material Selection

The aerospace industry has always been a driver for innovation in the material industry. Material selection in aeronautics is a critical task since it influences every part of aircraft, such as the fuel consumption, the operational performance, the safety, the maintenance, the recycling, etc. The material selected for the fuselage, tail and wing *MWET* are based on some constraints listed below

- high yield strength
- low density
- durability
- high fatigue cycle
- resistance to corrosion
- toughness
- damage tolerance
- recyclable material

Composite materials take an important place in the new generation of aircraft. More and more major components are made up of composite because of its competitive properties. One particular standout material is **carbon-fiber reinforced polymer monolithic** (**CFRP**). This material is composed of carbon-fiber embedded in a plastic resin, which gives an higher strength-to-weight ratio than metal and a good resistance to fatigue and corrosion. It is lighter than aluminum, stronger than iron, for a similar resistance. According to Airbus [58], the reduction in weight can go up to 30%, enabling the aircraft to carry more passengers, consume less fuel and fly further. Moreover, CFRP could save the operation of maintenance since the material does not corrode or rust.

Preliminary Design

In this section, the stress distribution and the bending moments of the fuselage due to a non-symmetrical distribution lift load are presented. First, the complex structure model is idealized to a simpler model in order to simplify the computation of the moment of inertia by replacing stringers with booms as it is illustrated in Figures 5.20 and 5.21.

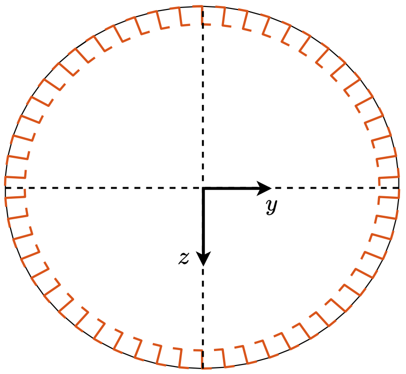

Figure 5.20: Cross section of stringers distribution.

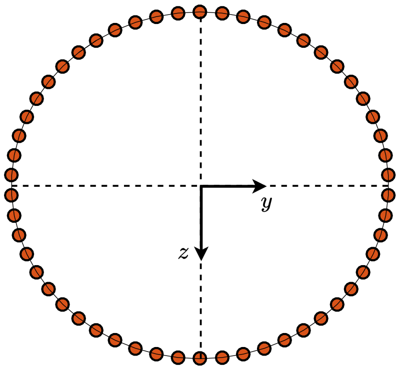

Figure 5.21: Cross section of booms distribution.

Then, from the idealized situation, stringers have a small constant cross-section area compared to the fuselage. Consequently, the assumption was made to have direct stresses on stringers while the skin is sustaining only shear forces. The cross-section of the fuselage has a circular symmetrical shape where a part is subjected to tensile stress and the other part is in compression. Both parts are separated by a neutral axis. The expression of stress can be written as:

$$\sigma_{xx} = \left(\frac{M_z I_{yy} - M_y I_{yz}}{I_{yy} I_{zz} - I_{yz}^2}\right) y - \left(\frac{M_y I_{zz} - M_z I_{yz}}{I_{yy} I_{zz} - I_{yz}^2}\right) z \tag{5.3.14}$$

Due to the symmetrical shape, $I_{yz} = 0$, and the expression becomes

$$\sigma_{xx} = \frac{M_y}{I_{yy}} z - \frac{M_z}{I_{zz}} y \,. \tag{5.3.15}$$

On the other hand, the computation is based on the yield strength and shear strength of CFRP multiplied by the safety factor

$S = 1.5$ to provide the maximum value that stresses are allowed to reach [59].

$$\begin{cases} \sigma_{max} = \frac{\sigma_{yield}}{S} = \frac{76{,}000}{1.5} = 50,000 \text{ [psi]} \\ \tau_{max} = \frac{\tau_{yield}}{S} = \frac{47{,}860}{1.5} = 31,900 \text{ [psi]} \end{cases} \tag{5.3.16}$$

Analytical Analysis

The rear fuselage is composed of frames that give the shape of the structure to prevent the fuselage from buckling. The safe distance between the frames for the composite fuselage structure is 25 inches. The stringers are arranged in equal space with the same cross-section area. The safe distance between the stringers could range between 5.9 to 7 inches [60]. More spacing distance reduces the number of stringers and the total weight of aircraft. By taking into account the used material, a distance of 7 inches is assumed. This corresponds to 52 stringers connected to the fuselage skin panel. The loads undergone by the frames are assumed low and are thus neglected. Therefore, the minimum dimensional area of stringer B is computed using Equation 5.3.17:

$$B_{\min} = \left(\frac{M_y}{I_{yy}} z - \frac{M_z}{I_{zz}} y\right) \frac{1}{\sigma_{\max}} \tag{5.3.17}$$

with the moments of inertia,

$$\begin{cases} I_{yy} = \sum_{i=1}^{N_{\text{stringers}}} z_i^2 \\ I_{zz} = \sum_{i=1}^{N_{\text{stringers}}} y_i^2 \end{cases} \tag{5.3.18}$$

M_y, M_z are the bending moments on the fuselage and y and z are the positions of stringers with respect to the centroid. Then, the minimum stringer area obtained for *MWET-50* and *MWET-76* is $B_{\min} = 0.093 \text{ in}^2$.

The skin must resist the shear flow which is the summation of the maximum shear flow due to T_y, T_z and the shear due to the torque which is constant along the section. The maximum shear flow can be expressed as

$$q^{i+1} = q^i - \frac{T_y}{3D^2} y_i - \frac{T_z}{3D^2} z_i + \frac{M_x}{2(\pi D^2/4)} \tag{5.3.19}$$

By taking the maximum shear load in each envelope, the value is substitued in Equation 5.3.19 to get the maximum shear flow in the skin. Therefore, the thickness of skin can be obtained by the formula:

$$t > \frac{q_{\max}}{\tau_{\max}} \tag{5.3.20}$$

Considering the thickness is uniform, the value $t = 0.14$ inches is obtained for both aircraft.

Due to the use of composite, rivets cannot be used as assembly method. Bonding is thus preferred as it is common for joining composite structure.

Summary of the dimensions of the structural design of the fuselage:

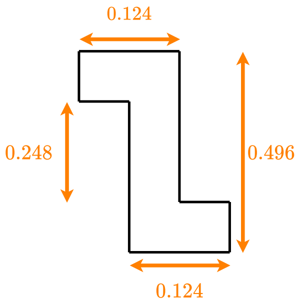

Figure 5.22: Fuselage stringer geometry [in] .

Component	Thickness or Area	Quantity
Stringers	0.093 in^2	52
Skin	0.13 in	/
Frame	0.13 in	/

Table 5.21: Summary of the dimensions of fuselage's components.

5.3.e Wing Section

In this section, the same methodology as the one performed for the fuselage is applied to the wing. However, the cross-section is not symmetrical anymore. First, the reaction forces and the moments are evaluated at the wing root section, which is the critical zone since it leads to the largest stresses. The primary study is based on the idealization of stringers to booms to simplify the computation. Finally, a finite element analysis is performed with SIEMENS NX 12 software to compare the results.

The loads applied to the wing can be shown in Figure 5.23 where L and D_w are the aerodynamic force decomposed in lift and drag at the aerodynamic center, W is the self weight of the wing applied at the center of gravity including the weight of the installed engine and M is the moment applied around the aerodynamic center. The study is based on a half-span wing, only half of the loads are imposed.

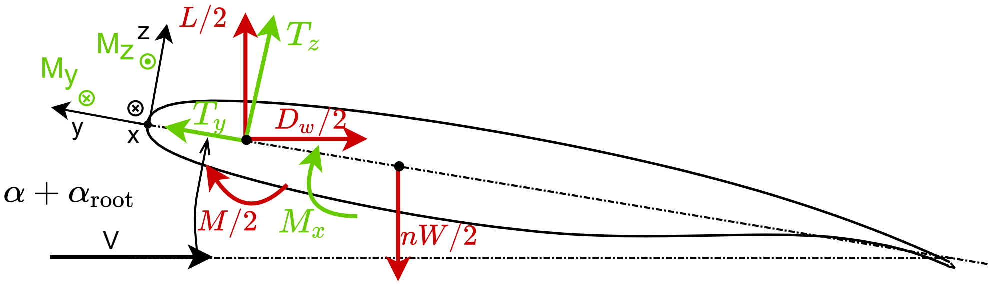

Figure 5.23: Forces and moments acting on the airfoil in the section at the root.

The equilibrium equations on the airfoil at the root section are shown in Equation 5.3.21:

$$\begin{cases} T_y = \left(\frac{L}{2} - \frac{nW}{2}\right)\sin\left(\alpha + \alpha_{\text{root}}\right) - \frac{D_w}{2}\cos\left(\alpha + \alpha_{\text{root}}\right) \\ T_z = \left(\frac{L}{2} - \frac{nW}{2}\right)\cos\left(\alpha + \alpha_{\text{root}}\right) + \frac{D_w}{2}\sin\left(\alpha + \alpha_{\text{root}}\right) \\ M_x = M/2 \\ M_y = \left[\frac{D_w}{2}\sin\left(\alpha + \alpha_{\text{root}}\right) + \frac{L}{2}\cos\left(\alpha + \alpha_{\text{root}}\right)\right] y_{AC} + \frac{nW}{2}\cos\left(\alpha + \alpha_{\text{root}}\right) y_{CG} \\ M_z = \left[\frac{D_w}{2}\cos\left(\alpha + \alpha_{\text{root}}\right) + \frac{L}{2}\sin\left(\alpha + \alpha_{\text{root}}\right)\right] y_{AC} + \frac{nW}{2}\sin\left(\alpha + \alpha_{\text{root}}\right) y_{CG} \end{cases} \tag{5.3.21}$$

Their values at the different points of the flight enveloppe defined in Section 5.3.c are represented in Table 5.22 for *MWET-76* only as they are more critical.

MWET-76	n	T_y [lbf]	T_z [lbf]	M_x [lbf.ft]	M_y [lbf.ft]	M_z [lbf.ft]
A	2.5	5.7e+04	4.0e+04	3.2e+06	1.8e+06	7e+05
C	2.56	-3.8e+04	6.3e+04	5.5e+06	-2.1e+06	3e+06
D1	**2.5**	**-7.5e+04**	**1.6e+03**	**8.5e+06**	**-2.9e+06**	**1e+06**
D2	0.027	1.7e+03	-9.5e+03	8.5e+06	5.9e+04	-3e+05

Table 5.22: Structural loads for different points of flight envelope at wing root section for *MWET-76*.

Analytical Study

As in the fuselage, the material used for the wing's structure is **carbon-fiber reinforced plastic**. The values of yield strength σ_{yield} and shear strength τ_{yield} are the one expressed in Equation 5.3.16. The following assumptions have been made:

- Due to the fact that wings are identical for both *MWET-50* and *MWET-76*, the study can be simplified. As aerodynamic and structural loads are more critical for the 76 seats configurations, the structural design is only performed for the latter.
- A bending moment induces only direct stress carried by the booms only.
- Torque and shearing loads cause only shear stress carried by the skin.
- The position of the centroid is computed by Equation 5.3.22 with y_i, z_i the position of the booms from the leading edge.

$$y_c = \frac{\sum_i^{N_{\text{booms}}} A_i y_i}{\sum_i^{N_{\text{booms}}} A_i} \qquad z_c = \frac{\sum_i^{N_{\text{booms}}} A_i z_i}{\sum_i^{N_{\text{booms}}} A_i} \tag{5.3.22}$$

First, the idealized wing section is illustrated in Figure 5.24. This one is split into three cells divided by two spars to allow good resistance against the loads. The first spar is located at the aerodynamic center and the second one at the aileron junction. The third cell is assumed to sustain no shear flow. Actually, it is composed of control surfaces that are not designed to sustain loads. Finally, the spacing distance between the stringers is 3.9 inches resulting in a number of 43 booms.

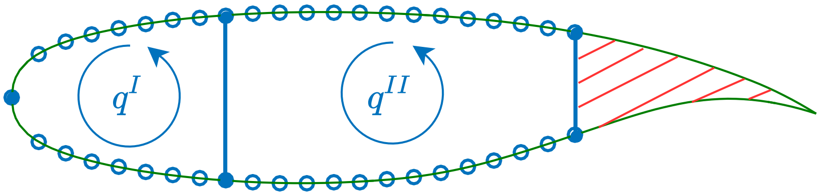

Figure 5.24: Representation of the idealized airfoil where the green line is the skin, the two vertical lines are the spars and the dots represent the stringers.

Direct stress From the bending moments M_y and M_z, the direct stresses are computed in Equation 5.3.23 in order to determine the area of the booms B with y and z the position from the centroid.

$$\sigma_{xx} = (1/B)[(\frac{M_z I_{yy} - M_y I_{yz}}{I_{yy} I_{zz} - I_{yz}^2})y - (\frac{M_y I_{zz} - M_z I_{yz}}{I_{yy} I_{zz} - I_{yz}^2})z] \tag{5.3.23}$$

Because the section of the wing is not symmetrical the non-diagonal moment of inertia are not equal to 0. The Equation can be seen below.

$$\begin{cases} I_{yy} = \sum_i^{N_{\text{booms}}} z_i^2 \\ I_{zz} = \sum_i^{N_{\text{booms}}} y_i^2 \\ I_{yz} = \sum_i^{N_{\text{booms}}} (y_i . z_i) = I_{zy} \end{cases} \tag{5.3.24}$$

From the maximum yield strength of CFRP, the area of the booms can be computed thanks to Equation 5.3.25.

$$\sigma_{max} \geq B\sigma_{xx} \tag{5.3.25}$$

It results that the area for the booms is fixed to 0.31inches^2.

Shear stresses By considering the torque M_x and the shear loads T_y and T_z, the thickness of the skin can be determined as it is assumed to carry shear stresses only.

The wing section can be considered as a closed thin-walled section for which the shear flow is computed by cutting each cell close to the spar. Noting that the equations are taking into account the taper of the wing.

$$q_o(s) = -\frac{I_{zz} T_z^{\text{web}} - I_{yz} T_y^{\text{web}}}{I_{yy} I_{zz} - I_{yz}^2} \left[\int_0^s t_{\text{direct}\,\sigma} z ds + \sum_{i:s_i \leq s} z_i A_i \right] - \frac{I_{yy} T_y^{\text{web}} - I_{yz} T_z^{\text{web}}}{I_{yy} I_{zz} - I_{yz}^2} \left[\int_0^s t_{\text{direct}\,\sigma} z ds + \sum_{i:s_i \leq s} z_i A_i \right] \tag{5.3.26}$$

where $t_{\text{direct}\,\sigma} z = 0$ as the skin is assumed to carry shear stress only. The change of shear flow induced by a boom is expressed in Equation 5.3.27.

$$q^{i+1} - q^i = -\frac{I_{zz} T_z^{\text{web}} - I_{yz} T_y^{\text{web}}}{I_{yy} I_{zz} - I_{yz}^2} B_r z_r - \frac{I_{yy} T_y^{\text{web}} - I_{yz} T_z^{\text{web}}}{I_{yy} I_{zz} - I_{yz}^2} B_r y_r \tag{5.3.27}$$

where

$$\begin{cases} T_z^{web} = T_z - \sum_{i=1}^{N_{\text{booms}}} P_z^i = T_z - \sum_{i=1}^{N_{\text{booms}}} P_x^i \frac{\delta z^i}{\delta x^i} = T_z - \sum_{i=1}^{N_{\text{booms}}} \sigma_{xx} B \frac{\delta z^i}{\delta x^i} \\ T_y^{web} = T_y - \sum_{i=1}^{N_{\text{booms}}} P_y^i = T_y - \sum_{i=1}^{N_{\text{booms}}} P_x^i \frac{\delta y^i}{\delta x^i} = T_z - \sum_{i=1}^{N_{\text{booms}}} \sigma_{xx} B \frac{\delta y^i}{\delta x^i} \end{cases} \tag{5.3.28}$$

Then a corrected shear flow is added and obtained from the momentum balance and the twist rate compatibility in Equation 5.3.29

and 5.3.30 respectively.

$$y_T T_z - z_T T_y \pm M_x = \sum_c \int_{\text{cell}\,c} q_o\, p\, ds + \sum_{\text{cell}\,c} 2A_h^c q^c(0) + \sum_{\text{boom}\,j} y^j \mathbf{P}_z^j - \sum_{\text{boom}\,j} z^j \mathbf{P}_y^j \tag{5.3.29}$$

$$\theta_{,x} = \frac{1}{2A_h^i\, \mu_{\text{REF}}} \left[-q^{i-1}(0)\bar{l}_{i-1}^i + q^i(0)\bar{l}^i + \oint_{\text{cell}\,i} \frac{q_o}{t\frac{\mu}{\mu_{\text{REF}}}} ds - q^{i+1}(0)\bar{l}_i^{i+1} \right] \tag{5.3.30}$$

where $\mu_{\mathbf{ref}}$ = 840 ksi is the shear modulus of **CFRP** and $\overline{l^i}$ is a non-dimensional length defined as:

$$\bar{l}^{i\,i+1} = \int_i^{i+1} \frac{ds}{t\frac{\mu}{\mu_{\mathbf{ref}}}} \tag{5.3.31}$$

Finally, the total shear stress is obtained thanks to Equation 5.3.32

$$q = q_o + q(0) \tag{5.3.32}$$

Then, the thickness can be obtained from the relation between the total shear fluxes and the shear strength of CFRP in Equation 5.3.33.

$$t = q_{\max} / \tau_{\max} \tag{5.3.33}$$

From this analytical study, a thickness of 0.118 inches has been chosen by simplicity for the skin, the spars and the ribs.

Assembly method About the assembly method, the use of composite induces that rivets can not be used to assemble the stringers and the skin. Instead, bonding is preferred. The latter is a common method for joining composite structures. It is designed to be a permanent joining method, like welding metal.

Dimensions summary This sums up the results obtained in the structural design of the wing of the aircraft.

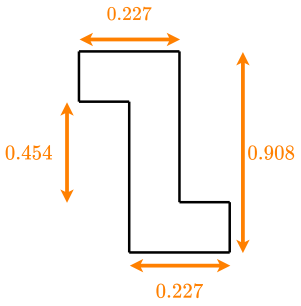

Figure 5.25: Wing stringer geometry [in].

Component	Thickness or Area	Quantity
Skin	0.118 in	/
Stringers	0.31 in^2	43
Spars	0.118 in	2
Ribs	0.118 in	26

Table 5.23: Summary of the wing structure components.

5.3.f Finite Element Analysis

Most analytical results are supported by a numerical analysis. For that reason, a finite element model has been implemented in order to compare the results obtained from the study of the fuselage and the wing.

Fuselage

The model representing the fuselage in Figure 5.26 is composed of frames equally spaced covered by the skin. Then stringers are added to reinforce the structure. The latter are composed of 1D elements of type *CBEAM* with a Z cross-section of area 0.093 in^2. The frames and the skin are discretized by quadrangular 2D elements of type *CQUAD4* for which thicknesses are 0.13 in for both of them. Noting that assembly constraints such as the windows, intersection between parts for example are not taken into account.

Figure 5.26: Representation of the CAD model and the mesh of the fuselage

In order to simplify the numerical simulations, the fuselage is studied between section AA' and BB' from Figure 5.17. It is assumed to be clamped on the side just after the wing. On the other extremity, the forces and moments resulting from the empennage have to be taken into account. Therefore, they are composed of the lift on the tail, the force on the fin and the weight of the empennage. They are modeled as three moments applied to the last frame at section BB' and a force to take into account shear loads. Moreover, the studied section is subjected to the total weight of the payload including luggage, passengers. It has been divided into components applied to each frames in order to represent a load distribution.

The resulting stresses are represented in Figure 5.27 and 5.28 for the direct and shear stresses respectively.

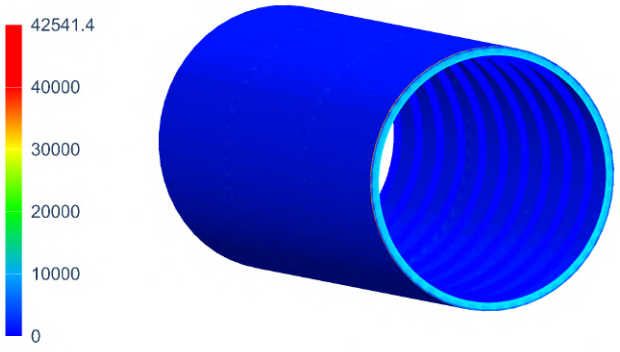

Figure 5.27: Maximum direct stresses [lb/in^2].

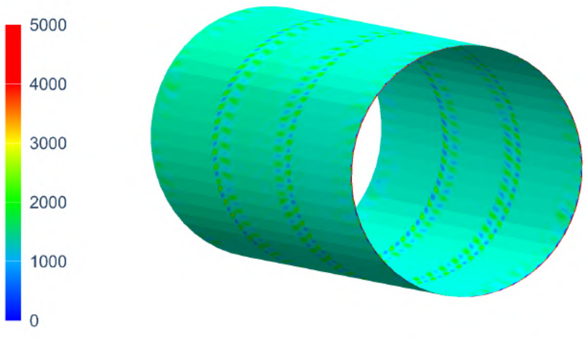

Figure 5.28: Maximum shear stresses [lb/in^2].

From this analysis, the stresses evaluated in this section are compared to the one obtained analytically. In the analytical part, it has been observed that the most critical section was located at AA' whereas stresses are concentrated in section BB' numerically. It mainly comes from the fact that the fuselage is assumed to be clamped on one side.

An other observation is that the maximum stress is concentrated on the section where the loads from the empennage are applied. For this reason, this frame will especially have to be reinforced at the junction between the fuselage and the empennage.

Finally, the results are compared to the one obtained through the analytical analysis and are represented in Table 5.24. Results are of the same order for both direct and shear stresses. Nonetheless, Figure 5.28 shows that the skin sustains also part of the direct stresses unlike the assumption made in the analytical study.

	Analytical	**FEM**
Max. direct stress [psi]	47,892	44,028
Max. shear stress [psi]	10,877	14,611

Table 5.24: Comparison of the maximum stress between analytical and numerical analysis for the *MWET-50* fuselage.

To further improve the simulations, the effect of the windows or the exact distribution of the payload could be considered.

Wing

To perform the finite element analysis, half of the wing is considered due to its symmetry with respect to the fuselage center. It permits faster computation. The internal structure of the wing is represented in Figure 5.29 and its characteristics are gathered in the table 5.23. The wing is fixed at its root and it is assumed that the control surfaces are not considered as load carrier so do not contribute to the wing stiffness.

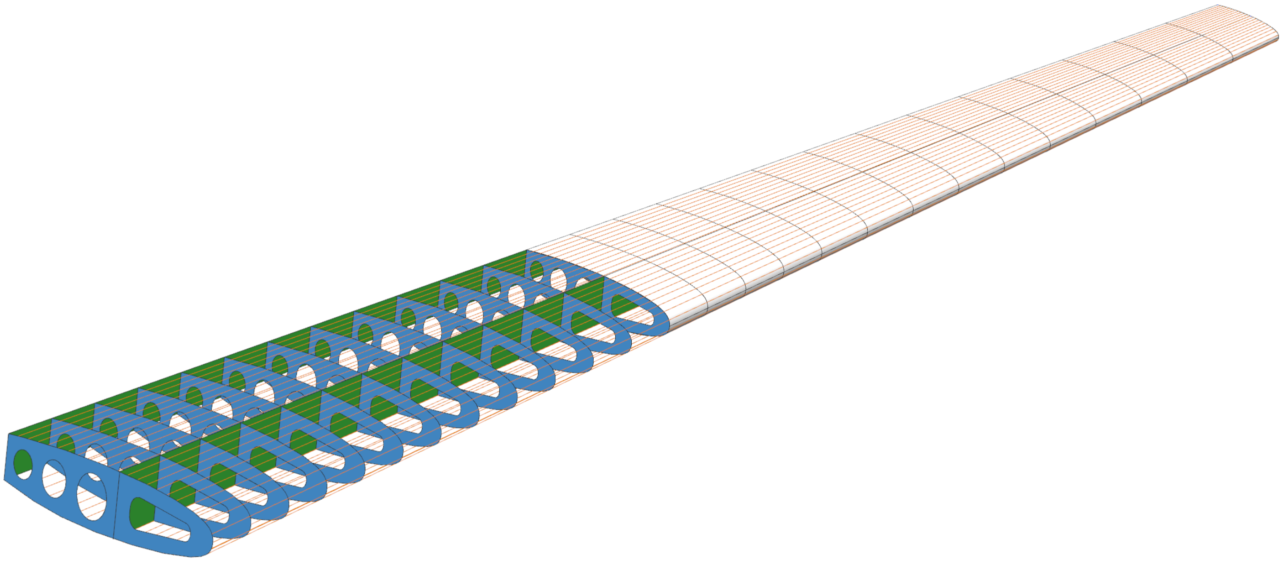

Figure 5.29: Internal structure of the *MWET* family wing. The ribs are in blue, the spars in green, the skin in white and the stringers in orange.

The worst-case flight condition for the wing is the point D1 (see Table 5.18) for the *MWET-76* aircraft. As the wing is the same for both aircraft, only this case is taken into account in the structure simulation. The lift distribution has been imposed but also, the self-weight of the wing, the engine mass and the thrust have to be taken into account. The fuel tank is considered as empty, which leads to higher loads and a more critical condition. It gives the loaded wing in Figure 5.30. The results are split into direct and shear stresses.

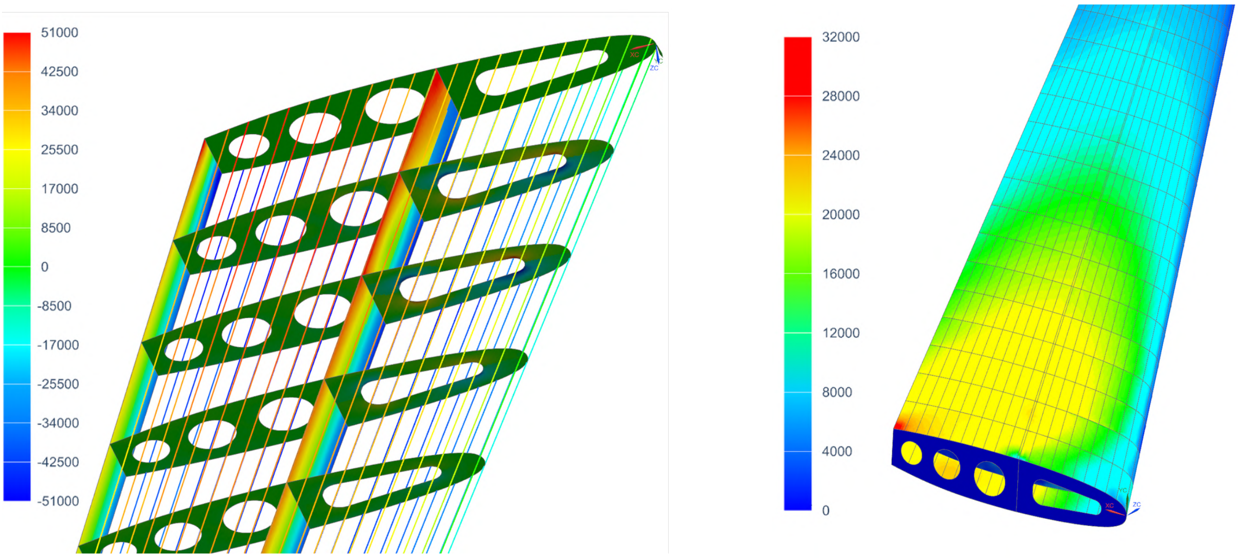

Figure 5.30: Maximal direct stress (left) [lbf/in^2] and maximal shear stress (right) [lbf/in^2] on the *MWET-76* worst-case.

As expected analytically, it can be seen that the stress distribution decreases along the spanwise direction and the results obtained seem plausible. As it could be predicted, the direct stress is highly compensated by the stringers while the skin and the spars sustain the majority of the shear stress. However similarly to the fuselage, a fraction of the shear stress is sustained by the stringers whilst the skin and spars sustain the direct stress. The maximal and minimal values are higher than the one given in Table 5.25 because of some singularities at the corner of the rib and the spars. However, the maximal and minimal values displayed with the legend are the limitation of the material with a security factor of 1.5. It can be seen that near the root of the half-wing, the direct stress is higher so the wing must be reinforced at the root and at the wing fixation.

	Analytical	**FEM**
Max. direct stress [psi]	36,072	36,260
Max. shear stress [psi]	31,900	32,630

Table 5.25: Comparison of the maximum stress between analytical and numerical analysis for the *MWET-76* half-wing.

Table 5.25 shows the difference of maximum stress obtained analytically and numerically. For both, the finite element model gives a bit higher stress than in the analytical method. The difference can be due to analytical assumptions but also from load concentration in the finite element model. Also, it can be noticed that the values obtained with the finite element model gives maximal values which are higher than the security stresses given above but are below the yield stress of the material.

Lastly, the displacement of the wing induced by the critical loading is shown in Figure 5.31. The displacement obviously increases along the span wise direction and reach its maximum at the wing tip. At this position, the amplitude is quite high but because of its material, the wing is really flexible. It can be compared to the Boeing 787 Dreamliner (at its span ratio) which is also made of carbon-fiber reinforced polymer [61].

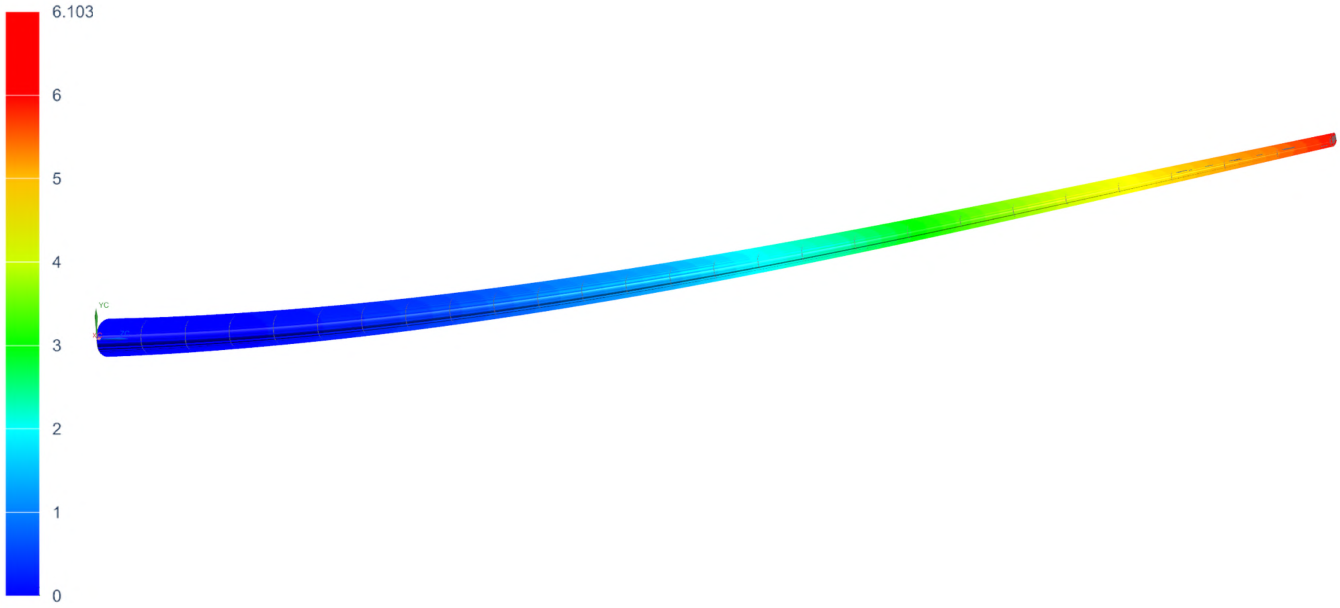

Figure 5.31: Wing displacement [ft] in the case D1 of the *MWET-76*.

An optimization and an improvement of the wing structure can be made by reinforcing the root which is a critical zone by adding stronger stringers and a thicker skin to reduce shear and direct stress to fit in the security range. Also, it can be recalled that the flexible winglets wasn't modeled in the finite element model but this mechanism is used to reduce the direct stress at the root of the wing as explained in the section 4.1. Then an advanced modelization can be performed to study this case. Finally, it can be seen that there is no strong stress starting from the middle of the wing. Therefore, a decrease of the skin and rib thickness should be conceivable to reduce the mass, the fuel consumption and the flying cost.

5.4 Performance

5.4.a Takeoff

The request for proposal requires a maximum takeoff field length of 4000 ft and 6000 ft for the 50- and 76-passengers regional aircraft respectively, with an obstacle clearance of 50 ft to a runway with dry pavement (sea level ISA + 18°F day) for both configuration. This upper bound of takeoff field length must be respected even if during the takeoff phase the aircraft is subjected to one engine failure beyond the decision speed. The methodology that has been followed is fully described in [18] and [25].

During the ground roll, the horizontal forces which act on the aircraft are the thrust produced by the engines, the drag and the friction force due to the contact of the wheels with the pavement. Assuming a flat and dry pavement made of concrete and asphalt leads to a friction coefficient $\mu = 0.03$ (-) as mentioned in [4] and in [18]. In order to respect the FAR part 25 requirements for the takeoff phase of a commercial airliner, the liftoff velocity (minimum threshold speed at which the pilot can attempt a liftoff maneuver) will be assumed equal to $V_{\mathrm{TO}} = 1.1 \cdot V_{\mathrm{stall}}$ while the climb velocity (minimum required speed to clear the obstacle with the climb angle) is equal $V_{\mathrm{CL}} = 1.2 \cdot V_{\mathrm{stall}}$. The ground roll distance, expressed by the Eq. 5.4.1, results in the required distance to achieve the acceleration from the null to the liftoff velocity. During this phase, the drag experienced by the aircraft depends mainly on the deflected flaps and the deployed landing gear.

$$X_{\mathrm{G}} = \int_{V_i}^{V_f} \frac{V}{\frac{g}{W}(T - D - \mu(W - L))} dV \tag{5.4.1}$$

However, in case of an engine failure occurring during takeoff, the rudder will be deflected to compensate the yawing moment produced by the asymmetry of the thrust. The rudder deflection and the inoperative engine will both lead to an increase of the drag. An analytical expression to estimate this increment of drag is developed in [4]. The drag forces encountered during the takeoff phase are computed and shown in the section 5.2.b. If the failure is encountered before the decision speed V_1, by definition of this threshold, the braking devices are applied and the takeoff is aborted. In the opposite case, as the aircraft needs enough velocity to attempt a climb in order to clear the mandatory obstacle of 50 ft, an increment of ground roll distance, X'_{G}, will be added to reach V_{CL} starting from V_{TO}. The decision speed for both *MWET* seats configuration is evaluated at $1.07 \cdot V_{\mathrm{stall}}$ using the equation 5.4.1 with $\mu = 0.4$ (-) (ground friction and the activation of the braking devices) and $V_f = 0$. The decision speed is determined by defining the balanced field length as the total needed length of the runway with one engine inoperative.

Then, rotation leading to liftoff is initiated and is assumed to take place within 2 seconds. This maneuver is effectuated at V_{TO} for an all operative engine takeoff and at V_{CL} after the increment of ground roll for one engine inoperative takeoff.

The transition phase (denoted TR) consists of the acceleration from V_{TO} to V_{CL} during a circular arc path whose radius, R, is function of the mean velocity and the load factor. The covered horizontal and vertical distances (X_{TR} and h_{TR}) during this maneuver are,

$$X_{\mathrm{TR}} = R \sin\gamma \quad \text{and} \quad h_{\mathrm{TR}} = R(1 - \cos\gamma) \tag{5.4.2}$$

where the climb angle can be computed as, knowing the drag D_{to} acting on the aircraft and the available thrust produced by the engines T_{to},

$$\gamma = \arcsin\left(\frac{T_{\mathrm{to}} - D_{\mathrm{to}}}{W_{\mathrm{to}}}\right) \tag{5.4.3}$$

Finally, the takeoff field part required to clear the obstacle of 50 ft at the end of the runway can be computed as,

$$X_{\mathrm{CL}} = \frac{h_{\mathrm{obstacle}} - h_{\mathrm{TR}}}{\tan\gamma} \tag{5.4.4}$$

.

The takeoff phase continues with a climb which keeps the velocity and the angle at the end of the transition phase until an altitude of 1500 ft.

Considering double slotted-flaps deflected at 20°, which produce a maximum lift coefficient of 2.17 [-] as mentioned in Table 4.7, and the stall velocity at takeoff which results from the application of these high lift devices, the takeoff distances for both *MWET* configurations can be computed. Each segment of the takeoff phase at sea level is shown in the figure 5.32 and the total distances are synthesized in Table 5.26. The AIAA also requires to show the respect of the performance requirements at takeoff for an altitude of 5000 ft above sea level (ISA + 18°F). These performances are shown in the Table 5.26.

Note that the climb angles for a normal takeoff are computed equal to 15° and 13° respectively for the *MWET-50* and the *MWET-76*. As mentioned in [18] and [25], a typical climb angle at takeoff for an airliner is included between 10° and 15°. However, in an event of one engine failure, these climb angles will be reduced to 5° and 4.8° due to the increase of the drag and the loss of power. These values respect the minimum climb gradient of 2.4% (= 1.38°) imposed for 2-engines airliner by the FAR25.

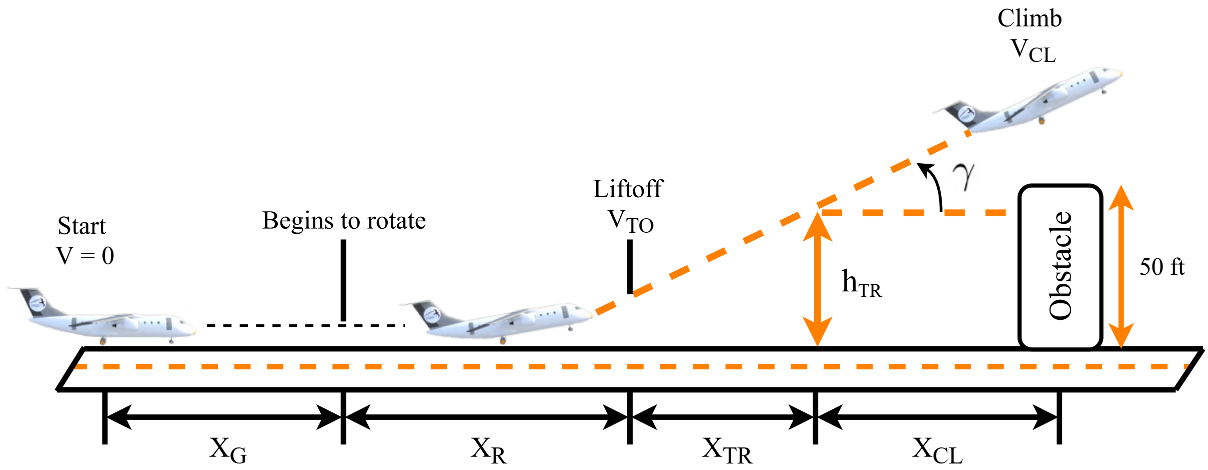

Figure 5.32: Takeoff phase.

	Ground distance ($X_G + X'_G + X_R$)[ft]	**Air distance** (X_{TR} + X_{CL}) [ft]	**Total takeoff field length at sea level [ft] (Requirement)**	**Total takeoff field length at 5000 ft above sea level [ft]**
MWET-50	2381	825	3206 (< 4000)	3612
***MWET-50* (OEI)**[4]	3123	745	3868 (< 4000)	3990
MWET-76	3240	925	4165 (< 6000)	4711
***MWET-76* (OEI)**	4232	801	5033 (< 6000)	5711

Table 5.26: Total takeoff distances for the *MWET-50/-76* aircraft.

5.4.b Climb

In this section, the climbing performances of the *MWET* aircraft family is evaluated. Both configurations are required to reach their cruise altitude within 200 nmi travelled.

During this part of the flight, assuming that the thrust is aligned with the aircraft velocity and that no turn is initiated, the equations of motion can be written as

$$T = \tfrac{1}{2}\rho C_D V^2 S + W \sin\gamma, \tag{5.4.5}$$

$$L = W \cos\gamma, \tag{5.4.6}$$

---

[3] OEI: One Engine Inoperative above decision speed.

where γ is the angle of climb (AoC).

Solving Equations (5.4.5) and (5.4.6) then allows to obtain the vertical component of the velocity, also called Rate of Climb (RoC). It is common to represent this parameter, as well as the corresponding angle of climb (AoC) as a function of the airspeed and of the altitude. This is done in Figures 5.33 and 5.34 and with a few assumptions:

- The drag is computed using the assumption of parabolic drag;
- γ is considered small;
- The maximum available thrust is used in order to illustrate which RoC can be achieved.

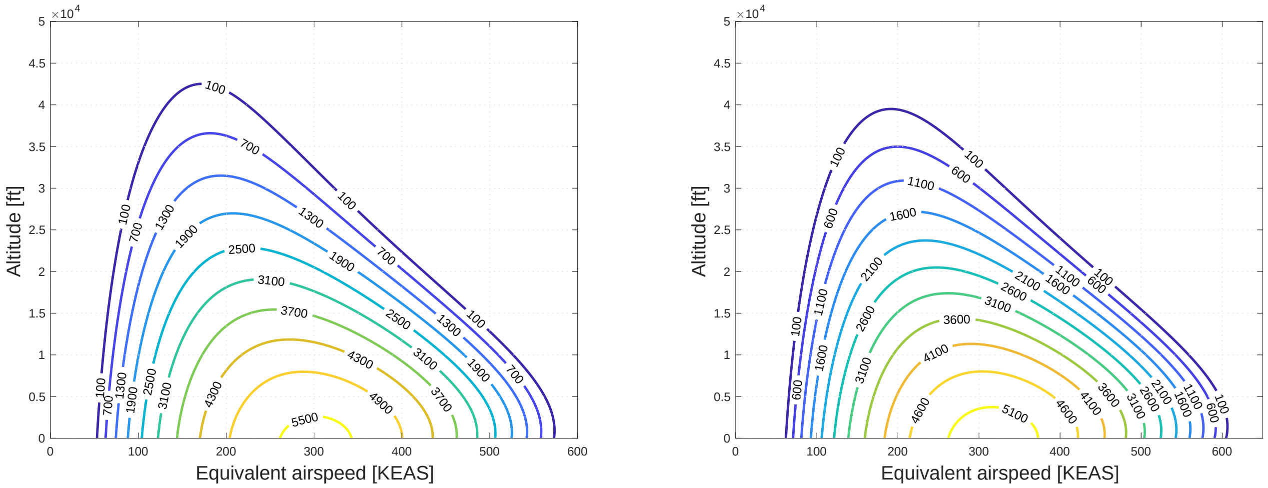

Figure 5.33: Representation of the achievable rate of climb [ft/min] for *MWET-50* (left) and *MWET-76* (right).

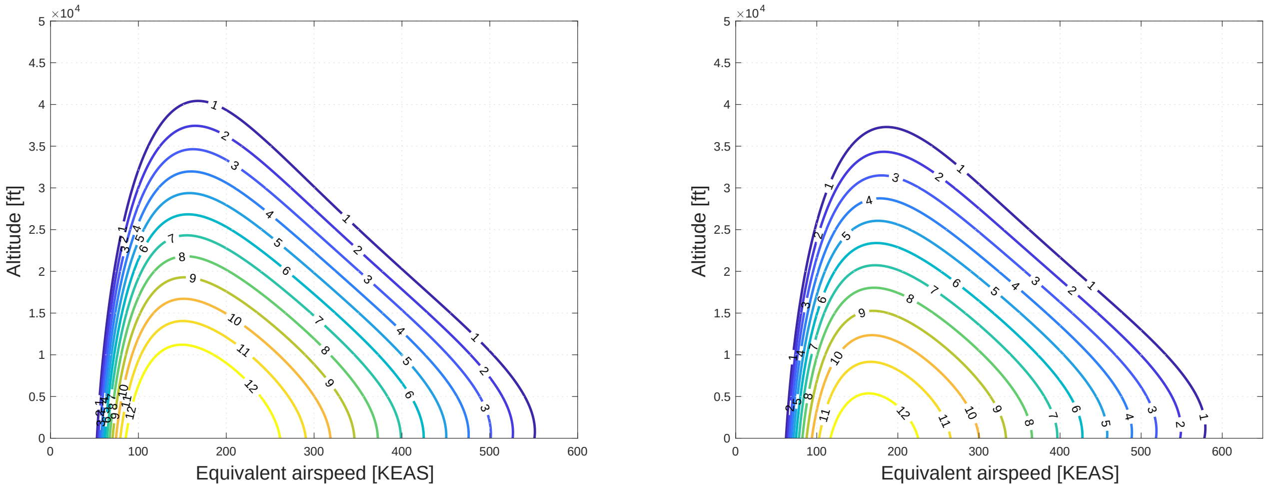

Figure 5.34: Representation of the angle of climb [deg] for *MWET-50* (left) and *MWET-76* (right).

The service ceiling altitude, the higher point for which RoC = 100 ft/min, can therefore be computed for each aircraft, as well as other useful climb quantities such a as the maximum rate of climb, $RoC_{\max}$, its associated airspeed V_Y and angle of climb AoC_Y, the maximum angle of climb, $AoC_{\max}$, and its associated airspeed V_X. They are all summarized in Table 5.27.

	MWET-50	*MWET-76*
Service Ceiling [ft]	42,500	39,500
RoC$_{\mathbf{Max}}$ [ft/min]	5624	5297.6
V$_{\mathbf{Y}}$ [kts]	301.3	317
AoC$_{\mathbf{Y}}$ [deg]	10.6	9.5
AoC$_{\mathbf{Max}}$ [deg]	14.7	12.9
V$_{\mathbf{X}}$ [kts]	141.9	159.2
RoC$_{\mathbf{X}}$ [ft/min]	3645.7	3600

Table 5.27: Relevant quantities for the climb computed at sea level.

In order to estimate the distance traveled to reach 32,000 ft, the initial cruise altitude, it is first required to compute the time necessary to climb that high. The definition of the vertical velocity gives

$$dt = \frac{dh}{RoC}. \tag{5.4.7}$$

Furthermore, it can be assumed that the rate of climb varies linearly with respect to the altitude (h) [18]. It leads to

$$\int_{t_1}^{t_2} dt = \int_{h_1}^{h_2} \frac{dh}{RoC} = \int_{h_1}^{h_2} \frac{dh}{a(h-h_i)+V_{vi}}, \tag{5.4.8}$$

and the time required to go from altitude h_i to h_{i+1} is then given by

$$\Delta t_i = t_{i+1} - t_i = \frac{1}{a} \ln \frac{(RoC)_{i+1}}{(RoC)_i} = \frac{1}{\frac{\Delta ROC_i}{\Delta h_i}} \ln \frac{(RoC)_{i+1}}{(RoC)_i}. \tag{5.4.9}$$

By decomposing the climb into short piecewise linear segments, the time to climb can be computed. In order to estimate the minimum value, it must be assumed that the aircraft is climbing at V_Y, corresponding to the maximum rate.

Finally, from the definition of the horizontal velocity

$$V_h = \frac{dx}{dt}, \tag{5.4.10}$$

a similar equation to (5.4.9) can be derived. The result is given by (5.4.11) and can be solved for Δx_i.

$$\Delta t_i = t_{i+1} - t_i = \frac{1}{\frac{\Delta ROC_i}{\Delta x_i}} \ln \frac{(V_h)_{i+1}}{(V_h)_i} \tag{5.4.11}$$

An estimation of the time necessary for a climb at V_Y at maximum thrust capability starting at 1500 ft (end of takeoff phase) and the corresponding distance traveled is presented in Table 5.28. Although it does not constitute a very precise value as the real climb strategy will be different (weather,...), it still shows that the distance traveled is a lot less than 200 nmi. A quite high margin is available.

	MWET-50	*MWET-76*
Time to climb [min]	10.5	12
Distance traveled [n mi]	56.5	68.3

Table 5.28: Time required and distance traveled during this time for a climb at V_Y from 1500 to 32,000 ft.

5.4.c Turn

This section has the purpose to study the turn of the aircraft, at a constant velocity and altitude. For this purpose, the methodology described by Raymer [18] is followed. In this maneuver, the horizontal component of the lift allows this aircraft to turn, as showed by Figure 5.35.

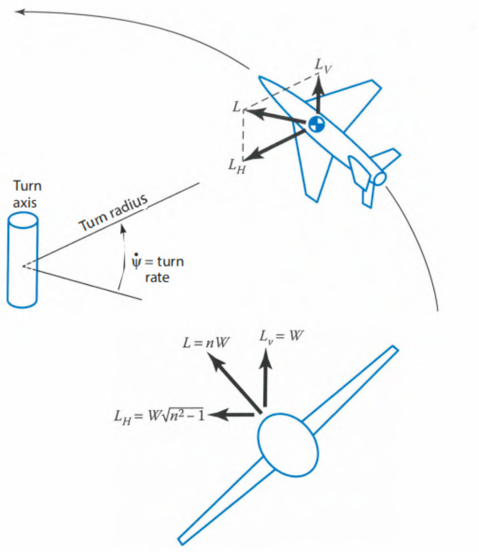

Figure 5.35: Level Turn geometry, from [18].

In this particular case, the thrust remains equal to the drag and the lift equals the weight times the load factor :

$$L = nW = \frac{W}{\sin\phi} \tag{5.4.12}$$

$$T = D \tag{5.4.13}$$

where ϕ is the bank angle, i.e. the angle between the lift and the horizontal direction. The associated turn radius R can then be computed from the horizontal component of the lift and is given by

$$R = \frac{V^2}{g\sqrt{n^2-1}}. \tag{5.4.14}$$

Figure 5.36 represents the minimum turn radius that is needed as a function of velocity. This curve was computed by solving the equations of motion at cruise altitude using the maximum thrust that the engine can produce. Alongside the minimum radius are represented curves corresponding to constant load factor and to a stall limit. It can be observed that turning at constant speed with the minimum turn radius is never sufficient to undergo a limit load factor of 2.5. At lower speed tough, stall needs to be taken into account by turning at a higher radius.

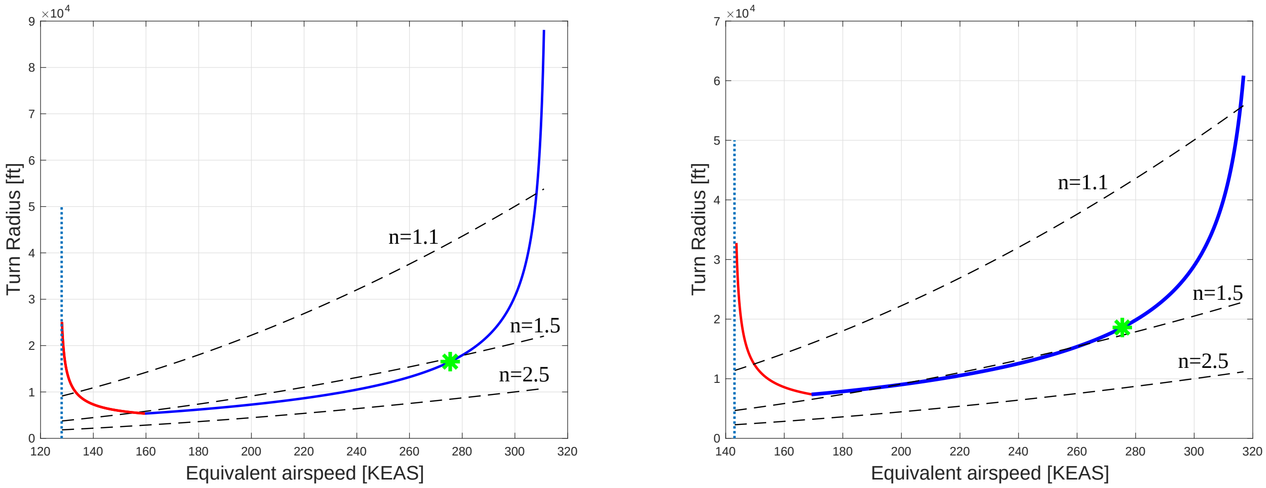

Figure 5.36: Constant velocity turn performances for *MWET-50* (left) and *MWET-76* (right), computed at 32,000 ft. The red part of the curve represents the limitation on the turn radius due to stall, the blue part is the minimum required turn radius. The green marker is placed at cruise conditions. The vertical line is the stall speed.

At cruise conditions i.e. at an equivalent velocity of 275 knots, the *MWET* aircraft family is therefore perfectly capable to turn at constant speed and with no altitude change. The maximum turning rate $\dot{\psi}_{\text{max}}$ the aircraft can achieve and the corresponding bank angle ϕ_{max}, load factor n_{max} and turn radius R_{min} are summarized at Table 5.29.

	MWET-50	*MWET-76*
$\dot{\psi}_{\text{max}}$ [deg/s]	2.6	2.3
$\mathbf{n}_{\text{max}}$ [ft]	1.5	1.42
ϕ_{max} [deg]	41.6	44.6
$\mathbf{R}_{\text{min}}$ [ft]	17,640	19,590

Table 5.29: Relevant quantities for the level turning flight computed at 32,000 ft (Mach 0.8).

5.4.d Glide

In case of all engine inoperative due to failure, glide performance of an aircraft are vital information to the pilot in order to safely attempts a landing in the closest airport. This section assesses the computation of the glide range and sink rate from cruise altitude to ground for each aircraft of the *MWET* family. Following the methodology presented in [18] and [25], first, the best glide speed can be determined as,

$$V_{\text{BG}} = \sqrt{\frac{2W}{\rho S}\sqrt{\frac{1}{C_{\text{D}_0} \cdot e\pi \text{AR}}}} = \begin{cases} 517.4 \text{ ft/s}, & \textit{MWET-50} \\ 572.2 \text{ ft/s}, & \textit{MWET-76} \end{cases} \tag{5.4.15}$$

where W, the aircraft weight, is taken at the beginning of the cruise segment and C_{D_0} is computed in case of all engine failure. Then, the pilot orients the aircraft in order to maximize its glide ratio and reach the maximal glide range. The former can be computed by,

$$\left(\frac{L}{D}\right)_{\max} = \frac{1}{\sqrt{4C_{D_0} \cdot \frac{1}{e\pi AR}}} = \begin{cases} 17.44, & \textit{MWET-50} \\ 16.97, & \textit{MWET-76} \end{cases} \tag{5.4.16}$$

so that the latter can be expressed as,

$$R_{\text{glide}} = h \cdot \left(\frac{L}{D}\right)_{\max} = \begin{cases} 92.3 \text{ nmi}, & \textit{MWET-50} \\ 89.8 \text{ nmi}, & \textit{MWET-76} \end{cases} \tag{5.4.17}$$

where h, the altitude, is 32,000 feet. The rate of descent (ROD) or sink rate of the aircraft in this situation is given by,

$$\text{ROD} = V_{\text{BG}} \cdot \sin\left(\arctan\left(\frac{h}{R_{\text{glide}}}\right)\right) = \begin{cases} 1778 \text{ fpm}, & \textit{MWET-50} \\ 2020 \text{ fpm}, & \textit{MWET-76}. \end{cases} \tag{5.4.18}$$

5.4.e Landing

The request for proposal requires a maximum landing field length of 4000 ft for the 50-passengers aircraft configuration and 6000 ft for the 76-passengers one with both an obstacle clearance of 50 ft to a runway with dry pavement (sea level ISA + 18°F day) at maximum landing weight. Moreover, both airplanes, *MWET-50* and *MWET-76*, must respect a approach velocity category C (< 141 knots). Similarly to the total takeoff field length, the total landing distance can be broken into several segments where different aerodynamic forces act.

The first segment is the approach distance, X_A (equation 5.4.19), needed to clear the imposed obstacle at the beginning of the landing phase with an approach velocity $V_A = 1.3\ V_{\text{stall}}$, which must respect the mandatory approach speed category mentioned earlier. Note that for transport aircraft, the approach angle, γ_a, should not be steeper than 3° (0.052 rad). This angle is computed following the equation 5.4.20 where D_{land} is the drag force acting during this phase and T_{idle} is the flight idle thrust. The latter, for a turbofan aircraft, is assumed at 20% of the static takeoff thrust [51]. The obtained approach angles are between 2°and 3°.

$$X_A = \frac{h_{\text{obstacle}} - h_F}{\tan\gamma_a} \tag{5.4.19}$$

$$\gamma_a = \arcsin\left(\frac{D_{\text{land}} - T_{\text{idle}}}{W_{\text{land}}}\right) \tag{5.4.20}$$

The next segment, called flare, consists of a flare with deceleration from the approach velocity to the touchdown one in order to smoothly touch the runway with the main landing gears. The flare horizontal distance X_F and flare vertical distance h_F are expressed as,

$$X_F = R\sin\gamma_a \quad \text{and} \quad h_F = R(1-\cos\gamma_a) \tag{5.4.21}$$

where R is the circular radius of the flare trajectory and function of the load factor and of the speed. When the aircraft has touched the ground, a free roll of approximately 2 seconds is assumed [18] before applying the braking systems. The resulting free roll distance X_{FR} is the one travelled during this time-lapse with the touchdown velocity.

Finally, the braking distance, X_{B}, starts when the braking devices are applied. It ends when the aircraft is completely stopped. During this segment, the thrust provided by the engines is the idle thrust and is approximated as equal to 5% of the static takeoff thrust as mentioned in [51] and [18]. The runway is assumed to be flat and dry, made of concrete and asphalt which leads to a friction coefficient $\mu = 0.4$ [-] with applied braking systems. The equation 5.4.1 can be used to determine the braking distance with V_i as the touchdown velocity and V_f equal to zero.

Considering double slotted-flaps deflected at 50° which produce a maximum lift coefficient of 2.43 [-] as mentioned in Table 4.7 and the stall velocity at landing which results from the application of these high lift devices, each segment is represented in the figure 5.37 and the total landing distances for both *MWET* configurations are synthesized in the Tab. 5.30. The AIAA requires also to show the respect of the performance requirements at landing for an altitude of 5000 ft above the sea level (ISA + 18°F). These performances are shown in the Table 5.30 where stall velocities, at seal level, of 121 knots and 137 knots are computed respectively for the *MWET-50* and the *MWET-76*. These values respect the approach velocity category C.

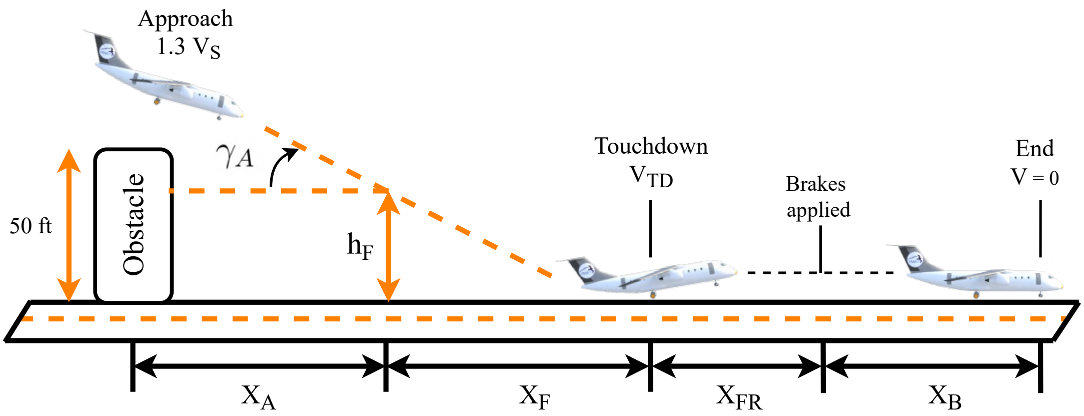

Figure 5.37: Landing phase.

	Air distance ($X_{\mathrm{A}}+X_{\mathrm{F}}$) [ft]	Ground distance ($X_{\mathrm{FR}}+X_{\mathrm{B}}$) [ft]	Total takeoff field length at sea level (Requirement) [ft]	Total takeoff field length at 5000 ft above sea level [ft]
MWET-50	1368	2319	3687 (< 4000)	4033
MWET-76	1123	2880	4003 (< 6000)	4442

Table 5.30: Landing distances for the *MWET-50/-76* aircraft.

5.4.f Range

The Request for proposal requires a short-haul range of 2000 nmi for the 50-seats configuration and at least 1500 nmi for the 76-seats aircraft. In order to be competitive with the other regional aircraft families (ERJ and CRJ series), the *MWET-50*, as well as the *-76*, are both designed to reach 2000 nmi. For the sake of safety, a mandatory requirement on the extra fuel to carry in case of close intended airport is defined by the FAR25 and must be added to the mission fuel. It requires, under commercial regulation, a additional cruise range of 100 nmi in order to reach the closest airport with a 30 min of additional loiter for daytime flights under visual flight rules (VFR), and 45 min under instrument conditions (IFR) after attempting to land at the intended destination. The worst case is set with the IFR conditions. The mission and reserve requirements are synthetized in the figure 5.38.

The knowing specific fuel consumption in cruise ($\text{SFC}_{\text{cruise}}$), described in the section 4.4.c, is used to compute the range covered by the aircraft during the cruise segment with the Breguet equation (Equation (5.4.22)) and the endurance time of this segment (Equation (5.4.23)),

$$R = \frac{V_{\text{cruise}}}{\text{SFC}_{\text{cruise}}} \frac{C_L}{C_D} \ln \left(\frac{W_{\text{start cruise}}}{W_{\text{end cruise}}} \right) \tag{5.4.22}$$

$$E = \frac{1}{\text{SFC}_{\text{cruise}}} \frac{C_L}{C_D} \ln \left(\frac{W_{\text{start cruise}}}{W_{\text{end cruise}}} \right) \tag{5.4.23}$$

where W stands the weight and V for the velocity. This equation is computed under the assumption of a cruise Mach number of 0.8 for both aircraft, at an altitude of 32,000 ft. The lift and drag coefficient are averaged over the whole cruise segment what represents approximately the values obtained for the case full-payload mid-fuel. These values are mentioned in section 5.2.a and 5.2.b respectively for the lift and drag coefficient in cruise condition.

With all these parameters, the cruise range and endurance are computed and presented in Table 5.31. Note that the descent flight segment is included in the cruise one.

	Range [nmi]	**Endurance** [min]
MWET-50	1950	251
MWET-76	1940	250

Table 5.31: Range and endurance for both *MWET* aircraft.

Knowing the needed distance to reach the cruise altitude starting from the end of the takeoff phase (detailed in Table 5.28), the total range for both aircraft is slightly higher than 2000 nmi.

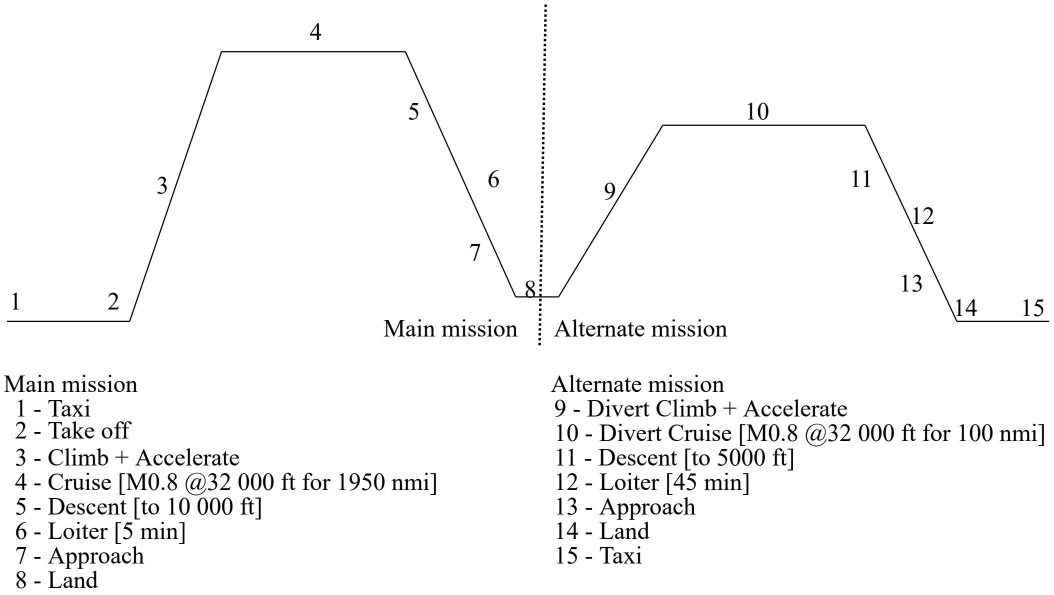

Figure 5.38: Mission requirement

In order to obtain the payload-range diagram, the fuel capacity of both aircraft must be known. The fuel volume V_{fuel} can be expressed, using empirical correlation [53], as :

$$V_{\text{fuel}} = 0.54 \cdot \frac{S_{ww}^2}{b_{ww}} \left(\frac{t}{c}\right)_{\text{root}} \cdot \frac{1+\lambda\sqrt{\tau}+\lambda^2\tau}{(1+\lambda)^2} \quad \text{with} \quad \tau = \frac{\left(\frac{t}{c}\right)_{\text{tip}}}{\left(\frac{t}{c}\right)_{\text{root}}} \tag{5.4.24}$$

where S_{ww} represents the wing surface without the winglets ($494.7 ft^2$), b_{ww} the span without the winglets ($68.9 ft$) and λ the taper ratio. The winglets are not taken into account in the fuel volume computation for the sake of structural integrity and given the defined use of this system.

As a result, the maximum amount of fuel that can be stored in the wings is 1651.7 US gallons. The needed amount of fuel (main + alternate mission) in order to cover a range of 2000 nmi with the maximum admissible number of passengers is 1793 US gallons and 2194 US gallons respectively for the *MWET-50* and *-76*. The reserve fuel represents 23% and 22% of the total amount of fuel respectively for the 50-seats and -76 configuration. However, knowing the available volume in the fuselage and the allocated volume for the storage of the landing gear as well as the luggage (section 4.5.d, the maximum fuel volume that can be stored inside the aircraft can be computed. These values are shown in the Table 5.32.

	Available volume in wings	**Available volume in fuselage**	**V_{fuel} (Designed mission)**	**Maximum V_{fuel}**
MWET-50	1651.7	912.6	1793	2564.3
MWET-76	1651.7	1473.7	2194	3125.4

Table 5.32: Fuel volume management for both *MWET* aircraft in [US Gallon].

The *MWET* aircraft family is designed to carry the maximum admissible payload over a range of at least 2000 nmi. However, the maximum fuel volume is reached if the number of passengers decreases. So the maximal range R* at the maximum takeoff weight (MTOW) is achievable by a reduction of 42% and 34% of the number of passengers respectively for the *MWET-50* and *-76*. The ferry range of the aircraft (R_{max}) is reached when all the passengers are removed and when the fuel tanks are full-filed meaning that the aircraft flies at its maximum operating weight. A general representation of the payload-range diagram is shown in the Figure 5.39 where the values obtained for each aircraft are synthetized in the Table 5.33. TOW stands for *Take-Off Weight*, ZFW means *Zero Fuel Weight* and MFW characterizes the *Maximum Fuel Weight*.

	Range [nmi]	**R*** [nmi]	**R_{max}** [nmi]	**MEW** [lb]	**MZFW** [lb]	**MTOW** [lb]
MWET-50	2000	3148 (29 pax)	3373 (0 pax)	31,370	44,190	56,200
MWET-76	2000	3265 (50 pax)	3643 (0 pax)	36,877	55,937	70,637

Table 5.33: *MWET* aircraft family range.

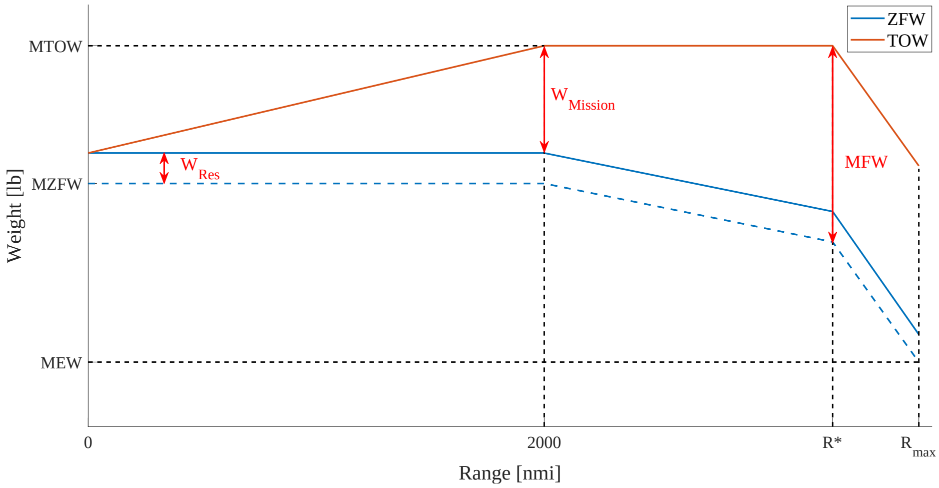

Figure 5.39: Payload-Range diagram of the *MWET* aircraft family.

5.4.g Fuel consumption

The overall goal of the *MWET-50* aircraft is to be at least 20% better than existing 50-seat regional jets in 500 nmi block fuel per seat. Regarding the existing 50-seat regional aircraft, the ERJ145 has a fuel consumption per seat per nautical mile of 0.0215 (US gallon) while the CRJ200 is a bit more consumptive with a consumption around 0.023 (US gallon) [8] [9] (these values are taken from flights of approximately 500 nmi). Using the performance of the *MWET-50* described earlier, as well as the knowledge and approximation of the specific fuel consumption for the considered engines, the amount of fuel required to perform each segment is computed. The total amount of fuel to perform a 500 nmi block is evaluated at 2815 lbs. By converting, the weight of fuel in volume using the kerosene density ($\rho = 6.7$ lb/US gal), the onboard volume of fuel is equal to 420.15 US gallons which represents a consumption of 0.0168 US gallon per seat per nautical mile. The relative difference with respect to the concurrent aircraft is included between 22% and 28.5%.

Regarding the fuel consumption for a 1000 nmi block fuel, the ERJ145 consumes 0.020 US gallon per seat per nmi, the CRJ200, 0.021 US gallon. Considering a 1000 nmi range to cover with the *MWET-50*, the consumption per seat per nautical mile is computed equal to 0.0148 US gallon, i.e. respectively 26% and 29.5% lower than the reference aircraft.

Similarly, the same analysis can be performed for the 76-seats aircraft. The ERJ170 consumes 0.021 US gallon of fuel per seat per nautical mile while the CRJ700 has a consumption of 0.022 US gallon [9] [62]. The *MWET-76*, for a 500 nmi block and 76 passengers, consumes 3650 lbs of fuel which represents a volume of 544.8 US gallons and a consumption of 0.0143 US gallon per seat per nautical mile. This results in an improvement between 32% and 35% with respect to the two previous regional aircraft with the same number of passengers and 500 nmi.

The fuel consumption for a 1000 nmi block fuel decreases to 0.018 and 0.019 US gallon per seat per nmi respectively for the ERJ170 and the CRJ700. To perform a flight over the same range, the *MWET-76* consumes 0.012 US gallon per seat per nautical mile (-33% and -37%).

The Figure 5.40 represents the repartition of the fuel consumption during the required mission (2000 nmi) of the *MWET* family aircraft.

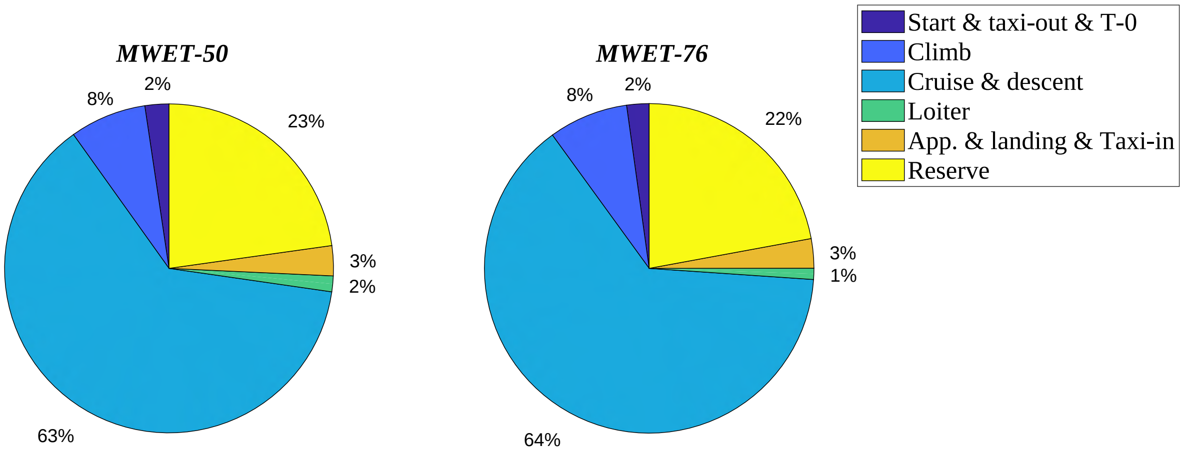

Figure 5.40: Repartition of the fuel consumption for the *MWET* family aircraft over 2000 nmi.

6 Trade-Off Study

6.1 Parameters Variation

The aim of the trade-off is to validate the design of the *MWET* aircraft family by comparing it with other design. First, the wing of *MWET* is compared to a more regular wing, meaning a wing with an usual aspect ratio. Then, the influence of a 10% variation of the *MWET* wing geometry on different metrics, such as the total weight, the fuel weight or the performance, is investigated. The weight is one of the most critical parameters for aircraft design. The total amount of fuel needed is also of primary importance, firstly because the request for proposal [1] imposes that the aircraft should be at least 20% more efficient than existing aircraft in terms of fuel consumption, and secondly because fuel is expensive and polluting. Those two parameters have the highest weight for the following trade-off studies.

6.1.a Comparison with a standard wing

Thanks to its innovative flexible winglets, the *MWET* aircraft family presents a very long and thin wing compared to existing regional aircraft. The choice to use flexible winglets for *MWET* is justified by the fact that they allow to set a high aspect ratio for the wing. To increase the aspect ratio decreases the induced drag produced by the wing and thus increases the lift-to-drag ratio. In theory, given that the induced drag force decreases, a decrease in the fuel weight needed to perform a 2000 nmi range is expected, which would help meeting the RFP requirements [1].

This section is dedicated to prove that, at the end, the use of flexible winglet is justified. To do so, a comparison with a more common wing is performed. The span of the common wing is set at the maximum value allowed at the ground by the ICAO

Code B, 24 m. The aspect ratio is set to a regular value for regional aircraft, $AR = 9$ [-]. The taper ratio, the twist and the sweep angle at quarter chord are kept the same as the ones of *MWET*. From then on, a new wing surface (S = 688.54 ft^2) and mean aerodynamic chord ($\bar{\bar{c}}$ = 9.58 ft) can be deduced.

Different metrics for the weight and the performance of the aircraft with a regular wing are shown in Table 6.1. The surface of the common wing is larger than the one of *MWET*, leading to better performance at take-off and thus a lower take-off field length. In the landing phase, the induced drag is much higher, improving the braking of the aircraft and decreasing the distance needed to land safely. However, if the performance are globally enhanced, the total amount of fuel needed to achieve the 2000 nmi range is increased by 13.9% for the 50-seats configuration and by 12.6% for the 76-seats configuration. In other words, the use of flexible winglets allows to save about 13% of fuel which is not negligible. From an economical point of view, that represent a saving of 1328.92$ per flight for the 50-seats configuration and of 1468.47$ per flight for the 76-seats configuration. To conclude, the use of flexible winglets for the *MWET* aircraft family wing design leads to economic and eco-friendly aircraft, given the reduction of pollutants coming from the reduction of the fuel burnt.

	50-seats		76-seats	
Total Weight [lbs]	57,562	+2.4%	72,235	+2.3%
Fuel for a 2000 nmi range [lbs]	13,686	+13.9%	16,552	+12.6%
Take-off field length [ft]	2903.5	-9.4%	3698	-11.2%
Take-off field length OEI [ft]	3967	+2.6%	4869	-3.2%
Landing distance [ft]	2691	-27.0%	3126	-21.9%

Table 6.1: Regular wing data and relative difference with respect to *MWET*

6.1.b 10% variation of geometrical parameters

In this subsection are compared different properties of the *MWET* aircraft family when main geometric parameters are changed. A 10% variation is considered for the wing surface and the wing aspect ratio. The impact on the total weight of the aircraft, the amount of fuel needed to satisfy the range, several performance quantities and the static stability margin is investigated. Results are presented in Tables 6.2 and 6.3 for each configurations.

Wing surface. Decreasing the wing surface allows to decrease the total weight of the aircraft and the amount of fuel needed. However, the performance for take-off and landing are negatively affected. The distance required for the take-off and the landing increases, which means that longer runways are needed. This last aspect induces more constraints on the hosting airport, reducing the number of clients that could be interested in the *MWET* family of aircraft. This increase is critical for the 50-seats configuration. The required 4000 ft of maximum field length is indeed not respected for the one engine inoperative case. In the same way, the needed landing distance is close to the maximum imposed field length (around 40 ft of the limit) for the *MWET-50*. Moreover, the approach velocity of the *MWET-76* does not respect the mandatory approach category C. In addition, the static stability margin in the worst configuration (maximum take-off weight) is out of bounds.

The opposite scenario occurs when the wing surface increases: the performance are enhanced but the total weight and the required amount of fuel increase. In addition to those bad scores for the weight and the fuel, increasing the surface while keeping the aspect ratio constant leads to a span that does not satisfy the limit imposed by the *AIAA* request for proposal [1].

Aspect ratio. Increasing the wing aspect ratio, AR, theoretically increases the lift-to-drag ratio. However, the initial AR of the *MWET* family of aircraft is already larger than usual. A 10% variation leads to an enormous and heavy wing, affecting negatively the weight of the aircraft. This increase of weight counteracts the reduction of fuel needed to perform the flight mission. The effect of a larger AR on the fuel consumption is reduced due to an heavier wing. Moreover, the maximal landing distance for the 50-seats configuration (4000 feet) is not respected when a higher aspect ratio is used, and neither is the static stability requirements.

A 10% decrease of the AR seems to be a good solution at first sight. Some performance are improved while other are less good, leading to neither a worse or better configuration. However, the lift-to drag ratio is decreased; lower AR leads to higher induced drag. More fuel is required for the flight. As the fuel is considered as a critical parameter, the solution is rejected.

Evaluation Criteria	**Wing Surface** [ft^2]			**Aspect Ratio** [-]		
Variation	**-10%**	**0**	**10%**	**-10%**	**0**	**10%**
Value	516.67	581.25	635	13.05	14.5	15.95
Total Weight [lbs]	-1.0%	56,200	+1.1%	-0.2%	56,200	+0.3%
Fuel for a 2000 nmi range [lbs]	-1.8%	12,010	+2.0%	+1.2%	12,010	-0.8%
Take-off field length [ft]	+7.1%	3206	-6.0%	-0.3%	3206	+0.1%
Take-off field length OEI [ft]	+6.7%	3868	-4.7%	+1.5%	3868	-0.5%
Approach velocity [KEAS]	+4.9%	121	-4.1%	+0%	121	+0.82%
Landing distance [ft]	+6.7%	3687	-5.9%	-8.2%	3687	+11.5%
Service ceiling [ft]	-0.5%	42,500	+0.5%	-2.8%	42,500	+2.6%
Distance traveled during climb [n mi]	+0.9%	56.5	-0.9%	+3.3%	55.6	-2.7%
Static Margin K_n [%]	17.6 - 24.1	14.8 - 20	10.6 - 15.1	11.3 - 15.8	14.8 - 20	15.7 - 21.9

Table 6.2: Variation table for *MWET-50* [5].

Evaluation Criteria	**Wing Surface** [ft^2]			**Aspect Ratio** [-]		
Variation	**-10%**	**0**	**10%**	**-10%**	**0**	**10%**
Value	516.67	581.25	635	13.05	14.5	15.95
Total Weight [lbs]	-0.9%	70,637	+0.9%	-0.1%	70,637	+0.1%
Fuel for a 2000 nmi range [lbs]	-1.6%	14,700	+1.6%	+1.6%	14,700	-1.2%
Take-off field length [ft]	+7.5%	4165	-6.5%	-0.2%	4165	+0.1%
Take-off field length OEI [ft]	+7.4%	5033	-6%	+1.3%	5033	-0.7%
Approach velocity [KEAS]	+4.4%	137	-11.7%	-1.5%	137	-0.7%
Landing distance [ft]	+7.1%	4003	-6.2%	-5.1%	4003	+6.2%
Service ceiling [ft]	-0.5%	39,500	+0.5%	-2.7%	39,500	+2.7%
Distance traveled during climb [n mi]	+2%	68.3	-1.3%	+5.4%	68.3	-3.7%
Static Margin K_n [%]	15.1 - 28.5	7.4 - 19.2	6.9 - 17.6	7.8 - 18.6	7.4 - 19.2	12.7 - 24.4

Table 6.3: Variation table for *MWET-76*.

---

[5] The green denotes the positive impact, the yellow the negative impact and the red shows when the metrics are out of the requirements.

7 Cost Analysis

This section intends to provide an estimate of the costs of the *MWET* aircraft family. For this purpose was used a modified version of the DACPA IV method, presented by Raymer [18]. The costs are predicted thanks to technical data, such as maximum velocity and empty weight, combined with cost estimating relationships (CERs). Fudge factor were also assumed using recommendations.

The production rate is assumed to be ranging from 4 to 10 aircraft per month. Over a 5 year period this gives 240 to 600 aircraft.

Note finally that the cost of living is taken into account thanks to the consumer price index (CPI) factor that can be obtained from [63]. The results of CERS, in 2012$, were therefore adapted in 2021$ by applying a 1.15 CPI factor. A steady 2.5% inflation rate was then assumed based on in order to estimate the price of the aircraft in 2030.

7.1 Non Recurring Costs

These are fixed costs that include engineering, production tooling, flight test and development support. They are summarised in Figures 7.1 and 7.2 for different production quantities.

As both aircraft share a lot of components, the engineering and tooling hours required will be lower than they would have been if the two airplanes were totally independent. For this purpose, those hours , obtained thanks to the DACPA IV model, were decreased by 20%. This value seems reasonable because overall, the number of hours required for engineering and tooling are 160% those that would have been needed for a single aircraft.

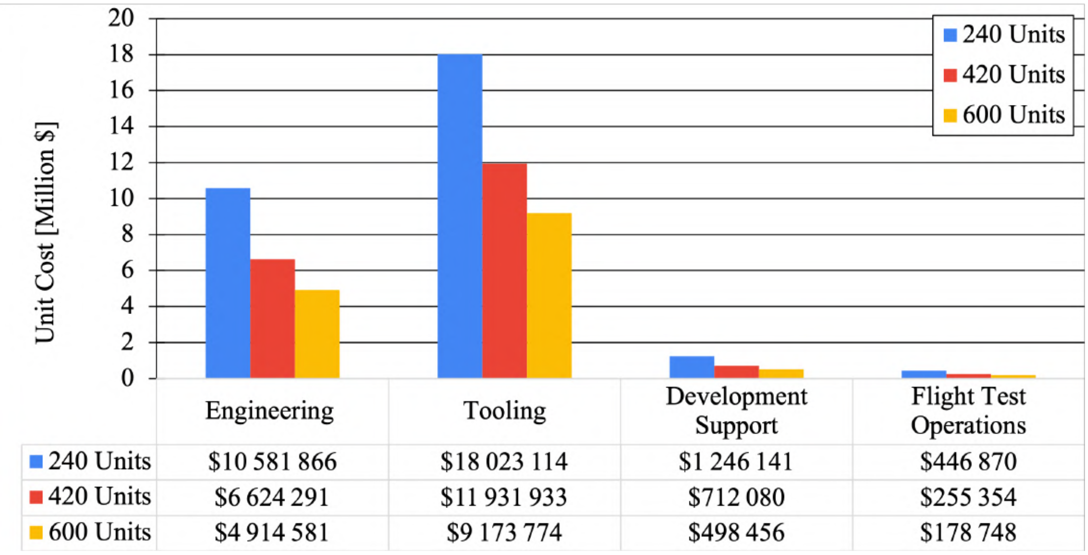

	Engineering	Tooling	Development Support	Flight Test Operations
🟦 240 Units	$10 581 866	$18 023 114	$1 246 141	$446 870
🟥 420 Units	$6 624 291	$11 931 933	$712 080	$255 354
🟨 600 Units	$4 914 581	$9 173 774	$498 456	$178 748

Figure 7.1: Non recurring unit costs for *MWET-50*, computed for different production scenarios.

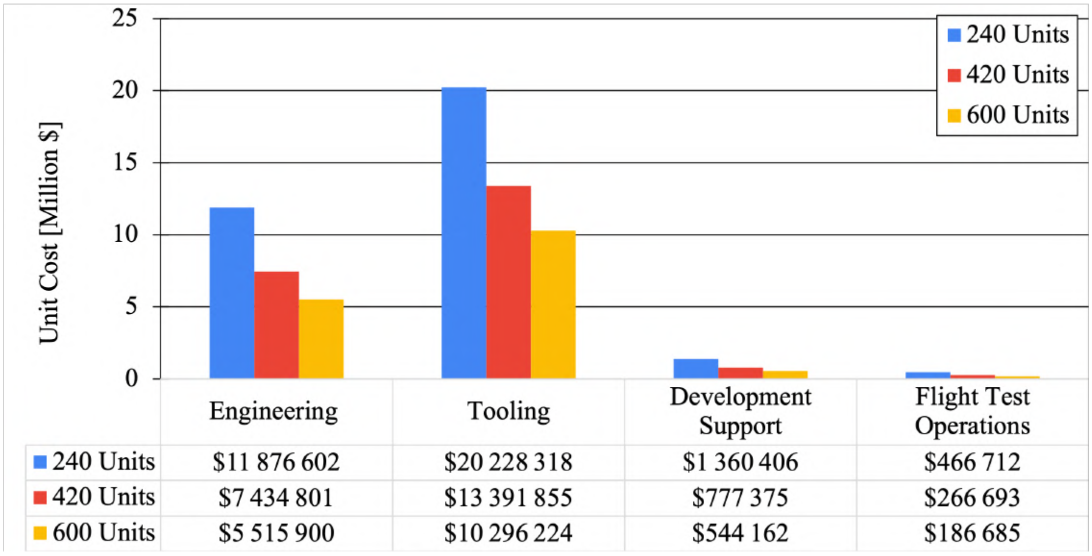

	Engineering	Tooling	Development Support	Flight Test Operations
🟦 240 Units	$11 876 602	$20 228 318	$1 360 406	$466 712
🟥 420 Units	$7 434 801	$13 391 855	$777 375	$266 693
🟨 600 Units	$5 515 900	$10 296 224	$544 162	$186 685

Figure 7.2: Non recurring unit costs for *MWET-76*, computed for different production scenarios.

7.2 Recurring Costs

The recurring costs correspond to the production of the aircraft itself. Their main contribution are due to manufacturing, material costs, quality control, avionics, engines and the interior.

The costs for different production quantities are displayed at Figures 7.3 and 7.4, while Figure 7.5 represents the Flyaway cost i.e. the cost of the next aircraft to be produced.

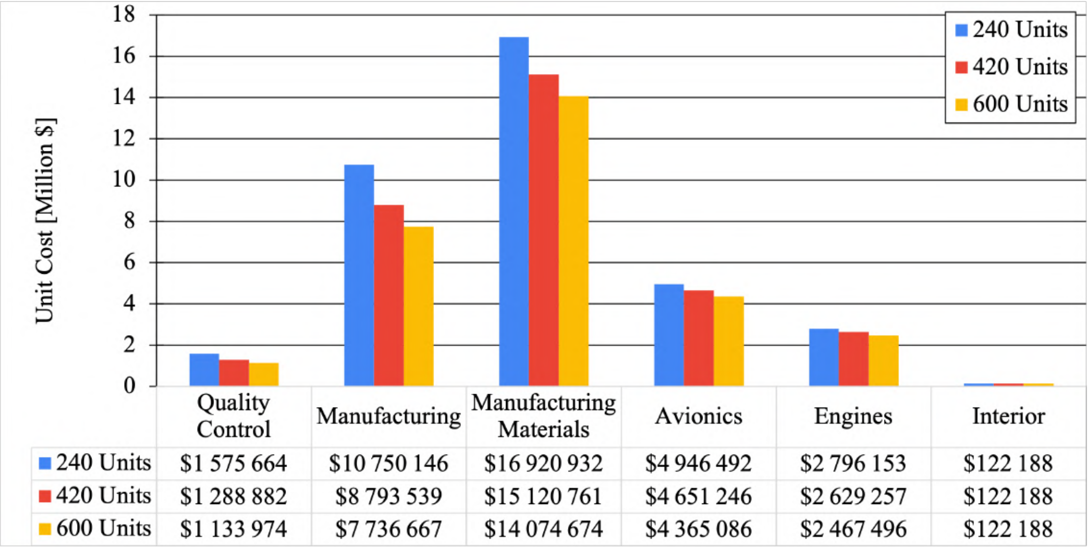

	Quality Control	Manufacturing	Manufacturing Materials	Avionics	Engines	Interior
🟦 240 Units	$1 575 664	$10 750 146	$16 920 932	$4 946 492	$2 796 153	$122 188
🟥 420 Units	$1 288 882	$8 793 539	$15 120 761	$4 651 246	$2 629 257	$122 188
🟨 600 Units	$1 133 974	$7 736 667	$14 074 674	$4 365 086	$2 467 496	$122 188

Figure 7.3: Recurring unit costs for *MWET-50*, computed for different production scenarios.

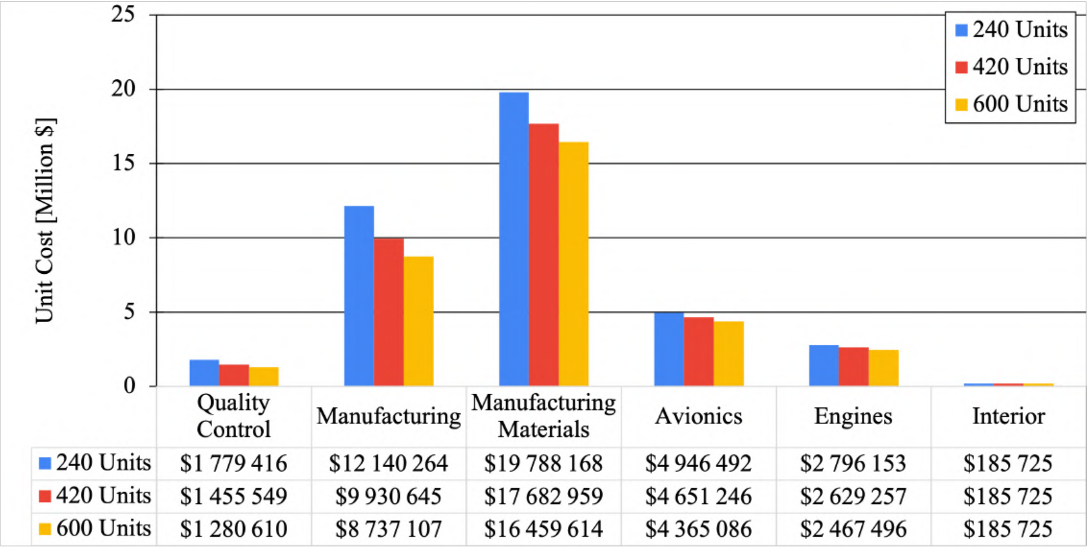

	Quality Control	Manufacturing	Manufacturing Materials	Avionics	Engines	Interior
🟦 240 Units	\$1 779 416	\$12 140 264	\$19 788 168	\$4 946 492	\$2 796 153	\$185 725
🟥 420 Units	\$1 455 549	\$9 930 645	\$17 682 959	\$4 651 246	\$2 629 257	\$185 725
🟨 600 Units	\$1 280 610	\$8 737 107	\$16 459 614	\$4 365 086	\$2 467 496	\$185 725

Figure 7.4: Recurring unit costs for *MWET-76*, computed for different production scenarios.

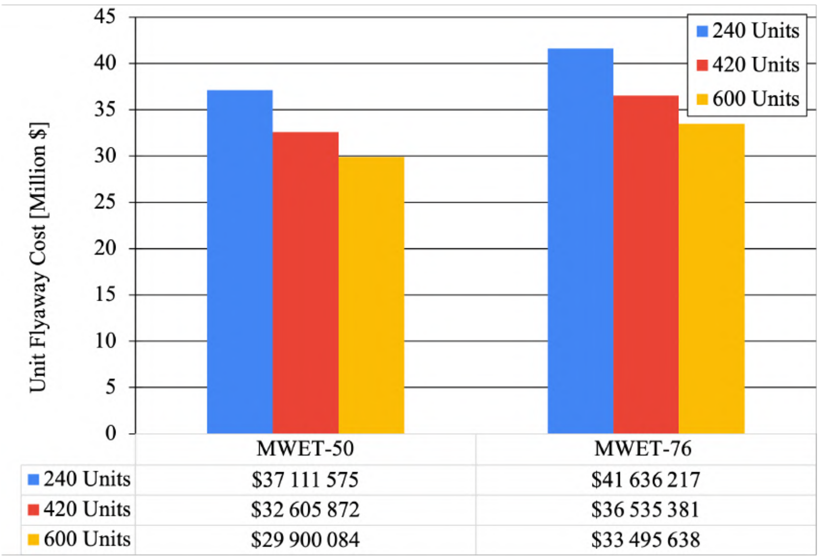

	MWET-50	MWET-76
🟦 240 Units	\$37 111 575	\$41 636 217
🟥 420 Units	\$32 605 872	\$36 535 381
🟨 600 Units	\$29 900 084	\$33 495 638

Figure 7.5: Flyaway unit costs of the *MWET* aircraft family, computed for different production scenarios.

7.3 Break-Even Analysis

Even tough aircraft are sold at a higher price than they actually cost, they do not generate profit immediately. A certain number of them needs to be sold in order to cover the fixed costs. This number, also referred as break-even point, is given by

$$N = \frac{\text{Total Fixed Costs}}{\text{Unit Sell Price} - \text{Unit Flyaway Cost}}. \tag{7.3.1}$$

The sell price is chosen as the sum of the total fixed cost and variable costs divided by the number of units to be produced, to which are added a 15% profit as well as a 10% liability insurance. As it can be observed in the previous sections, the costs are greatly influenced by the number of aircraft to be produced. In this section, a production number of 600 units within 5 years was chosen. This corresponds to a rate of 10 aircraft/month.

In the end, the *MWET* aircraft family price, in 2030, can be estimated to **$57,000,000** for the 50-passengers configuration and **$63,000,000** for its 76-passengers variation. Those results are comparable to the CRJ-200 and ERJ-145 prices, respectively equal to $64 and $63,000,000. [64]

As for the break-even point of the aircraft, it depends on the production quantity once again. For a production of 600 units, it would be reached as soon as 327 units for *MWET-50* and 336 for *MWET-76*.

7.4 Operating and Maintenance Costs

If the aircraft price is important, the costs relative to its utilization play a very important role in the decision process about whether it is worth buying or not. It is therefore crucial to estimate a them as well.

In this case, costs are mainly due to maintenance in general, to the crew salary, the consumable quantities such as oil and fuel, insurance and even depreciation. An estimation of those costs over one year, assuming 4200 hours of flight, can be found in Figure 7.6. Assuming depreciation is not part of the hourly rates of aircraft utilisation, the other costs leads to respectively **$4830 / $5250** per flight hour for *MWET-50/76*. The fuel cost includes the gain due to the electric taxiing system (310 and 381$/flight, discussed in the dedicated section) and was evaluated using a price of 5.3 $/US gallon in order to compare with existing configurations. As a title of comparison, the operating cost of the CRJ-200 and ERJ-145 are equal to 4850 and 5550 $/hour. [64]

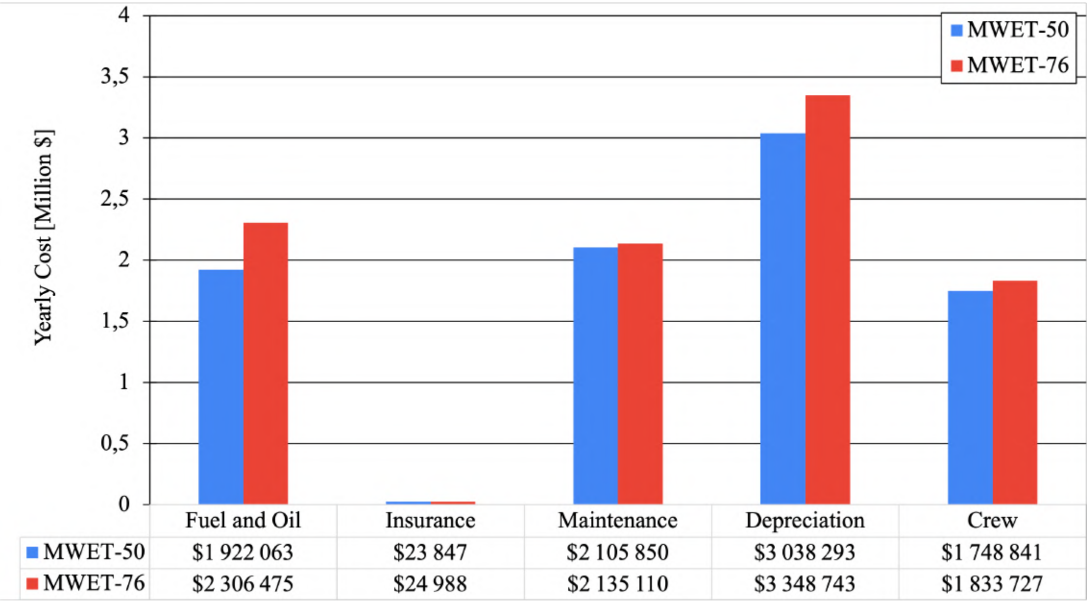

	Fuel and Oil	Insurance	Maintenance	Depreciation	Crew
🟦 MWET-50	$1 922 063	$23 847	$2 105 850	$3 038 293	$1 748 841
🟥 MWET-76	$2 306 475	$24 988	$2 135 110	$3 348 743	$1 833 727

Figure 7.6: Yearly costs of the *MWET* aircraft family

8 Conclusion

In response to the AIAA's request for proposal, the *MWET* crew presented an efficient, economic and eco-friendly regional aircraft family composed of the 50-seaters *MWET-50* and the 76-seaters *MWET-76*. It is innovative through the use of flexible winglets, which allow a longer and thinner wing than the concurrence resulting in a decrease of the induced drag produced by the aircraft. Moreover, in an era where ecology is taking a significant place, not only in aviation, but in the whole engineering industry, the use of an electric taxiing system is a real advantage for the image of the *MWET* family, in addition to saving fuel.

The design has been carried out throughout the academic year, where firstly the conceptual design was made. Starting from the requirements, as well as a complete and relevant documentation about regional aircraft, the various component of the aircraft, such as the wing, the empennage, were carefully thought and designed. The final design presented here results from a complex iterative process, which started from rough approximation and ending with a matured version of the *MWET* aircraft, that successfully fulfill the numerous requirements. The *MWET* aircraft family is more economic than the other regional aircraft as it allows to save more than 20% of fuel for several case of ranges!

The preliminary design went on with a deeper analysis of the aircraft with effective tools. The aerodynamic loads were computed and compared to validate several aspects of the design. The structure itself of the aircraft was designed and analyzed with a finite element method to provide a strong and effective family of aircraft.

The static stability, as well as the dynamic stability, was investigated and demonstrated. The performance of the aircraft was analyzed and optimized for several stages of the flight. It was proven that the *MWET* aircraft family is 20% less fuel consumptive than its competitors, which is a tremendous advantage, from an economical point of view, as well as from an ecological point of view. For the sake of comparison, a trade-off study was conducted and examined critically on several aspect of the aircraft, such as the flaps, the engines and the geometry of the wing. Finally, a complete analysis of the cost was made to prove that the *MWET* aircraft family can economically compete with existing airliners.

In conclusion, *MWET* is innovative and ecological. By meeting all the requirements of the *AIAA*, this new regional airliner family is ready to enter the next phases of the design, which consist in deeper and more precise CFD analysis.

References

[1] Request for proposal: Modern regional jet family. https://www.aiaa.org/get-involved/students-educators/Design-Competitions. Accessed April 24, 2021.

[2] Tom Cooper, Ian Reagan, Carlo Franzoni, and Chad Porter. Global fleet and mro market forecast 2021-2031. https://www.oliverwyman.com/our-expertise/insights/2021/jan/global-fleet-and-mro-market-forecast-2021-2031.html. accessed 24 April 2021.

[3] Departments, agencies of the Federal Government produced by the Office of the Federal Register (OFR), and the Government Publishing Office. Electronic code of federal regulations. https://www.ecfr.gov/cgi-bin/text-idx?node=14:1.0.1.3.11. Accessed February 8, 2021.

[4] Grigorios Dimitriadis and Ludovic Noels. Apri0004-1: Aerospace design project. http://www.ltas-cm3.ulg.ac.be/classes.htm, 2020.

[5] Mitsubishi spacejet. https://en.wikipedia.org/wiki/Mitsubishi_SpaceJet. Accessed April 24, 2021.

[6] Embraer e-jet family. https://en.wikipedia.org/wiki/Embraer_E-Jet_family. Accessed April 24, 2021.

[7] Bombardier regional jet crj-200 0. https://fr.wikipedia.org/wiki/Bombardier_CRJ200. Accessed April 24, 2021.

[8] Aircraft Commerce. *OWNER'S & OPERATOR'S GUIDE: ERJ FAMILY*. 2009.

[9] Aircraft Commerce. *OWNER'S & OPERATOR'S GUIDE: CRJ FAMILY*. 2009.

[10] A. Castrichini and T. Wilson. Preliminary investigation of use of flexible folding wing tips for static and dynamic load alleviation. *The Aeronautical Journal*, 2016.

[11] A. Castrichini and T. Wilson. Aeroelastic behaviour of hinged wing tips. *International Forum on Aeroelasticity and Structural Dynamics*, 2017.

[12] A. Castrichini and T. Wilson. Small scale flying demonstration of semi aeroelastic hinged wing tips. *International Forum on Aeroelasticity and Structural Dynamics*, 2019.

[13] Cheung, R.C.M., Rezgui, D. Cooper, J. E., and Wilson T. Testing of folding wingtip for gust load alleviation of a flexible high aspect ratio wing. *Journal of Aircraft*, 2020.

[14] A. Castrichini, Wilson T., Salteri F., Mastroddi F., Viceconti N., and Cooper J. E. Aeroelastics flight dynamics coupling effects of the semi aeroelastic hinge device. *Journal of Aircraft*, 2019.

[15] Airbus. Freely flapping wing-tips on future aircraft just took a leap forward. https://www.airbus.com/newsroom/stories/freely-flapping-wing-tips-took-a-leap-forward.html, october 2020.

[16] Airbus. Albatrossone: A revolutionary approach to aircraft wing design. https://www.airbus.com/innovation/future-concepts/biomimicry/albatrossone.html, 2019.

[17] Interplex. New electric taxiing systems save fuel while aircraft move on the ground. https://interplex.com/trends/aerospace/new-electric-taxiing-systems-save-fuel-while-aircraft-move-on-the-ground/#ftn1. accessed 12 February 2021.

[18] Daniel P. Raymer. *Aircraft Design: A Conceptual Approach*. Research Corporation, Playa del Rey, California, 2018.

[19] John Anderson. *Fundamentals of Aerodynamics*. 6th edition, 2017.

[20] Renaldo V. Jenkins, Acquilla S. Hill, and Edward J. Ray. *Aerodynamic Performance and Pressure Distribution for a NASA SC(2)-0714 Airfoil Tested in the Langley 0.3-Meter Transonic Cryogenic Tunnel*. NASA, 1988.

[21] Thomas Lambert and Grigorios Dimitriadis. Induced drag calculations with the unsteady vortex lattice method for cambered wings. *AIAA Journal*, 55(2):668–672, 2017.

[22] Thomas Lambert, Norizham Razak, and Grigorios Dimitriadis. Vortex lattice simulations of attached and separated flows around flapping wings. *Aerospace*, 4:22, 04 2017.

[23] Acxesspring. Spring catalogue. https://www.acxesspring.com/, accessed in April 2021.

[24] Mohammad H. Sadraey. *Aircraft Design: a systems engineering approach*. Daniel Webster College, New Hampshire, USA, 2010.

[25] Snorri Gudmundsson. *General Aviation Aircraft Design: Applied Methods and Procedures*. Butterworth-Heinemann, The Boulevard, Langford Lane, Kidlington, Oxford OX5 1GB, UK 225 Wyman Street, Waltham, MA 02451, USA, 2014.

[26] UIUC Applied Aerodynamics Group. Uiuc airfoil coordinates database.

[27] Dieter Scholz. Aircraft design. https://www.fzt.haw-hamburg.de/pers/Scholz/HOOU/, 2020.

[28] O. Resende. The evolution of the aerodynamic design tools and transport aircraft wings at embraer. *Journal of The Brazilian Society of Mechanical Sciences and Engineering*, 26:384, 12 2004.

[29] Paul McElroy. Boeing pilots the birth of biofuel for aviation's sustainable growth. *Our Environment*, 2019.

[30] Developing sustainable aviation fuel (saf). https://www.iata.org/en/programs/environment/sustainable-aviation-fuels/. Accessed February 05, 2021.

[31] Baxter Glenn. The use of aviation biofuels as an airport environmental sustainability measure: The case of oslo gardermoen airport. *MAD-Magazine of Aviation Development*, 8(1):6–17, 2020.

[32] Astm - standard specification for aviation turbine fuels. https://www.astm.org/Standards/D1655.htm. Accessed February 05, 2021.

[33] Astm - standard specification for aviation turbine fuel containing synthesized hydrocarbons. https://www.astm.org/Standards/D7566.htm. Accessed February 05, 2021.

[34] Astm - standard practice for evaluation of new aviation turbine fuels and fuel additives. https://www.astm.org/Standards/D4054.htm. Accessed February 06, 2021.

[35] Heyne Joshua, Rauch Bastian, Le Clercq Patrick, and Colket Meredith. Sustainable aviation fuel prescreening tools and procedures. *Fuel*, 290:120004.

[36] De Jong Sierk, Antonissen Kay, Hoefnagels Ric, Lonza Laura, Wang Michael, Faaij André, and Junginger Martin. Life-cycle analysis of greenhouse gas emissions from renewable jet fuel production. *Biotechnology for biofuels*, 10(1):1–18, 2017.

[37] Shane Kosir, Robert Stachler, Joshua Heyne, and Franchesca Hauck. High-performance jet fuel optimization and uncertainty analysis. *Fuel*, 281:118718, 2020.

[38] Feldhausen, John J, Bell, David C, Kosir, Shane T, Heyne, Joshua S, Scown, Corinne, Rapp, Vi, Comesana, and Ana. The co-optimization of sustainable aviation fuel: Cost, emissions, and performance. page 2029, 2021.

[39] Abid H. Tanzil, Kristin Brandt, Michael Wolcott, Xiao Zhang, and Manuel Garcia-Perez. Strategic assessment of sustainable aviation fuel production technologies: Yield improvement and cost reduction opportunities. *Biomass and Bioenergy*, 145:105942, 2021.

[40] MTU Aero engines. Pw800. https://www.mtu.de/engines/commercial-aircraft-engines/business-jets/pw800/?fbclid=IwAR2LPG-2i7PqScyPom0CZU-j4qSWqx8P3a6PaGpo71DIyAp_DdytYbCkiJ4, 2021.

[41] Daidzic and Nihad E. Estimation of performance airspeeds for high-bypass turbofans equipped transport-category airplanes. *Journal of Aviation Technology and Engineering*, 5:27–50, 08 2016.

[42] Matthias Bartel and Trevor Young. *Simplified Thrust and SFC Calculations of Modern Two-Shaft Turbofan Engines for Preliminary Aircraft Design*.

[43] Egbert Torenbeek. *Advanced Aircraft Design Conceptual Design, Analysis and Optimization of Subsonic Civil Airplanes*. Wiley, 2013.

[44] Mitsubishi. Mistubishi spacejet. https://www.mhi.com/group/mitac/, 2020.

[45] Cox & Company. Electro-thermal ice protection systems. https://www.coxandco.com/electro-thermal_ips.html, 25/04/21.

[46] Thales. Flight deck, avionics equipment & functions. https://www.thalesgroup.com/en/markets/aerospace/flight-deck-avionics-equipment-functions.

[47] Norman S. Currey. Aircraft landing gear design: Principles and practices. 1988.

[48] Michelin aircraft tire. *Aircraft tire Engineering Data*. Michelin.

[49] Levaux Nayan, Piret Axel, and Schmitz Vincent. Material selection for landing gears of commercial airplanes. 2017.

[50] Safran. Aircraft taxiing along with their engines shut down: Safran believes this is a winner! https://www.safran-landing-systems.com/systems-equipment/electric-taxiing-0. accessed 12 february 2021.

[51] Trevor M.Young. *Performance of the jet transport airplane*. Wiley, 2018.

[52] Ajoy Kumar Kundu. *Aircraft Design*. Cambridge university press, Queen's University Belfast, 2010.

[53] Pr.Ilan Kroo. *Aircraft Design: Synthesis and Analysis*. Desktop Aeronautics, Inc., P.O. Box 20384, Stanford, CA 94309, 2001.

[54] Grigorios Dimitriadis. Aero0016: Flight dynamics and control. http://www.ltas-aea.ulg.ac.be/cms/index.php?page=flight-dynamics-course, 2020.

[55] Adrien Crovato. *Steady Transonic Aerodynamic and Aeroelastic Modeling for Preliminary Aircraft Design*. PhD thesis, University of Liège, 2020.

[56] Gur Ohad, Mason William, and Schetz Joseph. Full-configuration drag estimation. *Journal of Aircraft - J AIRCRAFT*, 47:1356–1367, 07 2010.

[57] Federal Aviation Administration. Specific federal aviation regulation. https://www.ecfr.gov/cgi-bin/text-idx?node=14:1.0.1.3.11#se14.1.25_1333. Online; accessed 10 February 2021.

[58] Airbus. Airbus continues to shape the future. https://www.airbus.com/newsroom/news/en/2017/08/composites--airbus-continues-to-shape-the-future.html. accessed 1 August 2017.

[59] Ludovic Noels. Meca0028: Aeronautical structure course. http://www.ltas-cm3.ulg.ac.be/classes.htm, 2020.

[60] EASA. Codamein - composite damage metrics and inspection (high energy blunt impact threat. https://www.easa.europa.eu/sites/default/files/dfu/CODAMEIN_Report_20120312_highres.pdf. accessed 15 April 2021.

[61] Boeing. 787: Dreamliner. https://www.boeing.com/commercial/787/, accessed in April 2021.

[62] Aircraft Commerce. *OWNER'S & OPERATOR'S GUIDE: ERJ-135/-140/-145*. 2008/2009.

[63] Consumer price index. https://www.bls.gov/cpi/. Accessed April 05, 2021.

[64] Aircraft cost calculator. https://www.aircraftcostcalculator.com/default. Accessed April 05, 2021.